Understanding imperfections and instabilities in crystals via physics-based and data-driven models

Thesis by
Ying Shi Teh

In Partial Fulfillment of the Requirements for the
Degree of
Doctor of Philosophy in Mechanical Engineering

CALIFORNIA INSTITUTE OF TECHNOLOGY
Pasadena, California

2021
Defended April 30th, 2021

Ying Shi Teh
ORCID: 0000-0003-1743-4158

ACKNOWLEDGEMENTS

I wish to thank all the people who have made my PhD journey possible. My deepest gratitude goes to my PhD advisor, Professor Kaushik Bhattacharya. His love and curiosity in science, mathematics, and engineering have been a constant source of inspiration to me. He has also been a role model as a researcher as well as an educator. I am immensely grateful for his invaluable guidance, care, and encouragement throughout my PhD. He has not only taught me how to approach research problems, but also to persevere in the quest for knowledge and development in research.

Next I would like to thank my thesis committee: Professor Guruswami Ravichandran, Professor Michael Ortiz, and Professor Chiara Daraio, for their enlightening insights and feedback especially during the weekly joint group meetings. My sincere thanks are also extended to the graduate students and postdoctoral researchers in the joint research group, especially Roubing Bai and Swarnava Ghosh for the fruitful discussion and collaboration.

I am indebted to the Resnick Institute at Caltech and its executive director Neil Fromer for granting me the Resnick Graduate Research Fellowship to pursue my PhD work. My special appreciation also goes to Jenni Campbell for her friendly assistance and great efficiency in various administrative matters.

The friendships forged at Caltech have definitely made my PhD life all the more enjoyable and purposeful. I am especially grateful to Kavya Sudhir, Tori Lee, Erika Schibber, Linghui Wang, Valere Lambert, and Tomoyuki Oniyama for the shared meals, discussions, power-walking, running, trips, words of encouragement, and more. I want to specially thank Danilo Kusanovic for his selfless love, continual support, and encouragement, as well as all the wonderful moments we have shared during these past years at Caltech.

Last but not least, I want to thank my family for their unfailing love, care, and support even while I have been on the other side of the globe.

Ying Shi Teh
May 4, 2021

ABSTRACT

In crystals, atoms are arranged in a periodic manner in space. However in reality, imperfections and instabilities exist and this repeated arrangement is never perfect. The coupling between crystal defects, lattice instabilities, other defects like domain walls and domain patterns, and material properties generates interesting phenomena that can be leveraged on for future materials design. Nevertheless, the coupling of different scales and processes also makes the modeling and understanding of these materials an open challenge. This thesis examines these various aspects of crystalline solids through the development of both physics-based and data-driven computational models at the appropriate length scales.

Above-bandgap photovoltaic (PV) effect has been observed experimentally in multi-domain ferroelectric perovskites, but the underlying working mechanisms are not well understood. The first part of the thesis presents a device model to study the role of ferroelectric domain walls in the observed PV effect. The model accounts for the intricate interplay between ferroelectric polarization, space charges, photo-generation, and electronic transport. When applied to bismuth ferrite, results show a significant electric potential step across both 71° and 109° domain walls, which in turn contributes to the PV effect. The domain-wall-driven PV effect is further shown to be additive in nature, allowing for the possibility of generating the above-bandgap voltage.

In the second part, we present a lattice model incorporating random fields and long-range interactions where a frustrated state emerges at a specific composition, but is suppressed elsewhere. The model is motivated by perovskite solid solutions, and explains the phase diagram in such materials including the morphotropic phase boundary (MPB) that plays a critical role in applications for its enhanced dielectric, piezoelectric, and optical properties. Further, the model also suggests the possibility of entirely new phenomena by exploiting MPBs.

The final part of the thesis focuses on constructing data-driven models from first principles calculations, particularly density functional theory (DFT) for studying crystalline materials. Specifically we propose an approach that exploits machine learning to approximate electronic fields in crystalline solids subjected to deformation. When demonstrated on magnesium—a promising light weight structural material—our model predicts the energy and electronic fields to the level of chemical

accuracy, and it even captures lattice instabilities. This DFT-based machine learning approach can be very useful in methods that require repeated DFT calculations of unit cell subjected to strain, especially multi-resolution studies of crystal defects and strain engineering that is emerging as a widely used method for tuning material properties.

PUBLISHED CONTENT AND CONTRIBUTIONS

Y. S. Teh, K. Bhattacharya. Photovoltaic effect in multi-domain ferroelectric perovskite oxides. *Journal of Applied Physics*, 125(6):064103, 2019. doi: 10.1063/1.5083632. URL https://aip.scitation.org/doi/10.1063/1.5083632.

Y.S.T participated in the conception of the project, the development and numerical simulations of the model, the generation of all figures, and the writing of the manuscript.

R. Bai, **Y. S. Teh**, K. Bhattacharya. Collective behavior in the kinetics and equilibrium of solid-state photoreaction. *Extreme Mechanics Letters* 43:101160, 2021. doi: 10.1016/j.eml.2020.101160. URL https://doi.org/10.1016/j.eml.2020.101160.

Y.S.T contributed to the derivation and implementation related to the strain energy term, and participated in the editing of the manuscript.

Y. S. Teh, J. Li, K. Bhattacharya. Understanding the morphotropic phase boundary of perovskite solid solutions as a frustrated state. *Physical Review B* 103:144201, 2021. doi: 10.1103/PhysRevB.103.144201. https://link.aps.org/doi/10.1103/PhysRevB.103.144201.

Y.S.T participated in the conception of the project, the development and implementation of the model, the generation of all figures, and the writing of the manuscript.

Y. S. Teh, S. Ghosh, K. Bhattacharya. Machine-learned prediction of the electronic fields in a crystal. *In submission*. 2021.

Y.S.T participated in the conception of the project, the development and implementation of the machine learning models, the generation of all figures, and the writing of the manuscript.

TABLE OF CONTENTS

LIST OF ILLUSTRATIONS

Number *Page*

LIST OF TABLES

Chapter 1

INTRODUCTION

1.1 Imperfections and instabilities in crystals

Crystals are never perfect: imperfections and instabilities exist in crystalline solids. Their presence not only results in distortions from the ideal and periodic arrangement of atoms, but also defines various crystal properties.

Imperfections in crystals typically manifest as crystallographic defects which include vacancies, dislocations, and grain boundaries. In ferroelectric (FE) or ferromagnetic (FM) materials, there can further be two-dimensional defects called domain walls that separate different FE or FM domains. These defects or imperfections occasionally form characteristic patterns (Figure 1.1), but can also give rise to intriguing mechanical, electrical, optical, and thermal properties in crystallline solids. For example, grain orientations, sizes, and boundaries have a profound impact on ferroelectric domain switching and electromechanical response of ferroelectric materials [5–7]. Domain structures strongly influence the piezoelectric response and effective thermal conductivity of ferroelectrics, and are therefore engineered to improve these properties [8–11]. Vacancies may interact with and pin domain walls, leading to fatigue in ferroelectrics [12]. Vacancies also play a part in steady-state creep and govern various other mechanical properties of metals including ductility, yield strength, and hardness [13–15]. Similarly, dislocations govern the plastic deformations of materials [16]. In fact a recent article by Li and Lu discusses how a broad range of mechanical properties can be realized in metals through defect engineering – the careful manipulation and organization of these imperfections [17].

Certain defects like domain walls arise as a result of instabilities like phase transformations. Ferroelectricity itself is driven by a structural instability of the high-symmetry paraelectric phase that leads to the breaking of inversion symmetry and hence a spontaneous polarization [18]. The complex ferroelectric domain pattern of lead zirconate titanate in Figure 1.1(b) can also be viewed as the result of a chemically-induced instability [19]. While these instabilities are inherent characteristics of some materials, they can also be induced by other factors. For example, ferroelectric instability can be induced in strontium titanate using epitaxial strain [20] as well as in another perovskite oxide with the presence of oxygen vacancies

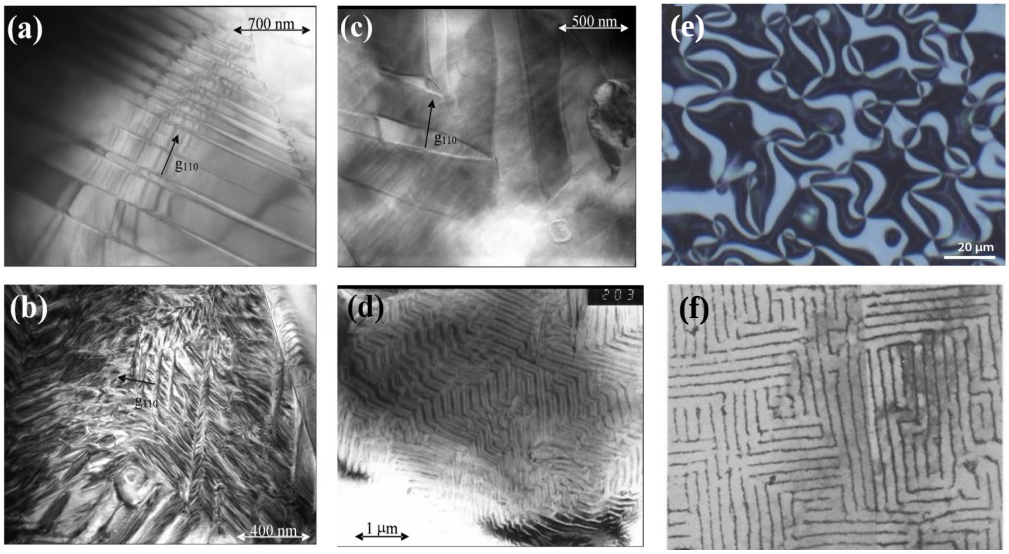

Figure 1.1: Bright field transmission electron microscopy images of domain structures of $PbZr_xTi_{1-x}O_3$ at varying compositions of (a) $x = 0.4$, (b) $x = 0.5$, (c) $x = 0.6$, and (d) $x = 0.95$. (e) Optical microscope observation of a sixfold vortex-antivortex domain structure of hexagonal rare-earth manganites. (f) Labyrinth dislocation structure of fatigued copper single crystals. All figures are adapted (with permission) from [1–3].

[19]. Metals can experience instabilities and undergo crystal structural transformation under various loading conditions or temperature change [21].

Understanding imperfections and instabilities in crystals as well as their relations with materials properties allows us to ultimately control and exploit them to develop novel materials with tantalizing properties.

1.2 Methods and challenges in modeling and simulation

For centuries, materials had been discovered and developed in a mostly serendipitous manner. With advances in high-performance computing architecture in terms of speed and storage, modeling and simulation offer a promising, systematic, and convenient pathway to understanding, predicting, and designing materials. In particular, materials modeling allows us to access the atomic or nanoscale features and isolate different mechanisms contributing to the behavior of materials, which can prove challenging through experimental means.

Quantum mechanical methods such as density functional theory (DFT) allow us to approximate solutions to the Schrödinger equation that governs the binding of atoms or ions in different material systems, and hence predict various material

properties [22]. In particular the DFT formulation that adopts plane wave basis and pseudopotentials is very efficient in unit cell or supercell calculations and has been widely used in the study of crystalline solids.

DFT calculations may not be computationally tractable in certain cases. This is especially applicable to the study of crystal imperfections or inhomogeneities which can no longer fit inside the unit cell or small supercell computational framework. Other methods suitable for the larger scale may be more appropriate. For instance, molecular dynamics (MD) and Monte Carlo (MC) methods can be very useful in simulating and understanding microstructural phenomena at the atomic scale as well as the dynamics of the systems [23]. Phase field methods offer a thermodynamically consistent platform to incorporating interfaces, kinetics, and processes such as diffusion and mass transport [24]. On the other hand, when other properties related to constructions at the much larger continuum scale (e.g. mechanical properties) are of interest, finite element methods (FEM) are typically adopted. In all these methods, generating predictions with reasonable accuracy requires good input. These inputs can come in the forms of interatomic potentials for MD, and atomistically informed or empirically obtained constitutive relations for phase field and other models at continuum level.

Some distinct phenomena of interest involve multiple processes or span across different spatial and temporal scales. Established models may be tailored to specific aspects, but neglect other important features, or they may not be computationally feasible for the larger-scale complex systems. This neccessitates the development of new models with either different theoretical bases or more efficient numerical formulation and implementation. For example, one research work that will be discussed in this thesis explores the effect of ferroelectric domain walls on the photovoltaic effect – a seemingly unrelated phenomenon. Here we have to first identify the appropriate processes or variables such as polarization, space charge, and photo-generation, and then determine how we can integrate them in a thermodynamically consistent manner instead of simply doing so with unfounded assumptions. Take the study of defects in crystals as another example. Defects couple the quantum mechanics of the defect core to the long-range elastic and electrostatic fields. It will be too costly computationally to directly employ traditional DFT methods in this problem since an enormous supercell will be needed for the slow decay of the electronic and elastic fields around the defect core. On the other hand, simple finite element methods will not be able to capture the quantum mechanical or atomistic effect. Methods such

as coarse-graining quasicontinuum (QC) and MacroDFT have been developed to bridge the different length scales [25–27]. We are motivated to investigate the possibility of incorporating machine learning methods to further enable these large-scale calculations.

1.3 Research objectives and organization of thesis

This thesis presents three distinct research studies in which computational models are developed to understand domain walls, domain patterns, lattice instabilities, crystal defects, and their effects in crystalline materials.

The first two studies focus on understanding interesting aspects of ferroelectric perovskite oxides that have not had clear concensus amongst the scientific community for years. In the first work, we are intrigued by the photovoltaic effect demonstrated in multi-domain ferroelectric perovskites [28]. However since the experimental discovery, there has been a long-standing debate on whether the effect should be attributed to the ferroelectric domain walls or the bulk photovoltaic effect inherent in noncentrosymmetric materials. We probe into the role of the domain walls in the photovoltaic effect by developing a device model at the continuum level that properly accounts for the intricate interplay between ferroelectric polarization, space charges, photo-generation, and electronic transport.

In the second work, we study perovskite solutions and the phase diagram in such materials including the morphotropic phase boundary (MPB) that plays a critical role in applications for its enhanced dielectric, piezoelectric, and ferroelectric properties. There has been great interest in understanding the underlying crystal structure at the MPB, but no clear agreement has been reached so far among the different research groups [29–33]. Another interesting and closely related aspect of the subject concerns the complex domain pattern that is observed at a narrow compositional range near the MPB (Figure 1.1(b)), but quickly disappears at other compositions (Figure 1.1(a,c)). It is worth exploring how this phenomenon can be related to the performance of the materials. To gain these understandings and in particular the competition between local chemical disorder and long-range interactions, we propose a new approach based on the random-field Ising model with long-range interactions that incorporates the basic elements of the physics at the meso-scale. The new insights gained from the model can be useful in the search for new piezoelectrics (e.g. lead-free piezoelectrics that are non-toxic as opposed to the widely available lead-based piezoelectrics) and in creating entirely new phenomena

by exploiting MPBs.

The final work concentrates on studying crystals based on density functional theory (DFT) calculations – a first principles approach – which can be a very powerful and predictive tool in materials modeling. However examining problems such as crystal defects and strain-induced instabilities directly using DFT requires very large computational domains or repeated unit cell calculations with varying strains, which can become computationally expensive. Methods such as DFT-based quasicontinuum and macroDFT have been developed to address the issue of large computational regions, but they still require repeated solutions of the unit cell subject to different distortions. Motivated by the success of machine learning in image recognition, natural language processing, and many other areas, we examine the possiblity of incorporating machine learning techniques to assist in such calculations.

Following this introduction, the remainder of the dissertation is organized as follows:

Chapter 2 provides an overview of perovskite oxides as ferroelectrics and wide-bandgap semiconductors, which serves as useful background information that will be relevant to Chapters 3 and 4.

Chapter 3 introduces the device model at the continuum scale that elucidates the role of ferroelectric domain walls in the photovoltaic effect of perovskite oxides. The model is applied to a specific perovskite oxide known as bismuth ferrite to investigate the occurence of electrostatic potential step across domain walls and the corresponding photovoltaic response in such films with different domain wall configurations including the different types (71°, 109°, and 180°) and separation widths of domain walls.

Chapter 4 discusses the development of the lattice model incorporating random fields and long-range interactions where a frustrated state emerges at a specific composition, but is suppressed elsewhere. This model is implemented and demonstrated on perovskite solid solutions such as lead zirconate titanate that have a morphotropic phase boundary along with enhanced ferroelectric and other material properties at the compostion. The same chapter illustrates how the model can be adapted to explore the possibility of creating new materials with strong ferroelectric-ferromagnetic coupling using such phase boundary.

Chapter 5 presents a machine learning model that combines model reduction with neural networks to approximate the energy and electronic fields of a crystalline unit cell subject to strain. We illustrate the model on a magnesium unit cell as an example,

and quantify the chemical accuracy of the prediction results to understand the efficacy of the model in larger DFT-based multiscale calculations. We also explore the possiblity of accurately extracting the constitutive response of the materials from the learning model.

Finally, the thesis is concluded in Chapter 6 with a summary of results and contributions, followed by some suggestions and opportunities for further enhancements.

Chapter 2

AN OVERVIEW OF FERROELECTRIC PEROVSKITES

This chapter provides a brief overview of perovskites and related properties such as ferroelectricity, as background information for Chapters 3 and 4.

2.1 Perovskites as ferroelectrics

Perovskites, or perovskite oxides, belong to the class of materials with a chemical structure of ABO_3, where A and B are typically transition metals that have a crystal structure similar to that of the mineral perovskite, $CaTiO_3$ ($Pm\bar{3}m$), Figure 2.1(a) (e.g. References [34, 35]). A number of these perovskites undergo a displacive phase transition upon cooling to transform from the high temperature perovskite structure to a low temperature structure that has lower crystallographic symmetry and no centrosymmetry, thus displaying ferroelectricity. Some examples include lead titanate ($PbTiO_3$ or PT) and bismuth ferrite ($BiFeO_3$ or BFO)[1]. Therefore these materials are widely used in capacitor, ultrasonic, optical, sensor, actuator, and storage applications.

Domains, which are regions of aligned dipoles, are commonly formed in ferroelectric materials. By symmetry, there are multiple energetically degenerate variants of the ferroelectric states. For instance, PT has six ferroelectric tetragonal states (Figure 2.1(b)) while BFO has eight ferroelectric rhombohedral states. These different states coexist in the crystal as domains. As neighboring domains are generally free to take any of the states by random, the net polarization is zero in the materials. This is indicated by point A in Figure 2.1(c). The dipoles of all the domains can be aligned through a process called *poling* in which they are exposed to a strong electric field for a period of time (point B). A remanent polarization can exist even upon the removal of the electric field (point C). The remanent polarization can be switched to the opposite direction (point E) by applying an electric field in that direction. The same figure also shows a typical hysteresis response of a ferroelectric material.

Ferroelectric perovskites also show measurable piezoelectricity. That is, when the material is subjected to a mechanical stress, electric charges build up on its surfaces. The reverse process – an internal generation of mechanical strain in response to an

[1] BFO is essentially a multiferroic material since it exhibits several ferroic orders including ferroelectricity and antiferromagnetism.

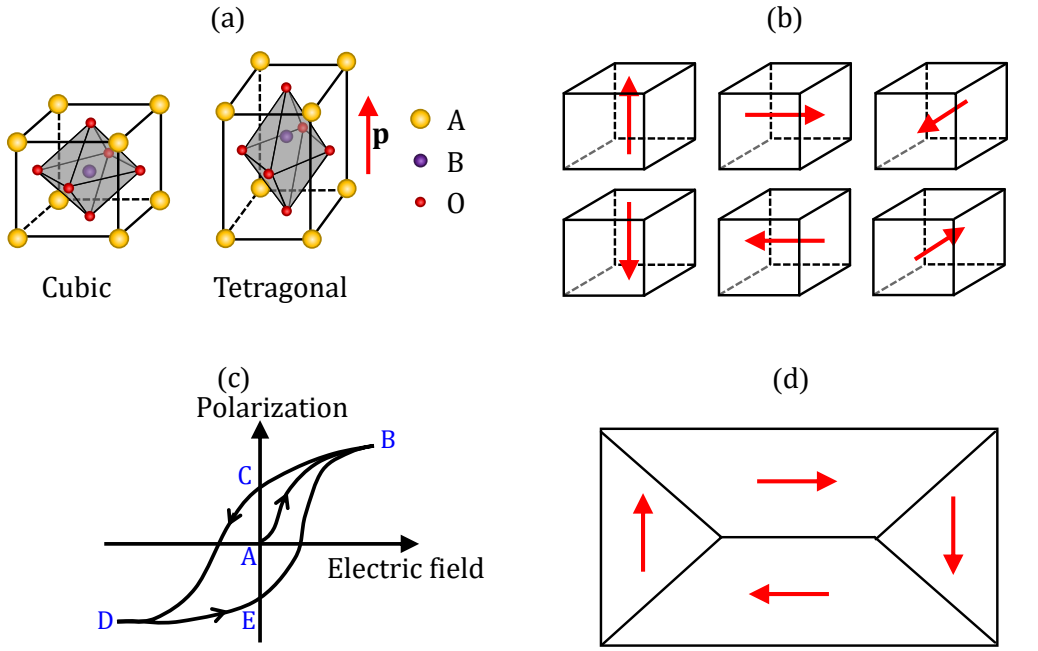

Figure 2.1: Key characteristics of ferroelectric perovskites. (a) Perovskite structure of ABO_3 in both cubic and tetragonal phases. (b) Six energetically degenerate variants of the tetragonal phase with the red arrows represent polarization directions. (c) A typical feroelectric hysteresis curve. (d) 90° and 180° domain walls present in the tetragonal phase of ferroelectrics.

applied electric field – also holds and it is known as the inverse piezoelectric effect. This piezoelectric property underlies many applications of ferroelectric perovskites including actuators, sensors, and ultrasonic transducers.

It is possible to form perovskite solid solutions where the A or B site of perovskites are substitutionally occupied by two or more species. One such example is lead zirconate titanate ($PbZr_xTi_{1-x}O_3$ or PZT). PZT has a rhombohedral phase at its PZ-rich compositions and a tetragonal phase at its PT-rich compositions. The boundary that separates the two phases occurs at a composition of around $x = 0.52$ and is called the *morphotropic phase boundary* (MPB). In fact, this composition is widely used in many applications due to its notably enhanced ferroelectric and piezoelectric properties [36]. In Chapter 4, we attempt to unravel the seeming coincidence between MPB and its enhanced properties by simulating and examining the domain patterns at various compositions. It is noteworthy that perovskite solid solutions have also been explored as a design strategy to tune other material properties such as thermochemical redox behavior [37], pigments [38], luminosity, and the corresponding wavelength [39].

Ferroelectric domains and domain walls

We have mentioned earlier that ferroelectric crystals can form domains. The boundaries that separate them are commonly known as domain walls. Ferroelectric domain walls have a typical width of a unit cell and are observed to be oriented in specific directions [40, 41]. In tetragonal phase, there can be 180° and 90° domain walls where the direction of polarization changes by the specified angle when traversing from one domain to another across the domain wall (Figure 2.1(d)). On the other hand, 71°, 109°, and 180° domain walls are found in the rhombohedral phase. These are also confirmed to be the only types of domain walls present in the respective phases by a theoretical analysis based on energy minimization [42]. To understand this in a simple manner, consider Gauss' equation in (2.1). In the bulk of the crystal, the space charge ρ is zero so $\nabla \cdot \mathbf{p} = 0$ when there is no applied electric field $\mathbf{E}$. Therefore domain walls are generally orientated in directions that satisfy this condition of divergence-free polarization. Later in Chapter 3, we will see that the polarization within a domain wall may be perturbed slightly and not necessarily satisfy the divergence-free condition.

$$\nabla \cdot (\varepsilon_0 \mathbf{E} + \mathbf{p}) = \rho \tag{2.1}$$

As 2D defects, ferroelectric domain walls present many exciting functionalities and opportunities. They are dynamic in that they are mobile and can even be controlled to move in one single direction similar to diodes [43]. They can also be pinned or stabilized, for example by space charge [44]. More recently their ability to conduct electricity has motivated hopeful prospects of transforming these walls into atomic-scale electronics [45]. The domain walls can also interact with light in intricate ways [46]. In Chapter 3 of this thesis, we investigate the role of the domain walls in the photovoltaic effect in perovskites.

A closely related property of ferroelectric materials is the polarization domain pattern, which is essentially defined by the orientations and locations of the domain walls. Domain structures can have a profound impact on the performance (for example, in terms of electromechanical coupling in microelectromechanical systems), stability, and lifetime of ferroelectrics [2]. Specifically in Chapter 4, we investigate the origin of the highly composition-dependent domain structures of perovskite solid solutions to better understand the relation between solid solution compositions and ferroelectric properties.

2.2 Perovskites as wide bandgap semiconductors

Ferroelectric perovskites are typically considered as ideal dielectrics. Compared to the commonly used semiconductors such as silicon and germanium with bandgaps of 1.14 eV and 0.67 eV, respectively [47], these perovskites have wider bandgaps. For instance, BFO has a bandgap of 2.5-2.8 eV [48, 49]. However, impurities or defects such as oxygen vacancies are inevitable in these perovskites. They can act as donors or acceptors, causing the materials to behave more like semiconductors instead. Therefore, perovskites should be more appropriately known as wide bandgap semiconductors [50]. Modeling perovskites in this notion has been done in previous works [12, 44, 51]; it is also the cornerstone of the work on understanding the photovoltaic effect in perovskites in Chapter 3.

Chapter 3

PHOTOVOLTAIC EFFECT IN MULTI-DOMAIN FERROELECTRIC PEROVSKITE OXIDES

The work presented in this chapter has been adapted from the following publication:

> Y. S. Teh, K. Bhattacharya. Photovoltaic effect in multi-domain ferroelectric perovskite oxides. *Journal of Applied Physics*, 125(6):064103, 2019. doi: 10.1063/1.5083632. URL https://aip.scitation.org/doi/10.1063/1.5083632.

3.1 Introduction

In conventional photovoltaics, electron-hole pairs are created by the absorption of photons that are then separated by an internal field in the form of heterogeneous junctions such as p-n junctions. Less than a decade ago, Yang *et al.* [28] reported large photovoltages generated in thin films of multi-domain bismuth ferrite (BFO), and suggested a new mechanism where electrostatic potential steps across the ferroelectric domain walls drive the photocurrent. This discovery has since revitalized the field of photoferroics. Among many ferroelectric oxides, BFO has particularly attracted considerable interest due to its high ferroelectric polarization and relatively small bandgap.

Many novel experiments were subsequently devised to investigate the role of domain walls in the observed photovoltaic (PV) effect in ferroelectric perovskites. Alexe and Hesse [52] performed measurements of the local photoelectric effect using atomic force microscopy (AFM). They found that the photocurrent is essentially constant across the entire scanned area, hence indicating the absence of the domain wall (DW) effect. The nanoscale mapping of generation and recombination lifetime using a method combining photoinduced transient spectroscopy (PITS) with scanning probe microscopy (SPM) points to a similar conclusion [53]. This led to the hypothesis that the bulk photovoltaic (BPV) effect, which arises from the noncentrosymmetry of perovskites, is the key mechanism instead [54, 55]. However further recent studies focused on characterizing both the BPV and DW effects show that the latter effect is much more dominant [56, 57]. The lack of clear concensus among the

scientific community on the key mechanism in the PV effect in perovskites as well as on the role of domain walls could be understood from the inherent difficulties in the experimental techniques. The nanoscale order of ferroelectric domain walls makes it difficult to probe into and separate the effects from the bulk domains and the domain walls. Other issues such as defect formation and grain boundaries in perovskite crystals further complicate the analysis.

First-principles calculations have provided a detailed understanding of the structure of domain walls [58–60], and have established the drop in electrostatic potential across it. However, they are limited to a few nanometers, and cannot examine the interaction of domain walls with other features. On the other hand, models at the device scale provide understanding at the scale [61], but assume *a priori* the polarization and other aspects of the domain wall. Finally, various phase field models provide understanding of the domain pattern [62, 63], but in the absence of space charge and photocurrent. Thus, there is a gap in our modeling of the intricate interplay between space charge, ferroelectric polarization, and electronic transport.

This work seeks to fill this gap by building on prior work of Xiao *et al.* [12, 51] and Suryanarayana and Bhattacharya [64] who developed a continuum theory of semiconducting ferroelectrics including electron and hole transport. We extend their work to include photogeneration due to illumination and study photovoltaic effect in ferroelectric perovskite oxides. We investigate the photovoltaic response of BFO films with different domain wall configurations by solving the model at the device scale. At a 71° or 109° domain wall, we observe a change in the component of polarization perpendicular to the domain wall. This in turn results in a relatively large electrostatic potential step across the wall which allows for separation of photogenerated electron-hole pairs. Thus this model supports the hypothesis of domain walls contributing to the photovoltaic effect.

We emphasize that this model does not *a priori* assume the domain wall structure or the electrostatic potential step across it. Instead, this is a prediction of the model that is based on well-established Devonshire-Landau models of ferroelectrics and lumped band models of semiconductors.

The rest of the chapter is organized as follows: In Section 3.2, we briefly review the structure of BFO and discuss the classifications of ferroelectric domain walls in BFO. We develop the theoretical framework in Section 3.3 along with an outline of the mathematical derivation in Section 3.4. We address some numerical issues faced in the implementation of the model in Section 3.5, and apply the model to

examine PV effect in ferroelectrics with domain walls in Section 3.6. Finally in Section 3.7, we conclude with a brief discussion.

3.2 Bismuth Ferrite

In this work, we focus on bismuth ferrite (BFO), though we note that the same framework can be applied to other ferroelectrics and the results are expected to be similar qualitatively.

At room temperature, BFO has a rhombohedral phase with space group $R3c$ (Figure 3.1a). The displacements of the atoms from the ideal cubic structure in this phase lead to a spontaneous polarization pointing in the $\langle 111 \rangle$ pseudocubic direction. Another distintive feature is the network of O_6 octahedra surrounding the Fe ions that rotate or tilt out-of-phase about the polarization axis. This is also commonly known as the antiferrodistortive (AFD) mode and has been found to play an important role in the ferroelectric phase of the material [60].

Electric polarization in rhombohedral BFO can take one of the eight variants of the $\langle 111 \rangle$ pseudocubic direction which gives possible domain wall orientations of 71°, 109°, and 180° (Figure 3.1(b,c)). On each domain, there can be two possible orientations of oxygen octahedra. We follow Lubk *et al.*'s method of classifying oxygen octahedra tilts (OTs) across domain walls as either *continuous* or *discontinuous* [59]. In the continuous case, the direction of oxygen octahedra tilt remains the same along the polarization vector field. In the discontinuous case, the direction reverses across the domain wall.

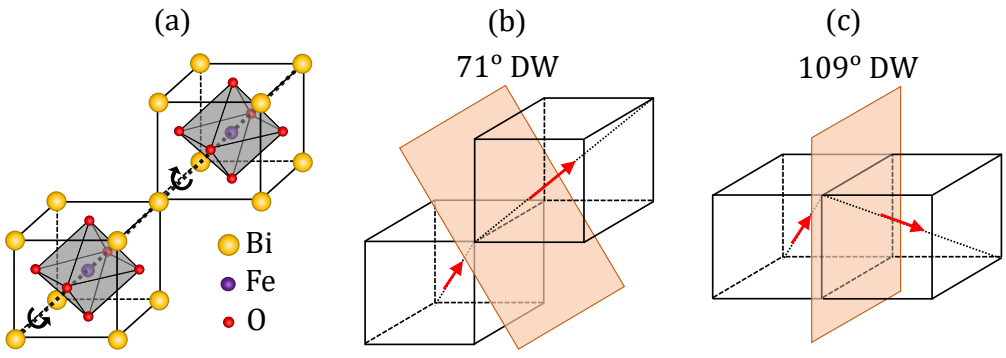

Figure 3.1: BFO crystal. (a) Crystal structure of bulk BFO. At rhombohedral phase, the two O_6 octahedra rotate out-of-phase about the polarization axis marked by the dotted line. (b) and (c) show domain walls with orientations of 71° and 109°, respectively. The red arrow in each domain points in the direction of polarization.

3.3 Theory

We consider a metal-perovskite-metal (MPM) structure that is connected to an external voltage source to form a closed electrical circuit (see Figure 3.2). The multi-domain ferroelectric perovskite film occupying the space Ω is subjected to light illumination. The two metal-perovskite interfaces are denoted by $\partial\Omega_1$, $\partial\Omega_2$ $\in \partial\Omega$. All the processes are assumed to occur at constant temperature T. We present the equations and their physical meanings here. Readers may refer to Section 3.4 for the thermodynamically consistent derivation.

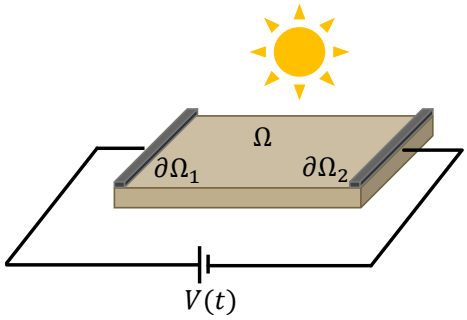

Figure 3.2: Schematic of a device model in a metal-perovskite-metal configuration.

Charge and electrostatic potential

The total charge density ($\mathbf{x} \in \Omega$) is given by

$$\rho = q(p_v - n_c + z_d N_d^+ - z_a N_a^-), \tag{3.1}$$

where q is the electronic charge, n_c is the density of electrons in the conduction band, p_v is the density of holes in the valence band, N_d^+ is the density of ionized donors, N_a^- is the density of ionized acceptors, z_d is the valency number of donors, and z_a is the valency number of acceptors. The polarization and space charge in the ferroelectrics together generate an electrostatic potential. This is determined by Gauss' equation

$$\nabla \cdot (-\epsilon_0 \nabla \phi + \mathbf{p}) = \rho, \tag{3.2}$$

where ϵ_0 is the permittivity of free space, subject to appropriate boundary conditions.

Transport equations

In the presence of light illumination, an incident photon may be absorbed in the semiconductor to promote an electron from the valence band to the conduction band,

thus generating an electron-hole pair in the process of photogeneration. The reverse may also occur such that an electron and a hole recombine. Electrons and holes may also move from one point to another point, as represented by the electron and hole density flux terms, $\mathbf{J}_n$ and $\mathbf{J}_p$. With conservation of electrons and holes, we can relate the time derivatives of densities of electrons and holes to the aforementioned processes via the following transport equations,

$$\dot{n_c} = -\nabla \cdot \mathbf{J}_n + G - R, \tag{3.3}$$

$$\dot{p_v} = -\nabla \cdot \mathbf{J}_p + G - R, \tag{3.4}$$

where G is the rate of photogeneration which can be taken to be proportional to the intensity of light illumination, while R is the recombination rate. Here we assume that the only form of recombination present is radiative recombination, which involves the transition of an electron from the conduction band to the valence band along with the emission of a photon. R takes the form of $B(n_c p_v - N_i^2)$ with the intrinsic carrier density being given by $N_i = \sqrt{N_c N_v}\exp(-\frac{E_c - E_v}{2k_B T})$ [65]. The radiative recombination coefficient B is a material property, independent of the carrier density.

The electron and hole fluxes $\mathbf{J}_n, \mathbf{J}_p$ are taken to be proportional to the gradient in its electro-chemical potential [65] via

$$\mathbf{J}_n = -\frac{1}{q}\nu_n n_c \nabla \mu_n, \tag{3.5}$$

$$\mathbf{J}_p = -\frac{1}{q}\nu_p p_v \nabla \mu_p, \tag{3.6}$$

where ν_n and ν_p are the electron and hole mobilities, respectively.

In this work, the diffusion of donors and acceptors are neglected.

Free energy

The free energy of the ferroelectric is postulated to be of the form

$$W = W_{DL}(\mathbf{p}, \theta) + W_G(\nabla \mathbf{p}, \nabla \theta) + W_{n_c}(n_c) + W_{p_v}(p_v) + W_{N_d}(N_d^+) + W_{N_a}(N_a^-). \tag{3.7}$$

The various terms are currently explained.

W_{DL} refers to the Devonshire-Landau free energy of bulk ferroelectrics. In addition to the typical primary order parameter of electric polarization $\mathbf{p}$, we include a second

order parameter—oxygen octahedral tilts θ. We adopt the following energy form for BFO [62]. The corresponding coefficients can be found in Table 3.1.

$$\begin{aligned} W_{DL} = {} & a_1(p_1^2 + p_2^2 + p_3^2) + a_{11}(p_1^4 + p_2^4 + p_3^4) + a_{12}(p_1^2p_2^2 + p_2^2p_3^2 + p_1^2p_3^2) \\ & + b_1(\theta_1^2 + \theta_2^2 + \theta_3^2) + b_{11}(\theta_1^4 + \theta_2^4 + \theta_3^4) + b_{12}(\theta_1^2\theta_2^2 + \theta_2^2\theta_3^2 + \theta_1^2\theta_3^2) \\ & + c_{11}(p_1^2\theta_1^2 + p_2^2\theta_2^2 + p_3^2\theta_3^2) \\ & + c_{12}\left[p_1^2(\theta_2^2 + \theta_3^2) + p_2^2(\theta_1^2 + \theta_3^2) + p_3^2(\theta_1^2 + \theta_2^2)\right] \\ & + c_{44}(p_1p_2\theta_1\theta_2 + p_1p_3\theta_1\theta_3 + p_2p_3\theta_2\theta_3). \end{aligned} \tag{3.8}$$

The energy stored in the ferroelectric domain walls is accounted for through the gradient or Ginzburg energy term W_G which includes the energy cost associated with rapid change in polarization and octahedral tilts.

$$W_G(\nabla\mathbf{p}, \nabla\theta) = \frac{1}{2}a_0|\nabla\mathbf{p}|^2 + \frac{1}{2}b_0|\nabla\theta|^2. \tag{3.9}$$

Here we assume that the gradient terms are isotropic for simplicity, but can easily be modified.

$W_{n_c}, W_{p_v}, W_{N_d}, W_{N_a}$ in equation (3.7) are the free energies of electrons in the conduction band, holes in the valence band, donors, and acceptors, respectively. The explicit expressions of these energies can be determined by considering each system as a canonical ensemble in the framework of statistical mechanics [64]

$$W_{n_c}(n_c) = n_cE_c + k_BT[-N_c\log N_c + n_c\log n_c + (N_c - n_c)\log(N_c - n_c)], \tag{3.10}$$

$$\begin{aligned} W_{p_v}(p_v) = {} & (N_v - p_v)E_v + k_BT[-N_v\log N_v + p_v\log p_v \\ & + (N_v - p_v)\log(N_v - p_v)], \end{aligned} \tag{3.11}$$

$$\begin{aligned} W_{N_d}(N_d^+) = {} & (N_d - N_d^+)E_d - (N_d - N_d^+)k_BT\log(2z_d) \\ & + k_BT[-N_d\log N_d + N_d^+\log N_d^+ + (N_d - N_d^+)\log(N_d - N_d^+)], \end{aligned} \tag{3.12}$$

$$\begin{aligned} W_{N_a}(N_a^-) = {} & N_a^-E_a - (N_a - N_a^-)k_BT\log(2z_a) \\ & + k_BT[-N_a\log N_a + N_a^-\log N_a^- + (N_a - N_a^-)\log(N_a - N_a^-)]. \end{aligned} \tag{3.13}$$

Polarization and tilt equations

The polarization and tilt evolve according to the (time-dependent) Landau-Ginzburg equations

$$\frac{1}{\nu_{\mathbf{p}}}\dot{\mathbf{p}} = \nabla\cdot\frac{\partial W_G}{\partial\nabla\mathbf{p}} - \frac{\partial W_{DL}}{\partial\mathbf{p}} - \nabla\phi, \tag{3.14}$$

$$\frac{1}{\nu_\theta}\dot{\theta} = \nabla \cdot \frac{\partial W_G}{\partial \nabla \theta} - \frac{W_{DL}}{\partial \theta}. \tag{3.15}$$

where $\nu_{\mathbf{p}}, \nu_\theta$ are the respective mobilities. They are subject to natural boundary conditions

$$\hat{\mathbf{n}} \cdot \frac{\partial W_G}{\partial \nabla \mathbf{p}} = 0, \tag{3.16}$$

$$\hat{\mathbf{n}} \cdot \frac{\partial W_G}{\partial \nabla \theta} = 0. \tag{3.17}$$

Electrochemical potentials

The electrochemical potentials are obtained from the energy to be

$$\mu_n = \frac{\partial W_{n_c}}{\partial n_c} - q\phi, \tag{3.18}$$

$$\mu_p = \frac{\partial W_{p_v}}{\partial p_v} + q\phi, \tag{3.19}$$

$$\mu_{N_d^+} = \frac{\partial W_{N_d}}{\partial N_d^+} + q z_d \phi, \tag{3.20}$$

$$\mu_{N_a^-} = \frac{\partial W_{N_a}}{\partial N_a^-} - q z_a \phi. \tag{3.21}$$

At thermal equilibrium, $\mu_n = -\mu_p = -\mu_{N_d^+} = \mu_{N_a^-} = E_{f_m}$ where the magnitude of E_{f_m} is the workfunction of the metal electrode. Further, using equations (3.10) to (3.13), we can invert the relations to obtain

$$n_c = \frac{N_c}{1 + \exp(\frac{E_c - E_{fm} - q\phi}{k_B T})}, \tag{3.22}$$

$$p_v = \frac{N_v}{1 + \exp(\frac{E_{Fm} - E_v + q\phi}{k_B T})}, \tag{3.23}$$

$$N_d^+ = N_d \left[1 - \frac{1}{1 + \frac{1}{2z_d}\exp(\frac{-E_{fm} + E_d - q\phi z_d}{k_B T})}\right], \tag{3.24}$$

$$N_a^- = N_a \left[1 + 2z_a \exp(\frac{-E_{f_m} + E_a - q\phi z_a}{k_B T})\right]^{-1}, \tag{3.25}$$

consistent with Fermi-Dirac distribution [66]. Finally, assuming $N_c >> n_c$ and $N_v >> p_v$, equations (3.5) and (3.6) become

$$\mathbf{J}_n = -\frac{\nu_n k_B T}{q}\nabla n_c + \nu_n n_c \nabla\phi, \tag{3.26}$$

$$\mathbf{J}_p = -\frac{\nu_p k_B T}{q}\nabla p_v - \nu_p p_v \nabla\phi. \tag{3.27}$$

Equations (3.26) and (3.27) show that each of $\mathbf{J}_n$ and $\mathbf{J}_p$ can be resolved into two contributions: (1) a diffusion current, driven by the concentration gradient of carriers, and (2) a drift current, driven by an electric field. By applying the Einstein relation which relates diffusion constant D to mobility ν via $D = \nu k_B T/q$, we recover the equations that are typically written to describe the flow of electrons and holes in solar cells.

Ohmic boundary conditions

We prescribe ohmic boundary conditions at the contacts with metal electrodes following [67] for convenience. We have

$$\left.\begin{aligned} n_c &= N_c e^{-(E_c - E_{fm})/k_B T} \\ p_v &= N_v e^{-(E_{fm} - E_v)/k_B T} \end{aligned}\right\} \quad \text{on } \partial\Omega_1 \cup \partial\Omega_2. \tag{3.28}$$

This is equivalent to assuming that the Fermi level in the semiconductor aligns with that of the metal, hence giving rise to electron and hole densities that are independent of the applied voltage.

Steady-state model

At steady state, all the fields of interest do not vary with respect to time. Further, we are interested in domain walls, and therefore can assume that things are invariant parallel to the domain wall. This means that we have one independent space variable which we denote r. We denote the components of polarization and tilt parallel (respectively perpendicular) to the domain wall to be p_s, θ_s (respectively p_r, θ_r). With $z_d = z_a = 1$, we have a coupled system of differential equations for region $x \in (0, L)$, where L is the length of the film.

$$a_0 \frac{d^2 p_r}{dr^2} - \frac{\partial W_{DL}}{\partial p_r} - \frac{d\phi}{dr} = 0, \tag{3.29}$$

$$a_0 \frac{d^2 p_s}{dr^2} - \frac{\partial W_{DL}}{\partial p_s} = 0, \tag{3.30}$$

$$b_0 \frac{d^2\theta_r}{dr^2} - \frac{\partial W_{DL}}{\partial \theta_r} = 0, \tag{3.31}$$

$$b_0 \frac{d^2\theta_s}{dr^2} - \frac{\partial W_{DL}}{\partial \theta_s} = 0, \tag{3.32}$$

$$-\epsilon_0 \frac{d^2\phi}{dr^2} + \frac{dp_r}{dr} = q(p_v - n_c + N_d^+ - N_a^-), \tag{3.33}$$

$$-\frac{dJ_n}{dr} + G - B(n_c p_v - N_i^2) = 0, \tag{3.34}$$

$$-\frac{dJ_p}{dr} + G - B(n_c p_v - N_i^2) = 0, \tag{3.35}$$

$$J_n = -\frac{\nu_n k_B T}{q} \frac{dn_c}{dr} + \nu_n n_c \frac{d\phi}{dr}, \tag{3.36}$$

$$J_p = -\frac{\nu_p k_B T}{q} \frac{dp_v}{dr} - \nu_p p_v \frac{d\phi}{dr}, \tag{3.37}$$

where

$$N_d^+ = N_d \left[1 - \frac{1}{1 + \frac{1}{2}\exp(\frac{-E_{fm} + E_d - q\phi}{k_B T})} \right],$$

$$N_a^- = N_a \left[1 + 2\exp(\frac{-E_{f_m} + E_a - q\phi}{k_B T}) \right]^{-1},$$

$$N_i = \sqrt{N_c N_v} \exp(-\frac{E_c - E_v}{2k_B T}),$$

with boundary conditions

$$\frac{dp_r}{dr}(r = 0) = \frac{dp_r}{dr}(r = L) = 0,$$

$$\frac{dp_s}{dr}(r = 0) = \frac{dp_s}{dr}(r = L) = 0,$$

$$\frac{d\theta_r}{dr}(r = 0) = \frac{d\theta_r}{dr}(r = L) = 0,$$

$$\frac{d\theta_s}{dr}(r = 0) = \frac{d\theta_s}{dr}(r = L) = 0,$$

$$\phi(r = 0) = V, \quad \phi(r = L) = 0,$$

$$n_c(r = 0) = n_c(r = L) = N_c e^{-(E_c - E_{fm})/k_B T},$$

$$p_v(r = 0) = p_v(r = L) = N_v e^{-(E_{fm} - E_v)/k_B T}.$$

3.4 Derivation of a thermodynamically consistent theory

We outline a derivation of the model in Section 3.3, and show that it is thermodynamically consistent. Since we consider only isothermal processes, the second law of thermodynamics (Clausius-Duhem inequality) requires the rate of dissipation to be non-negative. This rate of dissipation is given by

$$\mathcal{D} = \mathcal{F} - \frac{d\mathcal{E}}{dt}, \tag{3.38}$$

where $\mathcal{F}$ is the rate of external work done on the system

$$\begin{aligned}\mathcal{F} = &\int_\Omega \mu_n G_{\mathtt{net}} dV + \int_\Omega \mu_p G_{\mathtt{net}} dV + \frac{d}{dt}\int_{\partial\Omega_1\cup\partial\Omega_2} \phi\sigma \, dS - \int_{\partial\Omega} \mu_n \mathbf{J}_n \cdot \hat{\mathbf{n}} \, dS \\ &- \int_{\partial\Omega} \mu_p \mathbf{J}_p \cdot \hat{\mathbf{n}} \, dS - \int_{\partial\Omega} \mu_{N_d^+} \mathbf{J}_{N_d^+} \cdot \hat{\mathbf{n}} \, dS - \int_{\partial\Omega} \mu_{N_a^-} \mathbf{J}_{N_a^-} \cdot \hat{\mathbf{n}} \, dS, \end{aligned} \tag{3.39}$$

and $\mathcal{E}$ is the energy stored in the system

$$\mathcal{E} = \int_\Omega \left(W + \frac{\epsilon_0}{2} |\nabla\phi|^2 \right) dV. \tag{3.40}$$

The first two terms in equation (3.39) denote the rate of work done by incident photons in generating electron-hole pairs. Here $G_{\mathtt{net}} = G - R$ denotes the net rate of photogeneration. The third term refers to the work done by the external voltage and $\sigma = [\![-\epsilon_0 \nabla\phi + \chi \mathbf{p}]\!] \cdot \hat{\mathbf{n}}$ is the surface charge density where $[\![\cdot]\!]$ indicates a jump in the respective quantity $(\cdot)$ and $\hat{\mathbf{n}}$ is a unit vector normal to the surface. The final four terms are the energy carried into the systems by the fluxes of electrons, holes, donors, and acceptors at the boundary. The total energy consists of the free energy and the electrostatic energy stored in the electrostatic field.

Applying the divergence theorem and transport equations (3.3), (3.4), we rewrite equation (3.39) as

$$\begin{aligned}\mathcal{F} = &\frac{d}{dt}\int_{\partial\Omega_1\cup\partial\Omega_2} \phi\sigma dS - \int_\Omega \nabla\mu_n \cdot \mathbf{J}_n \, dV - \int_\Omega \nabla\mu_p \cdot \mathbf{J}_p \, dV \\ &- \int_\Omega \nabla\mu_{N_d^+} \cdot \mathbf{J}_{N_d^+} \, dV - \int_\Omega \nabla\mu_{N_a^-} \cdot \mathbf{J}_{N_a^-} \, dV + \int_\Omega \mu_n \dot{n}_c \, dV + \int_\Omega \mu_p \dot{p}_v \, dV \\ &+ \int_\Omega \mu_{N_d^+} \dot{N}_d^+ \, dV + \int_\Omega \mu_{N_a^-} \dot{N}_a^- \, dV. \end{aligned} \tag{3.41}$$

From equations (3.40) and (3.7), the rate of change of the total energy of the system

can be expressed as

$$\begin{aligned}\frac{d\mathcal{E}}{dt} = &\int_\Omega \left(-\nabla\cdot\frac{\partial W_G}{\partial \nabla \mathbf{p}} + \frac{\partial W_{DL}}{\partial \mathbf{p}}\right)\cdot\dot{\mathbf{p}}\, dV \\ &+ \int_\Omega \left(-\nabla\cdot\frac{\partial W_G}{\partial \nabla \theta} + \frac{W_{DL}}{\partial \theta}\right)\cdot\dot{\theta}\, dV + \frac{d}{dt}\left(\frac{\epsilon_0}{2}\int_{\mathbb{R}_3}|\nabla\phi|^2 dV\right) \\ &+ \int_\Omega \left(\frac{\partial W_{p_v}}{\partial p_v}\dot{p_v} + \frac{\partial W_{n_c}}{\partial n_c}\dot{n_c} + \frac{\partial W_{N_d}}{\partial N_d^+}\dot{N}_d^+ + \frac{\partial W_{N_a}}{\partial N_a^-}\dot{N}_a^-\right) dV \\ &+ \int_{\partial\Omega}\left(\hat{\mathbf{n}}\cdot\frac{\partial W_G}{\partial\nabla\mathbf{p}}\right)\cdot\delta\mathbf{p}\, dS + \int_{\partial\Omega}\left(\hat{\mathbf{n}}\cdot\frac{\partial W_G}{\partial\nabla\theta}\right)\cdot\delta\theta\, dS. \end{aligned} \tag{3.42}$$

Following [64], we can show (see Appendix A.1 for details)

$$\begin{aligned}\frac{d}{dt}\left(\frac{\epsilon_0}{2}\int_\Omega|\nabla\phi|^2 dV\right) = &\int_{\partial\Omega_1\cup\partial\Omega_2}\phi\,\dot{\sigma}\, dS + \int_\Omega \nabla\phi\cdot\dot{\mathbf{p}}\, dV \\ &+ \int_\Omega \phi\, q\,(z_d\dot{N}_d^+ - z_a\dot{N}_a^- - \dot{n_c} + \dot{p_v})dV. \end{aligned} \tag{3.43}$$

Therefore,

$$\begin{aligned}\mathcal{D} = &\int_\Omega\Bigg[\left(\nabla\cdot\frac{\partial W_G}{\partial\nabla\mathbf{p}} - \frac{\partial W_{DL}}{\partial\mathbf{p}} - \nabla\phi\right)\cdot\dot{\mathbf{p}} + \left(\nabla\cdot\frac{\partial W_G}{\partial\nabla\theta} - \frac{W_{DL}}{\partial\theta}\right)\cdot\dot{\theta} \\ &+ \left(\mu_n - \frac{\partial W_{n_c}}{\partial n_c} + q\phi\right)\dot{n_c} + \left(\mu_p - \frac{\partial W_{p_v}}{\partial p_v} - q\phi\right)\dot{p_v} \\ &+ \left(\mu_{N_d^+} - \frac{\partial W_{N_d}}{\partial N_d^+} - qz_d\phi\right)\dot{N}_d^+ + \left(\mu_{N_a^-} - \frac{\partial W_{N_a}}{\partial N_a^-} + qz_a\phi\right)\dot{N}_a^- \\ &- \nabla\mu_n\cdot\mathbf{J}_n - \nabla\mu_p\cdot\mathbf{J}_p - \nabla\mu_{N_d^+}\cdot\mathbf{J}_{N_d^+} - \nabla\mu_{N_a^-}\cdot\mathbf{J}_{N_a^-}\Bigg] dV \\ &+ \int_{\partial\Omega}\left[\left(\hat{\mathbf{n}}\cdot\frac{\partial W_G}{\partial\nabla\mathbf{p}}\right)\cdot\dot{\mathbf{p}} + \left(\hat{\mathbf{n}}\cdot\frac{\partial W_G}{\partial\nabla\theta}\right)\cdot\dot{\theta}\right] dS. \end{aligned} \tag{3.44}$$

Each of the above terms is a non-negative product of a generalized force and a generalized velocity or rate. Assuming either over-damped dynamics or equilibrium gives rise to the equations in Section 3.3.

3.5 Numerical issues

The model derived above comprises of differential equations that are nonlinear and coupled, which can prove troublesome numerically. See equations (3.29-3.37). So we non-dimensionalize the problem as in Appendix A.2. Further, we notice that the coupling between the first five governing equations and the rest of the model is weak. This is especially so when the length of the simulated device is much

smaller than the Debye length, or when the dimensionless quantity δ is small, which is generally the case in the simulations in this work. Therefore we treat them as two subproblems, that are then solved self-consistently until convergence occurs. Each subproblem is constructed within the finite difference framework, and the resulting system of nonlinear equations is solved using the trust-region dogleg method.

3.6 Application to Bismuth Ferrite

Material constants

The coefficients of the Devonshire-Landau energy for BFO in equation (3.8) are presented in Table 3.1. They are derived to match the values of spontaneous polarization, tilt angles, and dielectric constant [60, 68, 69]. Other material parameters including band structure information [49] and carrier mobility values [70] are listed in Table 3.2. The values of a_0 and b_0 are chosen to match a ferroelectric domain wall width of 2 nm. Typically BFO exists as an n-type semiconductor due to oxygen vacancies. It can also become p-type with Bi deficiency. Here we restrict our simulations to n-type semiconductors.

Symbols	Values	Units
a_1	-1.19×10^9	$\mathrm{V\,m\,C^{-1}}$
a_{11}	9.93×10^8	$\mathrm{V\,m^5\,C^{-3}}$
a_{12}	3.93×10^8	$\mathrm{V\,m^5\,C^{-3}}$
b_1	-1.79×10^{10}	$\mathrm{V\,m^{-3}\,C}$
b_{11}	1.14×10^{11}	$\mathrm{V\,m^{-3}\,C}$
b_{12}	2.25×10^{11}	$\mathrm{V\,m^{-3}\,C}$
c_{11}	1.50×10^{10}	$\mathrm{V\,m\,C^{-1}}$
c_{12}	7.50×10^9	$\mathrm{V\,m\,C^{-1}}$
c_{44}	$-1.60 \times 10^{1-}$	$\mathrm{V\,m\,C^{-1}}$

Table 3.1: Coefficients of Laudau-Devonshire energy for BFO

Two-domain ferroelectrics

(i) 71° and 109° domain walls

We consider a device comprising of a BFO film with two ferroelectric domains separated by either a 71° or 109° domain wall, with continuous or discontinuous oxygen octahedra rotations across the domain wall. This gives a total of four different cases, as illustrated in Table 3.3.

Figures 3.3 and 3.4 show the variation of various field quantities when the perovskite

Parameters	Symbols	Values	Units
Electron mobility	μ_n	2×10^{-5}	$m^2\,V^{-1}\,s^{-1}$
Hole mobility	μ_p	1×10^{-5}	$m^2\,V^{-1}\,s^{-1}$
Energy of conduction band	E_c	-3.3	eV
Energy of valence band	E_v	-6.1	eV
Donor level	E_d	-3.7	eV
Acceptor level	E_a	-5.8	eV
Effective density of states for conduction band	N_c	1×10^{24}	m^{-3}
Effective density of states for valence band	N_v	1×10^{24}	m^{-3}
Donor concentration	N_d	1×10^{20}	m^{-3}
Acceptor concentration	N_a	0	m^{-3}
Polarization gradient coefficient	a_0	9×10^{-10}	$V\,m^3\,C^{-1}$
AFD gradient coefficient	b_0	2×10^{-9}	$V\,m^{-1}\,C$
Rate of photogeneration	G	1×10^{27}	$m^{-3}\,s^{-1}$
Radiative recombination coefficient	B	1×10^{-9}	$m^3\,s^{-1}$
Thickness of film	L	100	nm
Temperature	T	300	K
Work function of Pt	$-E_{f_m}$	5.3	eV

Table 3.2: Material and simulation parameters

71°domain wall Polarization: $\langle 111\rangle \longrightarrow \langle 11\bar{1}\rangle$		**109°domain wall** Polarization: $\langle 111\rangle \longrightarrow \langle 1\bar{1}\bar{1}\rangle$	
(a)	**(b)**	**(c)**	**(d)**
Continuous OT	Discontinuous OT	Continuous OT	Discontinuous OT
$[111] \longrightarrow [11\bar{1}]$	$[111] \longrightarrow [\bar{1}\bar{1}1]$	$[111] \longrightarrow [1\bar{1}\bar{1}]$	$[111] \longrightarrow [\bar{1}11]$
$E_{DW} = 0.53\ J\,m^{-2}$	$E_{DW} = 0.63\ J\,m^{-2}$	$E_{DW} = 0.53\ J\,m^{-2}$	$E_{DW} = 0.45\ J\,m^{-2}$
$J_{sc} = -0.22\ A\,m^{-2}$	$J_{sc} = -0.84\ A\,m^{-2}$	$J_{sc} = 0.98\ A\,m^{-2}$	$J_{sc} = -1.0\ A\,m^{-2}$
$V_{oc} = 6.8$ mV	$V_{oc} = 29$ mV	$V_{oc} = -70$ mV	$V_{oc} = 38$ mV

Table 3.3: Device models with different types of domain walls. Note that $\langle\cdot\rangle \longrightarrow \langle\cdot\rangle$ and $[\cdot] \longrightarrow [\cdot]$ denote the directions of electric polarization and oxygen octahedra tilt (OT), respectively, on two neighboring domains. J_{sc} and V_{oc} are the short-circuit current density and open-circuit voltage obtained from our device model simulations. E_{DW} refers to the domain wall energy calculated at thermal equilibrium in the absence of light illumination.

film is exposed to light illumination and shorted. Notice that in all cases, the perpendicular component of the polarization p_r is not constant in the vicinity of the domain wall. In other words, the polarization is not divergence free, and we see a

voltage drop across the domain wall. The polarization profile (i.e. p_r) of 71° and 109° domain walls with continuous OT are qualitatively similar to those obtained from first-principles calculations [59]. This voltage drop across the domain wall leads to charge separation of photogenerated electron-hole pairs, and a non-zero photocurrent. This is evident in the current-voltage plots shown in Figure 3.5 and is consistent with the mechanism proposed by Yang *et al.* [28].

Figure 3.5 shows that the magnitude and direction of photocurrent due to the domain wall effect hinge greatly upon the changes in the crystallographic structure across the domain wall. The case with 109° DW and continuous OT gives a positive short-circuit current, which is in the same direction as net polarization in the film while the rest show negative currents. Importantly, this DW-based photovoltaic effect shows that the direction of current flow does not necessarily correlates with the direction of net polarization consistent with experimental observations [56].

Furthermore, we observe strong coupling between polarization and oxygen octahedra tilt (OT). This is evident from the vastly different results (including the change in current direction) obtained when changing the OT profiles without changing the type of domain walls. In actual experiments, we may only observe one type of oxygen octahedra rotation for each domain wall type. We compute the domain wall energy for each case as in Table 3.3, and find that it is energetically more favorable to have 71° domain wall with continuous OT and 109° domain wall with discontinous OT. This is consistent with previous first-principles calculations [60, 62].

As the perovskite film is first exposed to light illumination, which is simulated in terms of an increase in the photogeneration rate of electron-hole pairs, the magnitude of the short-circuit current density generated increases rapidly initially as shown in Figure 3.6. The increase slows down at higher illumination (or photogeneration rate) due to recombination of the excited electrons and holes.

Finally we consider changing the order of the domains in a two-domain device. Figure 3.7 shows that doing so does not pose any difference to the profiles of other quantities such as p_r and ϕ. This implies that current flows in a single direction irrespective of the order of the domains. If we were to stack the different domains to form a device with periodic domain pattern (i.e. alternating domains), the photovoltaic effect would be additive and would not cancel out. This is exactly what we observe later in the section.

(ii) 180° domain walls

In the case of the 180° domain walls, with either continuous or discontinuous OTs, there is no visible disturbance to the polarization component normal to the domain wall at the domain wall. With a lack of symmetry breaking, the photovoltaic effect fails to be generated. The figures are omitted for brevity.

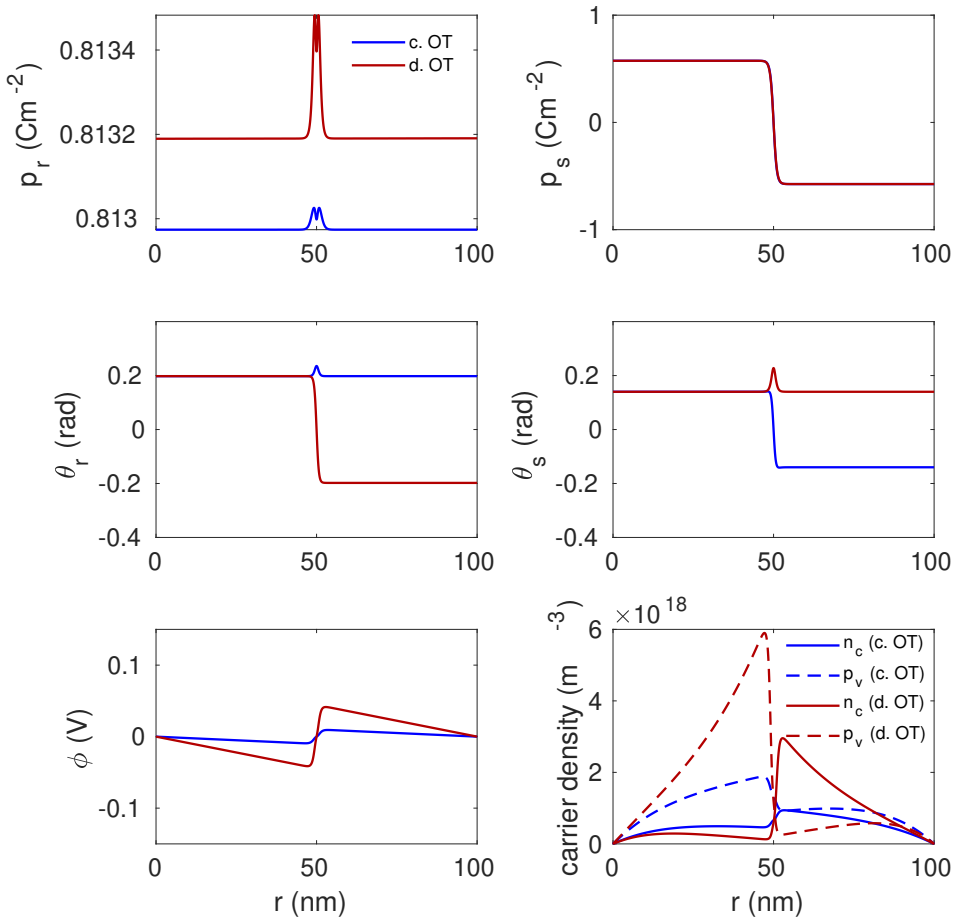

Figure 3.3: Spatial variation of field quantities (polarization components, OT tilt angles, electric potential, and carrier densities) along the 71° DW device with either continuous or discontinuous OT at short circuit under light illumination.

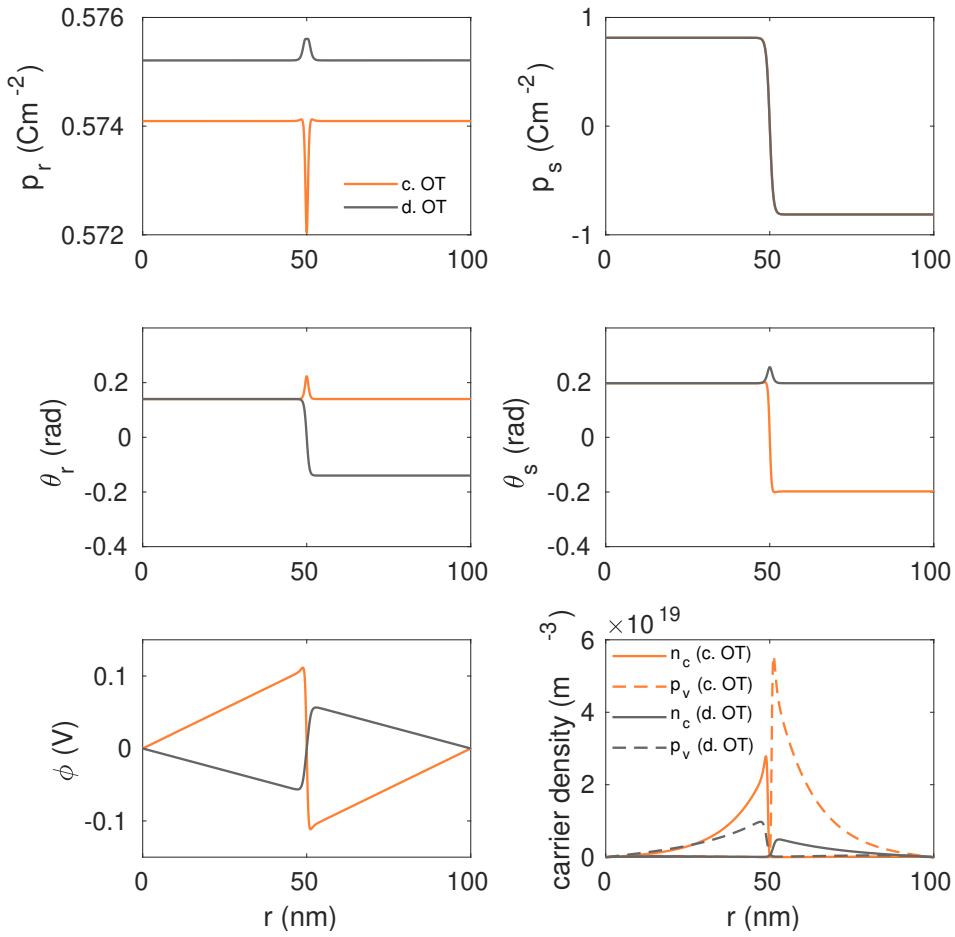

Figure 3.4: Spatial variation of field quantities (polarization components, OT tilt angles, electric potential, and carrier densities) along the 109° DW device with either continuous or discontinuous OT at short circuit under light illumination.

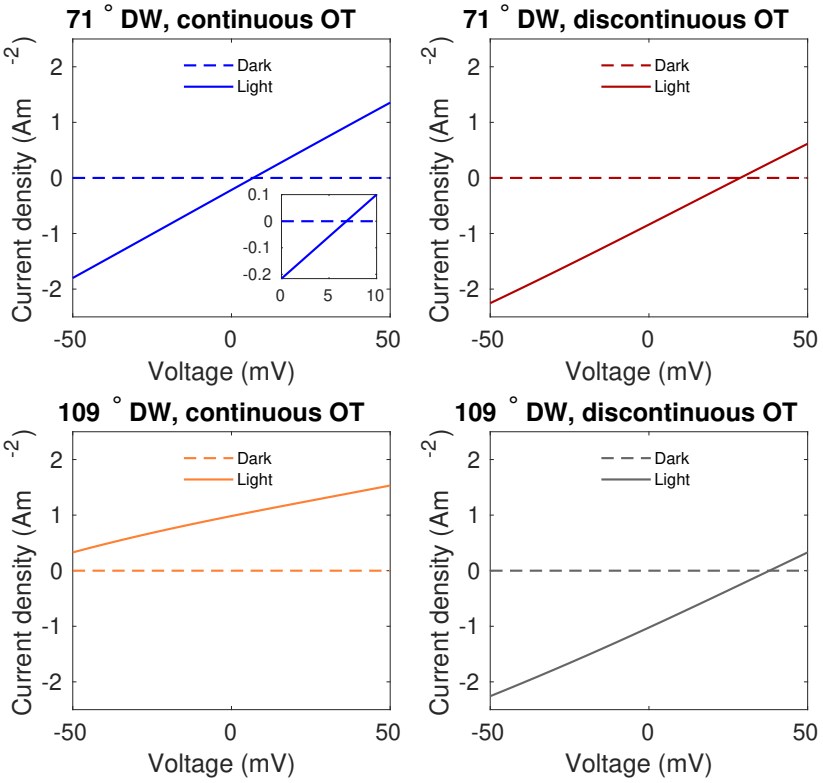

Figure 3.5: Current-voltage plot in dark ($G = 0$) and under light illumination ($G = 10^{27}\,\mathrm{m}^{-3}\,\mathrm{s}^{-1}$) for BFO devices with a 71° or 109° DW with continuous or discontinuous OT.

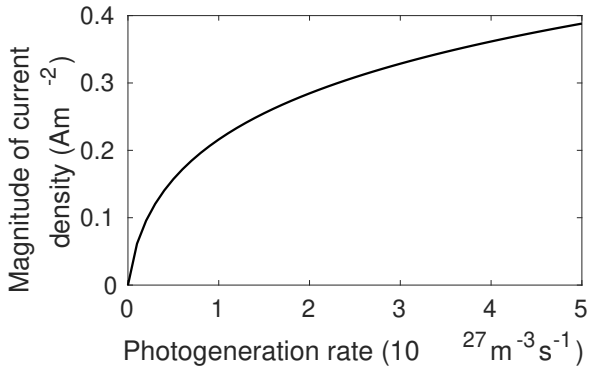

Figure 3.6: Short-circuit current density versus photogeneration rate for a two-domain ferroelectrics separated by a 71° DW with continuous OT.

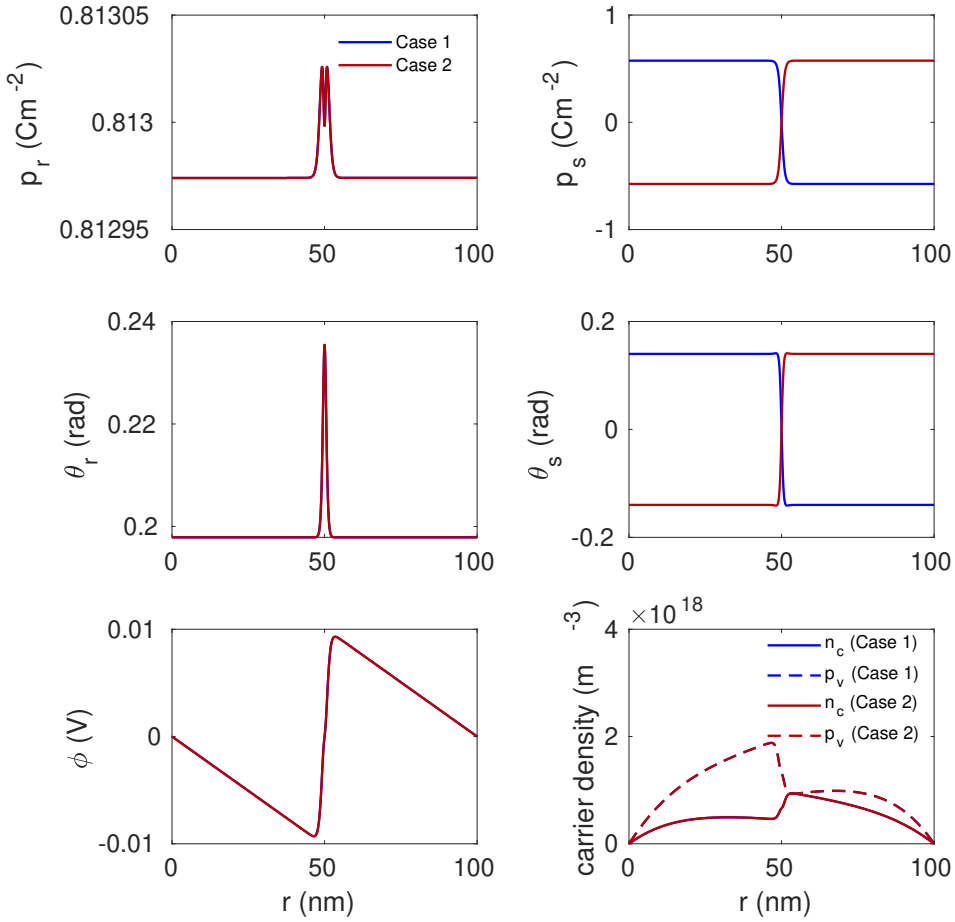

Figure 3.7: Spatial variation of field quantities along a two-domain device (71° DW, continuous OT) at short circuit. The two cases are identical, except the order of the two domains is reversed.

Ferroelectrics with multiple domain walls

We now examine the case with multiple domain walls. We keep the width of the perovskite film constant and uniformly place a number of domain walls parallel to the metal electrodes within the film. The distribution of polarization, oxygen octahedra tilts (OTs), and other field quantities for a shorted device with ten 71° domain walls are presented in Figure 3.8. Polarization and OTs are periodic and electric potential varies in a zig-zag manner but with a slope.

Figure 3.9 shows that the magnitudes of both short-circuit current and open-circuit voltage increase with the density of domain walls in the device. The additive effect becomes smaller at higher domain wall number as it is influenced by the boundary.

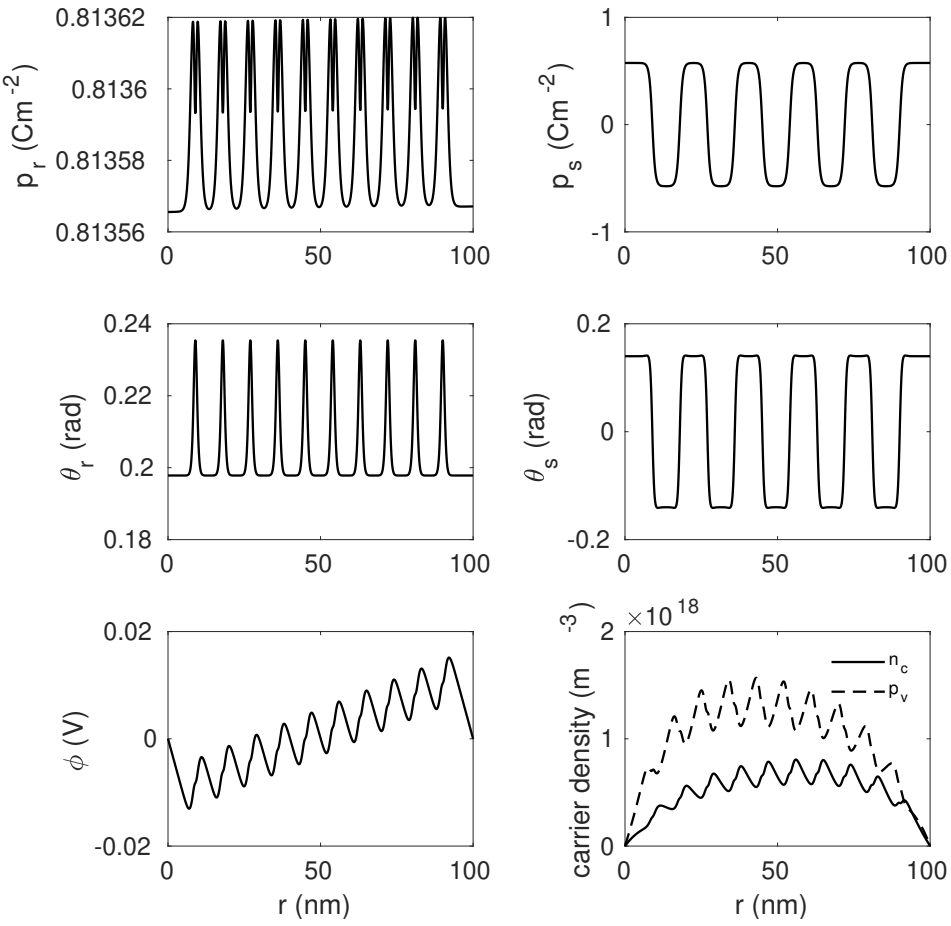

Figure 3.8: Spatial variation of field quantities for ferroelectrics with ten 71° DWs and continuous OTs at short circuit.

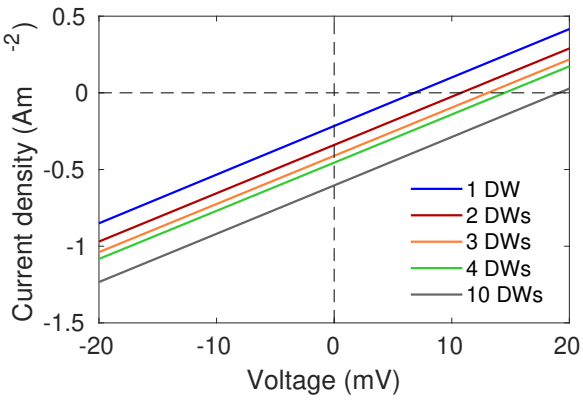

Figure 3.9: Current-voltage plot for multi-domain BFO devices with 71° DWs and continuous OTs.

Effect of varying doping and width of ferroelectric film

Next, we investigate the effect of doping and width on the ferroelectric response using a two-domain example. All the previous simulations are run using a small donor doping density of $N_d = 10^{20}\,\mathrm{m}^{-3}$ and a width of 100 nm, which corresponds to the state of complete depletion. Typically a depletion layer forms at a metal-semiconductor interface and the width of the depletion layer is related to the Debye length which is dependent on the dopant density and dielectric constant. Complete depletion occurs when the Debye length of the material is much larger than the width of the device. Otherwise there is partial or local depletion. Figure 3.10 shows the short-circuit distributions for two different perovskite widths of 100 nm and 500 nm at a low dopant density level of $N_d = 10^{20}\,\mathrm{m}^{-3}$ and a high dopant density of $N_d = 10^{22}\,\mathrm{m}^{-3}$. At a small width of 100 nm, changing the doping level from low to high does minimal changes to the field profiles and the photovoltaic response, with its short-circuit current density staying almost constant at -0.22 $\mathrm{A\,m}^{-2}$. On the other hand, at a larger width of 500 nm, increasing the doping level changes the state of the perovskite film from complete depletion to partial depletion, and at the same time, raises the short-circuit current density from -0.011 $\mathrm{A\,m}^{-2}$ to -0.033 $\mathrm{A\,m}^{-2}$. The resulting electric potential profile can be viewed as the superposition of two contributions: domain walls and depletion. This illustrates the feature of the model in combining the ferroelectric and semiconductor behavior of the material.

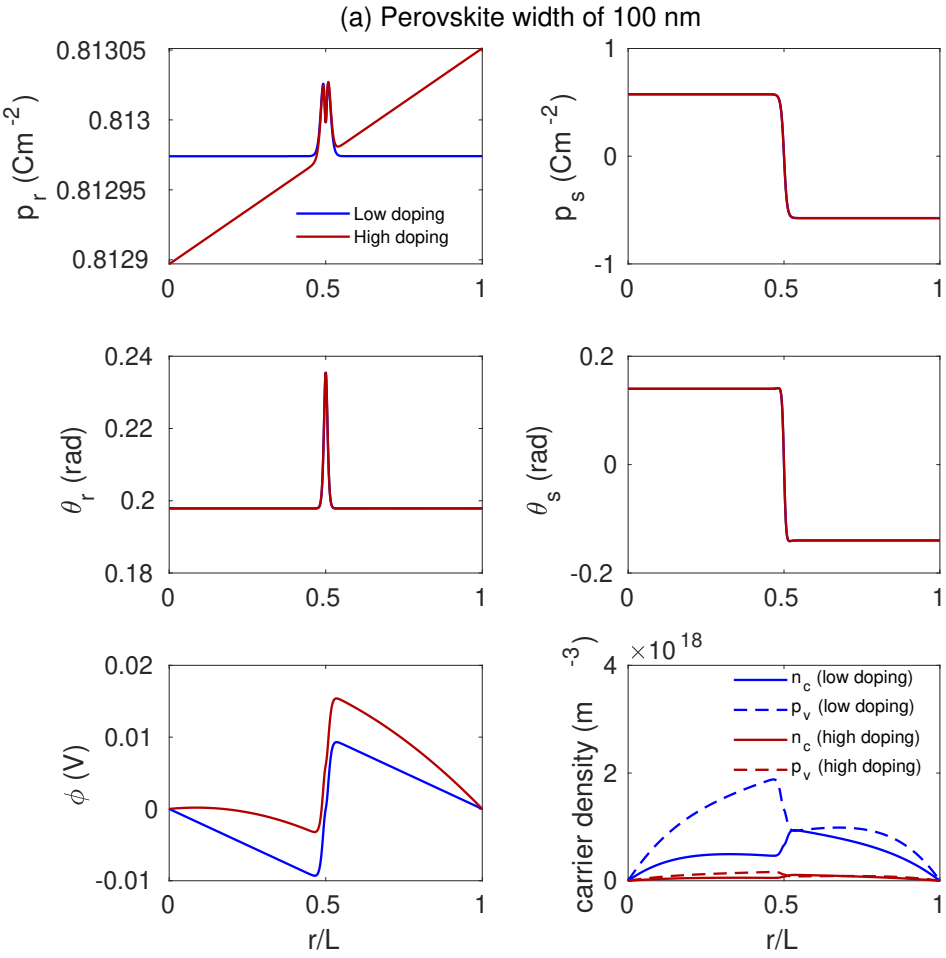

Figure 3.10: *(To be continued on the next page.)*

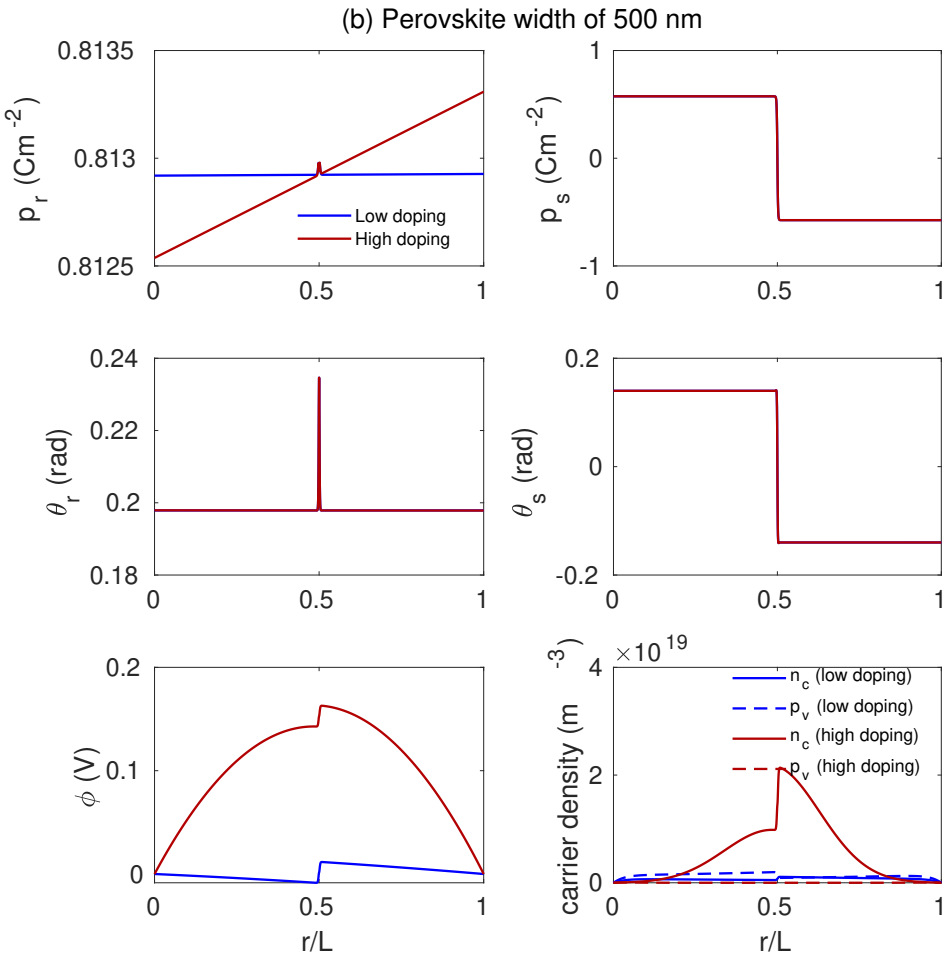

Figure 3.10: Spatial variation of field quantities along two-domain devices (71° DW, continuous OT) of (a) width 100 nm and (b) width 500 nm, with low dopant level of $N_d = 10^{20}\,\mathrm{m}^{-3}$ and high dopant level of $N_d = 10^{22}\,\mathrm{m}^{-3}$, at short circuit.

3.7 Conclusions and discussion

We have proposed a thermodynamically consistent continuum device model to study photovoltaic effect in multi-domain ferroelectric perovskites accounting systematically for the interactions among space charge, polarization, and oxygen octahedra tilts. The model has been successfully implemented numerically. Our results show that there is an electric potential step across each 71° or 109° domain wall, and that this produces a PV effect. There is no electric potential step across a 180° domain wall, and correspondingly no PV effect. Further, the model shows that the direction of current depends on the nature of the domain wall and not the orientation of domains. Therefore, the PV effect becomes additive across multiple domain walls with alternating domains.

We note that the presence of electric potential step across non-180° or the lack of such a step for a 180° domain wall is a generic feature. Consider a generic Devonshire-Landau energy landscape shown in Figure 3.11. Further, consider a non-180° domain wall that separates two ferroelectric domains, one with polarization L and the other with polarization R, as marked in the same figure. These two polarization vectors are spontaneous polarizations, and are thus energy minima of the Devonshire-Landau energy. Now, as the polarization changes from the value L to the value R or vice versa across the domain wall, it will do so along the low energy valley as shown by the red dashed line. This path necessarily involves a change in the component of polarization normal to the domain wall. Therefore, there will indeed be an electric potential step across this domain wall. Note that the electric potential step depends on the path connecting the two polarizations, and this is unchanged if the domains are swapped. This argument is generic because there is no reason in symmetry for the low energy valley to go in a straight line between L and R. A similar argument shows that the lack of such a step for a 180° domain wall is also a generic feature. While the presence or absence of the step is a generic feature, its magnitude and direction depend on the specific energy landscape.

The model and results presented here support the hypothesis that non-180° domain walls contribute to the photovoltaic effect. Importantly, this model does not *a priori* assume the domain wall structure or the electrostatic potential step across it. Instead, this is a prediction of the model that is based on well-established Devonshire-Landau models of ferroelectrics and lumped band models of semiconductors. This model is agnostic about the bulk photovoltaic effect. We could modify our model to include it by coupling the photogeneration to the polarization, but we chose not to do so

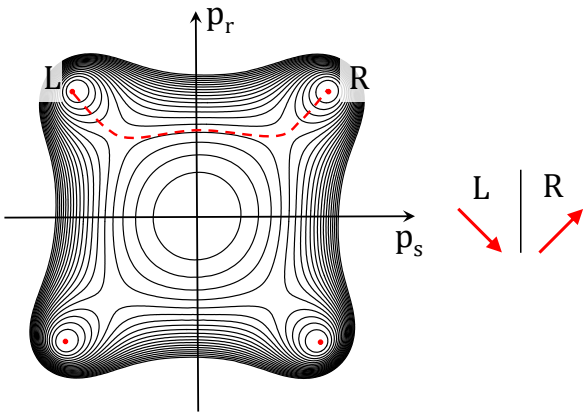

Figure 3.11: The energy landscape of a non-180° domain wall.

since this would not be predictive.

We note that it remains an open question as to why Alexe and Hesse [52] do not see any difference in photocurrent in their AFM-based measurement. One possibility is that the AFM-tip created a depletion zone around it which dominated over the potential step across the domain wall. This can be investigated further by the proposed model, but it requires a multi-dimensional numerical implementation that is a topic of future work.

Finally, we hope that the model presented here as well as the multi-dimensional numerical implementation of it will prove useful for future device designs.

Chapter 4

UNDERSTANDING THE MORPHOTROPIC PHASE BOUNDARY OF PEROVSKITE SOLID SOLUTIONS AS A FRUSTRATED STATE

The work presented in this chapter has been adapted from the following publication:

> Y. S. Teh, J. Li, K. Bhattacharya. Understanding the morphotropic phase boundary of perovskite solid solutions as a frustrated state. *Physical Review B* 103:144201, 2021. doi: 10.1103/PhysRevB.103.144201. https://link.aps.org/doi/10.1103/PhysRevB.103.144201.

4.1 Introduction

Perovskites are materials with a chemical composition ABO_3 (Figure 4.1(a)). Some of these materials undergo a displacive phase transition on cooling from the high temperature perovskite structure to a low temperature low symmetry structure that is not centrosymmetric and thus displays ferroelectricity or ferromagnetism. Therefore these materials are widely used in capacitor, ultrasonic, optical, sensor, actuator, and storage applications for their dielectric, piezoelectric, and ferroelectric properties.

The basic structure is extremely stable, and it is possible to have solid solutions

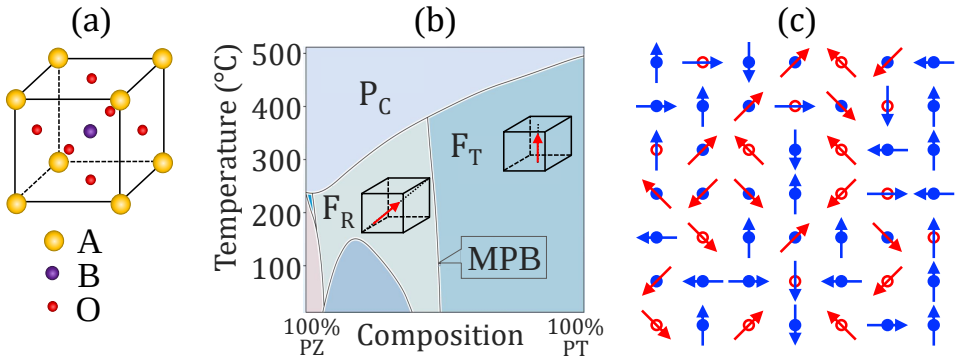

Figure 4.1: PZT and the proposed lattice model. (a) Perovskite structure. (b) Phase diagram of PZT adapted from Cross [4]. F_R, F_T and P_C denote ferroelectric rhombohedral, tetragonal, and paraelectric phases respectively. (c) Schematic illustration of the lattice model proposed in this work.

$A(C_xD_{1-x})O_3$ where two metallic species C and D substitutionally occupy the B site of the lattice. The low temperature structure in these compounds depends on composition and changes across the *morphotropic phase boundary* (MPB) which is largely independent of temperature. Figure 4.1(b) shows the phase diagram of the widely used piezoelectric lead zirconate titanate ($PbZr_xTi_{1-x}O_3$ or PZT) that has a MPB at $x = 0.52$ with a ferroelectric rhombohedral (R3m) structure in the Zr-rich compositions[1] and ferroelectric tetragonal (P4mm) structure in the Ti-rich compositions. The dielectric and piezoelectric properties as well as the ability to pole a ceramic increase dramatically at the MPB [4, 71, 72], and therefore PZT is widely used close to this composition. The search for lead-free dielectric and piezoelectric materials has also focused on solid solutions with MPBs (e.g. Reference [73]).

The nature of the MPB has been extensively studied since the discovery of a bridging monoclinic phase (Cm) at the MPB by Noheda *et al.* [29] using x-ray powder diffraction. It has been suggested that the presence of a bridging phase enables a larger intrinsic [71, 74, 75] and extrinsic [72] piezoelectric effect at the MPB. Since then, various structures have been observed: the combination of two monoclinic phases (Cm and Ic [30] or Cm and Pm [31]), combination of tetragonal (P4mm) and monoclinic (Cm) [32], and combination of rhombohedral (R3m) and monoclinic (Cm) [33]. This uncertainty has been attributed to the disorder in the composition which further results in a disorder in the structure and the difficulty of resolving local structures [76]. This role of disorder is also supported by first principles calculations [77, 78]. This, however, raises the question as to why the disorder does not affect the structure away from the MPB. Another interesting observation concerns the domain patterns. Classical well-defined domain patterns are observed away from the MPB, but highly fragmented domain patterns are observed near the MPB [1]. It has been argued that this fragmented domain pattern also contributes to the high piezoelectric response [79].

In short, critical questions remain open. Why is the effect of compositional disorder suppressed to form an unambiguous structure away from the MPB, but suddenly revealed at the MPB? Is there a definitive crystal structure at the MPB? Why do domain patterns become fragmented near the MPB? Does compositional disorder play a role in the ease of poling at the MPB? Can the MPB be exploited to create new phenomena? These questions have proved to be challenging. The disordered nature of the solid solution requires a large ensemble that takes it beyond the scope

[1] PZT shows a second rhombohedral (R3c) phase at low temperature at high Zr compositions, but we focus on the compositions near the MPB.

of first principles calculations without the introduction of a composition-dependent hybrid pseudopotential [80] that does not include randomness. On the other hand, phase-field Landau-Ginzburg methods can provide insight into domain patterns, but require a phenomenological model of the phase transition.

In this work, we propose a model based on the random-field Ising model with long-range interactions that incorporates the basic elements of the underlying physics. The B sites of a perovskite form a reference cubic lattice that is occupied randomly by atoms of either C or D species. The local quantum mechanical interactions create a propensity for the unit cell to break cubic symmetry depending on the species at the B site. The ferroelectric, ferromagnetic, and ferroelastic polarizations lead to long-range interactions. We create an effective Hamiltonian with these physics.

Our model shows the emergence of a frustrated state. This frustrated state bears resemblance to the spin glass – a magnetic state characterized by randomness – that has been widely studied in the past decades. One of the earliest spin glass models is the Edwards-Anderson model [81]. It contains only nearest neighbor exchange interactions similar to the classical Ising model, but the exchange constants are randomly selected according to a probability distribution to depict the randomly mixed ferromagnetic and antiferromagnetic bonds. The infinite-range version of this model with two-spin interactions is the Sherrington-Kirkpatrick model [82]. The model can be solved using the mean field approach and has also been used in understanding other phenomena including tweed formation in martensitic transformations [83]. Aside from these bond-disordered models, site-disorder models such as the Mattis model and its variants [84] have also been proposed. Another related work is the Coulomb glass model that comprises of both disorder and long-range Coulomb interactions between electrons [85]. This model is used to study the gap in the density of states of doped crystalline semiconductors, as well as the underlying glasslike order, phase transition, and critical exponents [86, 87]. In our model, the frustrated state emerges only at a narrow range of composition and therefore manifests itself as the MPB. We study how this arises from the competition between different energy terms.

Specifically, we present our model and its implementation in the context ferroelectric solid solutions in Sections 4.2 and 4.3. In Section 4.4, we show that our model provides insights to the questions concerning the MPB of ferroelectric solid solutions like PZT. In particular, the long-range interactions overwhelm the local disorder in the C-rich and D-rich compositions with the exchange of stability taking place at

a specific composition corresponding to the MPB where the material is frustrated. The frustrated state also enables easy poling as observed. In Sections 4.5 and 4.6, we adapt our model and its implementation to explore the possibility of obtaining a strongly coupled multiferroic material system (Section 4.7) using the insights obtained from Section 4.4. Finally, we conclude in Section 4.8.

4.2 Model for ferroelectric materials

Consider a d-dimensional periodic lattice ($d = 2$ or 3) with N lattice points as shown in Figure 4.1(c). Each lattice point i is characterized by fixed (quenched) chemical composition (c_i) of either type C ($c_i = 0$ indicated by a red open circle in Figure 4.1(c)) or type D ($c_i = 1$ indicated by a blue closed circle). Each lattice point carries a dipole state ($\boldsymbol{p}_i$ indicated by the arrows in Figure 4.1(c)) that can take one of a number of orientations $\mathcal{C} \cup \mathcal{D}$ determined by the Hamiltonian

$$W(\{\boldsymbol{p}_i\};\{c_i\}) = \sum_{i=1}^{N} h_i - \frac{1}{2}\sum_{<i,j>} J_{e_{ij}}\boldsymbol{p}_i \cdot \boldsymbol{p}_j + W_e. \tag{4.1}$$

The first term encodes the information that lattice site of type C (respectively, D) energetically prefers the set of dipole states $\mathcal{C}$ indicated by the red arrows (respectively, $\mathcal{D}$ indicated by the blue arrows), though they can take states in $\mathcal{D}$ (respectively, $\mathcal{C}$) with an energetic cost $h_{\mathcal{CD}} > 0$ (respectively, $h_{\mathcal{DC}} > 0$):

$$h_i = \begin{cases} h_{\mathcal{CD}} & c_i = 0 \;\&\; \boldsymbol{p}_i \in \mathcal{D}, \\ h_{\mathcal{DC}} & c_i = 1 \;\&\; \boldsymbol{p}_i \in \mathcal{C}, \\ 0 & \text{otherwise.} \end{cases} \tag{4.2}$$

The second term, where the sum is limited to nearest neighbors, is the exchange energy. Ferroelectricity requires noncentrosymmetric displacements of ions which arise from a delicate balance between short-range repulsions of electron clouds and the short-range portion of the Coulomb interaction with a range of the lattice constant [88]. The exchange term captures this net ferroelectric effect as it promotes like neighbors when the exchange constant $J_{e_{ij}} > 0$. The exchange constant in this model is composition-dependent and takes the form of

$$J_{e_{ij}} = \frac{1}{2}[J_e(c_i) + J_e(c_j)], \quad J_e(c) = \begin{cases} J_e^{\mathcal{C}} & c = 0, \\ J_e^{\mathcal{D}} & c = 1. \end{cases} \tag{4.3}$$

The third term represents the electrostatic contribution that includes the long-range dipole-dipole interaction scaled by D_e (which incorporates the dipole strength, lattice

constant, and electromagnetic constants) and the influence of the applied external electric field $\mathbf{E}$. As the dipole-dipole term for the two-dimensional case is not found in the literature, we derive it in Appendix C.1 and show the final expression obtained here.

$$\begin{aligned} W_e &= W_{em}(\{\boldsymbol{p}_i\}, D_e, \mathbf{E}) \\ &:= D_e \Bigg\{ \underbrace{\frac{1}{(d-1)} \sum_{i,j=1}^{N} {\sum_{\mathbf{R}}}' \frac{1}{x_{ij}^d} \left[\boldsymbol{p}_i \cdot \boldsymbol{p}_j - \frac{d(\boldsymbol{p}_i \cdot \mathbf{x}_{ij})(\boldsymbol{p}_j \cdot \mathbf{x}_{ij})}{x_{ij}^2} \right]}_{W_{dip}^0} + \underbrace{\frac{2\pi}{d} \sum_{i=1}^{N} |\boldsymbol{p}_i|^2}_{W_{dip}^{self}} \Bigg\} \\ &\quad - \mathbf{E} \cdot \sum_{i}^{N} \boldsymbol{p}_i. \end{aligned} \tag{4.4}$$

Given a lattice where the composition of each site is randomly assigned subject to a fixed average, we use a Markov chain Monte Carlo (MCMC) method with cooling to obtain the equilibrium distribution at a given temperature. The state is initialized by randomly assigning a polarization from $C \cup \mathcal{D}$. Adapting the Metropolis-Hastings algorithm to our multistate setting, a site is chosen at random, and its dipole state is updated to one of the N_s states according to the transition probability

$$P_s = \frac{\exp(-\beta W^{(s)})}{\sum_{r=1}^{N_s} \exp(-\beta W^{(r)})}, \qquad s = 1, ..., N_s \tag{4.5}$$

where β is the inverse temperature and N_s is the cardinality of $C \cup \mathcal{D}$. We choose the transition probability of the form (4.5) so as to satisfy the detailed balance condition which is a sufficient condition for an equilibrium distribution. More details can be found in Appendix B. Further, we avoid the system getting trapped in local minima at low temperatures by starting at a high temperature ($\beta = 0$) and slowly cooling (increasing β) to the temperature of interest, while performing enough MCMC steps to reach equilibrium at each temperature. Algorithm 1 provides a summary of the method.

Algorithm 1 Markov chain Monte Carlo with cooling

Initialize dipole states $\{\boldsymbol{p}_i\}_{i=1}^N$
Initialize $\beta = 0$
while $\beta < \beta_{max}$ **do**
  for iteration $= 1, \ldots, \theta_{max}$ **do**
    Select lattice point i at random
    Compute energy $\Delta W^{(s)}$ for $s = 1, \ldots, N_{states}$
    Update $\boldsymbol{p}_i$ according to transition probabilities P_s
  end for
  $\beta \leftarrow \beta + \Delta\beta$
end while

4.3 Implementation for ferroelectric materials

We note that the dipole-dipole energy term in (4.4) is only conditionally convergent; it is not feasible to compute the term as it is. Hence we take two important steps as detailed below to ensure an accurate and efficient computation of the dipole-dipole energy.

First, we adopt Ewald summation [89–91] to separate the first term (W_{dip}^0) of expression (4.4) into a short-range contribution that converges rapidly in real space (W_{dip}^r), a long-range contribution that converges rapidly in Fourier space (W_{dip}^k), a self energy ($W_{dip}^{k\_self}$), and a surface term (W_{dip}^{surf}) that depends on the boundary condition. In other words, we rewrite the first term as

$$\begin{aligned} W_{dip}^0 &:= \frac{1}{(d-1)} \sum_{i,j=1}^{N} {\sum_{\mathbf{R}}}' \frac{1}{x_{ij}^d} \left[\boldsymbol{p}_i \cdot \boldsymbol{p}_j - \frac{d(\boldsymbol{p}_i \cdot \mathbf{x}_{ij})(\boldsymbol{p}_j \cdot \mathbf{x}_{ij})}{x_{ij}^2} \right] \\ &= W_{dip}^r + W_{dip}^k - W_{dip}^{k\_self} + W_{dip}^{surf}, \end{aligned} \tag{4.6}$$

where

$$W_{dip}^r = -\frac{1}{2} \sum_{i,j=1}^{N} {\sum_{\mathbf{R}}}' (\nabla_{\mathbf{x}_i} \cdot \boldsymbol{p}_i)(\nabla_{\mathbf{x}_j} \cdot \boldsymbol{p}_j) G_r(|\mathbf{x}_i - \mathbf{x}_j - \mathbf{R}|), \tag{4.7}$$

$$W_{dip}^k = -\frac{1}{2V} \sum_{\substack{\mathbf{k} \neq \mathbf{0} \\ \mathbf{k} \in \mathbb{K}^d}} |\widetilde{\boldsymbol{p}}(\mathbf{k}) \cdot i\mathbf{k}|^2 \widetilde{G}_\sigma(\mathbf{k}), \tag{4.8}$$

$$W_{dip}^{k\_self} = \frac{1}{d(2\pi)^{d/2-1}\sigma^d} \sum_{i=1}^{N} |\boldsymbol{p}_i|^2, \tag{4.9}$$

$$W_{dip}^{surf} = \frac{2^{d-1}\pi}{d(d-1)V} \left| \sum_{i=1}^{N} \boldsymbol{p}_i \right|^2, \tag{4.10}$$

with

$$G_r(r) = \begin{cases} \mathrm{Ei}\left(-\frac{r^2}{2\sigma^2}\right), & d = 2 \\ -\frac{1}{r}\mathrm{erfc}\left(\frac{r}{\sqrt{2}\sigma}\right), & d = 3 \end{cases},$$
$$\widetilde{G}_\sigma(\mathbf{k}) = -\frac{4\pi}{k^2}\exp(-k^2\sigma^2/2),$$

$\widetilde{\boldsymbol{p}}(\mathbf{k})$ the discrete Fourier transform of $\boldsymbol{p}$, $\mathbb{K}^d$ the Brillouin zone, and σ a parameter chosen to be sufficiently large to keep the calculation of W^k_{dip} tractable but small enough such that the W^r_{dip} term is negligible and can be simply disregarded. A vacuum boundary condition is selected in the surface term above so that the formation of domains can be observed. In the context of a periodic system like our case, this would be the boundary condition at infinity. Interested readers may refer to Appendix C.2 for the full derivation.

Second, notice that for any flip, $\Delta W^0_{dip} \approx -\mathbf{E}^{dip}_i \cdot \Delta \boldsymbol{p}_i$ where $\mathbf{E}^{dip}_i = -\nabla_{\boldsymbol{p}_i} W^0_{dip}$ is the electric field. While the long-range nature of the dipole-dipole interaction means that $\mathbf{E}^{dip}_i$ has to be recomputed after each flip, the error is small for individual flips. Therefore we update $\mathbf{E}^{dip}_i$ only every $\sqrt{N}$ flips where N is the size of the supercell lattice. We can then perform $\sqrt{N}$ flips independently and in parallel thereby enabling acceleration on a graphical processing unit (GPU). Further, $\mathbf{E}^{dip}_i$ is readily computed using fast Fourier transforms (FFT) which can also be implemented on GPUs.

Specifically, the electric field at lattice point $\mathbf{x}_i$ due to other dipoles is

$$\mathbf{E}^{dip}_i = -\nabla_{\boldsymbol{p}_i} W^0_{dip} = \mathbf{E}^k_i - \mathbf{E}^{k\_self}_i + \mathbf{E}^{surf}_i. \tag{4.11}$$

The difficult term is $\mathbf{E}^k_i$. Due to the exponential decay in $\tilde{G}_\sigma(\mathbf{k})$, we may limit the summation over all $\mathbf{m} \in \mathbf{Z}^d$ to $\{\mathbf{m} \in \mathbb{Z}^d, -M_{cut}/2 \le m_i < M_{cut}/2\}$ and

$$\mathbf{E}^k_i = \frac{4\pi}{V} \sum_{\mathbf{k}\in\widetilde{\mathbb{M}}^d} \widetilde{\boldsymbol{p}}(\mathbf{k}) \cdot \underbrace{\left(\sum_{\mathbf{m}\in\mathbb{Z}^d} \mathbf{g}(\mathbf{k} + 2\pi\mathbf{m}) \right)}_{\boldsymbol{A}(\mathbf{k})} \exp(i\mathbf{k}\cdot\mathbf{x}_i), \tag{4.12}$$

$$\mathbf{g}(\mathbf{k}_\mathbf{m}) = \begin{cases} \mathbf{0} & \text{if } \mathbf{k}_\mathbf{m} = \mathbf{0}, \\ \mathbf{k}_\mathbf{m} \otimes \mathbf{k}_\mathbf{m} \widetilde{G}_\sigma(\mathbf{k}_\mathbf{m}) & \text{otherwise.} \end{cases}$$

Note that we can precompute $\boldsymbol{A}(\mathbf{k})$ and exploit FFT to obtain an efficient algorithm: (i) FFT to compute $\widetilde{\boldsymbol{p}}(\mathbf{k})$, (ii) multiplication with pre-computed $\boldsymbol{A}$, and (iii) inverse FFT to obtain $\mathbf{E}^k_i$ in real space. See Algorithm 2. We use the highly parallelized `cufft` and `curand` libraries in CUDA-based GPU programming to perform FFT and generate random numbers.

Algorithm 2 GPU-accelerated computational method

1: Initialize dipole states $\{\boldsymbol{p}_i\}_{i=1}^N$
2: Initialize $\beta = 0$
3: **while** $\beta < \beta_{max}$ **do**
4: **for** iteration $= 1, \ldots, \theta_{max}$ **do**
5: Construct $\{\boldsymbol{p}_i\}_{i=1}^N$
6: Perform FFT of $\{\boldsymbol{p}_i\}_{i=1}^N$ to obtain $\widetilde{\boldsymbol{p}}(\mathbf{k})$
7: Perform pointwise multiplication with $\boldsymbol{A}$ tensor
8: Perform inverse FFT to obtain $\{\mathbf{E}_i^k\}_{i=1}^N$
9: Determine $\{\mathbf{E}_i^{surf}\}_{i=1}^N$ using parallel sum reduction, and compute the net electric field $\mathbf{E}_i = \mathbf{E}_i^{dip} + \mathbf{E}$
10: Generate $\sqrt{N}$ number of lattice points at random and perform MC updates on these points in parallel with $\Delta W = -\mathbf{E}_i \cdot \Delta \boldsymbol{p}_i + \Delta W_{dip}^{self} + \Delta W_{local} + \Delta W_{exchange}$
11: **end for**
12: $\beta \leftarrow \beta + \Delta\beta$
13: **end while**

Performance on GPU

We evaluate the performance of our proposed algorithm (Algorithm 2) on GPU and compare it to that on CPU. This is done using the example of PZT and the details will be specified in the beginning of Section 4.4.

Figure 4.2 shows the performance of the algorithm when running on one GPU (Nvidia P100) as compared to when running the sequential version on one CPU core on Intel Xeon (2.4Hz). The speedup measured is much more significant for larger lattice sizes. At a lattice size of 256 by 256, we measure a speedup of 16.5X. When considering the run times task-by-task, FFT and inverse FFT– the two most computationally expensive tasks in the algorithm– experience a reduction in run time by at least 20 folds (Figure 4.2c). The reduction is less significant for task 6 (i.e. step 10 in Algorithm 2) as the Monte Carlo update at lattice points is comparatively less amenable to parallelism. Nonetheless, there is still considerable speedup that can be reaped overall using a GPU implementation.

4.4 Results for ferroelectric materials

We study an example motivated by PZT though the results are generic. Here, the C and D lattice points represent lead zirconate (PZ) and lead titanate (PT) unit cells containing Zr and Ti atoms, respectively. Recall that the former prefers

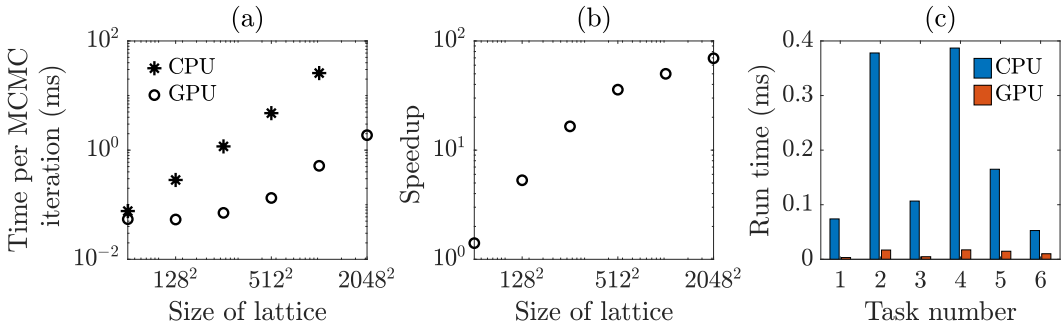

Figure 4.2: Performance of Algorithm 2 on one GPU versus on one CPU core. (a) Time taken for one MCMC iteration (which comprises of steps 5 to 10 in Algorithm 2) on different 2D lattice sizes. (b) A replot of (a) showing the speedup obtained when running the algorithm on one GPU relative to one CPU core. (c) Comparison of run time for each of tasks 1 to 6, corresponding to each step in one MCMC iteration.

rhombohedral or $\langle 111 \rangle$ polarization states while the latter prefers tetragonal or $\langle 100 \rangle$ polarization states. We consider two dimensions $d = 2$ so that $\mathcal{C} = (p_o^{\mathcal{C}}/\sqrt{2})\{[1,1],[1,-1],[-1,1],[-1,-1]\}$ while $\mathcal{D} = p_o^{\mathcal{D}}\{[1,0],[0,1],[-1,0],[0,-1]\}$. Unless otherwise specified, we set $p_0^{\mathcal{C}} = p_0^{\mathcal{D}} = h_{\mathcal{CD}} = h_{DC} = J_e^{\mathcal{C}} = J_e^{\mathcal{D}} = D_e = 1$, unit lattice distance between any two nearest neighboring sites, Ewald parameters $\sigma = 0.157$ and $M_{cut} = 16$, and conduct our simulations on a 256^2 lattice. The lattice size is chosen to be sufficiently large upon convergence studies to depict randomness in composition as well as for us to visualize domain formation. More details will be presented later in this section. In each simulation, we begin with an inverse temperature of $\beta = 0$, and repeatedly increase its value with a small step size of $\Delta\beta = 0.05$ until we reach $\beta = 5$. At each temperature value, at least 2000 Monte Carlo (MC) sweeps (each sweep consists of $N = 256^2$ steps) are performed with a total of approximately 2×10^5 sweeps.

Main results

Figure 4.3 shows the results of these simulations. Figure 4.3(a) shows the evolution of the order parameter ($\xi = \frac{1}{\kappa_{max}} \sum_{\kappa=1}^{\kappa_{max}} \kappa C(\kappa)$ where $C(\kappa) = \langle \boldsymbol{p}_i \cdot \boldsymbol{p}_j \rangle$ is the correlation function over any two sites i and j that satisfy $\kappa - 1 < |\mathbf{x}_i - \mathbf{x}_j| \leq \kappa$) in a series of simulations with varying average composition. The material is disordered at high temperature, but becomes ordered at low temperatures. The phase transition is somewhat diffuse due to the compositional disorder. Figure 4.3(b) shows the nature of the ordered phase. Remarkably, we find that all dipoles are in the rhombohedral

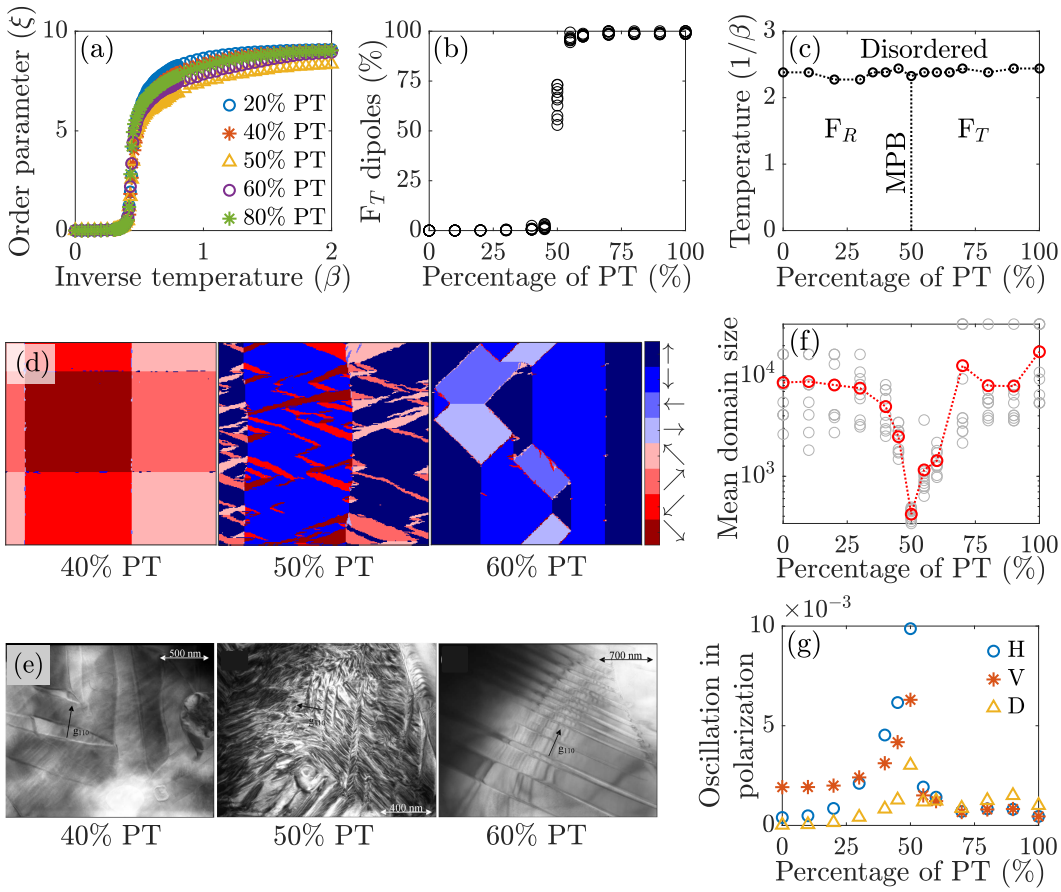

Figure 4.3: Emergence of a morphotropic phase transition (MPB) as a competition between short-range (compositional) disorder and long-range (exchange and electrostatic) interactions. (a) Order parameter versus inverse temperature for various compositions. (b) Dipole orientation in the ordered phase at various compositions. (c) Phase diagram showing the MPB. (d) Domain patterns at various composition. (e) Experimentally observed domain patterns at various compositions (reprinted with permission from Woodward, Knudsen, and Reaney [1]). (f) Average domain size versus composition (average (red) and ten realizations (gray)). Domain size is computed using breadth first search, and domains with width or length of not more than 2 units (which are typically domain walls) are excluded. (g) Small-scale oscillations in terms of the finest Haar wavelet horizontal (H), vertical (V), and diagonal (D) detail coefficients versus composition.

(C) states until a critical composition of about 50% beyond which all dipoles are in the tetragonal ($\mathcal{D}$) states. Indeed, at a composition of 33.3%, a third of the sites would prefer tetragonal dipoles. However, the exchange and electrostatic interaction with the neighbors overwhelm this preference and instead force it into the rhombohedral state. The opposite happens at a composition of 66.7%. The exchange of stability between the rhombohedral and tetragonal states takes place at

a well-defined critical composition. This observation is extremely robust: Figure 4.3(b) includes results from 10 realizations. In short, we see the *emergence of the morphotropic phase boundary* (MPB). Remarkably, the disorder is completely suppressed at all compositions except the MPB.

The resulting phase diagram is shown in Figure 4.3(c) (where the order-disorder transition temperature is taken to be that of the maximum curvature of the $\xi - \beta$ curve). It is structurally consistent with experimental observations with the paraelectric phase at high temperature and different ordered phase at low temperatures depending on composition. The details depend on the parameters as we shall show later.

The resulting domain patterns are also interesting. Figure 4.3(d) shows the typical domain patterns at three different compositions. We see the 2D analogs of 71° or 109° domain walls with (10) normals at a composition of 40%, and we see the 2D analog of 90° domain walls with (11) normals at a composition of 60%. However, at the MPB (composition 50%), we see a mixture of rhombohedral ($\mathcal{C}$) and tetragonal ($\mathcal{D}$) states with a highly fragmented and frustrated domain pattern.

Figure 4.3(f) shows that the average domain size falls precipitously at the MPB compared to that at all other compositions. Figure 4.3(g) shows that the oscillations in polarization in the horizontal, vertical, and diagonal directions are also magnified at the MPB. Specifically, we take the Haar wavelet transform of each domain pattern, which is represented in terms of a two-dimensional matrix $\mathbf{X}$ using different numbers from 1 to 8 to denote different dipole states. Figure 4.4 shows an example of the results obtained from the Haar wavelet decomposition at level one (the finest level), in which the horizontal ($\mathbf{H}_1$), vertical ($\mathbf{V}_1$), and diagonal ($\mathbf{D}_1$) detail coefficients trace the domain walls of the corresponding orientations. Since the relation $||\mathbf{X}||^2 = ||\mathbf{A}_1||^2 + ||\mathbf{H}_1||^2 + ||\mathbf{V}_1||^2 + ||\mathbf{D}_1||^2$ holds with $\mathbf{A}_1$ being the approximation coefficients [92], it is natural to consider the normalized sum of squares of the detail coefficients (i.e. $||\mathbf{H}_1||^2/||\mathbf{X}||^2$, $||\mathbf{V}_1||^2/||\mathbf{X}||^2$ and $||\mathbf{D}_1||^2/||\mathbf{X}||^2$) as a method to quantify the proportion of the domain walls in different orientations. Figure 4.3(g) shows these normalized quantities averaged over 10 realizations. The Haar wavelet decomposition can also be employed to approximate the average domain size similar to Figure 4.3(f), which we will show in Appendix D.

All these observations are consistent with experimental observations. Figure 4.3(e) reproduces the experimental observations of Woodward, Knudsen, and Reaney [1]: classical well-defined domain patterns are observed away from the MPB, but highly

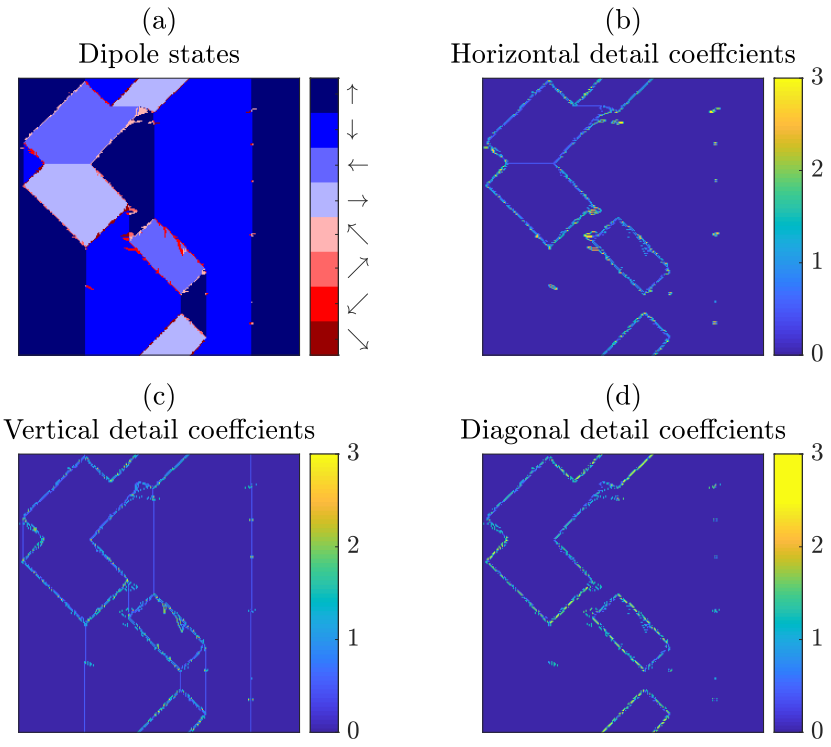

Figure 4.4: Level one Haar wavelet decomposition results. (a) Simulated dipole orientation (reproduced from Figure 4.3(d)). (b), (c), and (d) show the absolute values of the horizontal, vertical, and diagonal detail coefficients obtained from the wavelet decomposition of the dipole states in (a).

fragmented domain patterns are observed near the MPB as in our simulations (Figure 4.3(d)). We note that the fragmented patterns in our simulations at the MPB are found to be angled at around 22.5° to accommodate the divergence-free rotation of dipole states across the boundary when changing from a tetragonal state to a rhombohedral state or vice versa. Such domain walls typically do not exist in three dimensions leading to further fragmentation [42].

Verification of convergence with respect to lattice size

As we use a periodic lattice to represent a solid solution and its compositional disorder, one may wonder if a periodic lattice size of 256^2 is sufficient for convergence of results. Figure 4.5 shows the dipole orientations obtained when different lattice sizes are used for the simulations. We find that a small lattice size of 64^2 fails to capture the complex phase structure at the MPB. The phase structure starts to stabilize and small-sized domains become visible when increasing the lattice size to 128^2. At a large lattice size of 512^2 (Figure 4.5(c)), the microstructure at the MPB looks similar and is of the same scale as those of 256^2 in Figure 4.3(d). This

justifies our choice of 256^2.

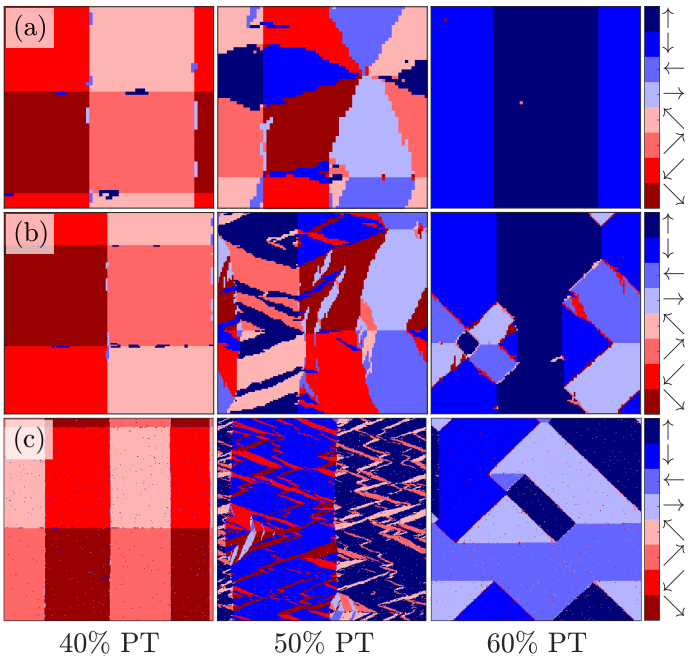

Figure 4.5: Dipole orientations at various compositions when lattice sizes of (a) 64^2, (b) 128^2, and (c) 512^2 are used. Due to the slow computational time for (c), the dipole states are relaxed up to an inverse temperature of $\beta = 2.5$ instead of $\beta = 5$.

Importance of disorder and long-range interaction

Examining our simulation results more closely, we identify that both the long-range interaction and the disorder in composition are necessary for the emergence of the MPB.

In the absence of the long-range dipole-dipole interaction (i.e., when $D_e = 0$), the average number of dipoles track the composition as shown in Figure 4.6(a). Recall that the lower critical dimension of a two-state random-field Ising model is two, that is, the lattice remains disordered even at low temperatures [93–95]. We follow a scaling-type argument to confirm that the statement also applies to our multistate model (see below). This is consistent with the observations in the first row of Figure 3b where the material remains disordered. We see some domains, with $\mathcal{C}-$rich states and $\mathcal{D}-$rich states and meandering domain walls. However, the microstructure is still disordered with all states present, and domains with $\mathcal{C}-$rich and $\mathcal{D}-$rich states co-exist. This is why the average number of dipoles track the composition. Crystallographically distinguished domain walls arise with small D_e and become sharper as it increases (Figure 4.6(b)) along with a complete suppression

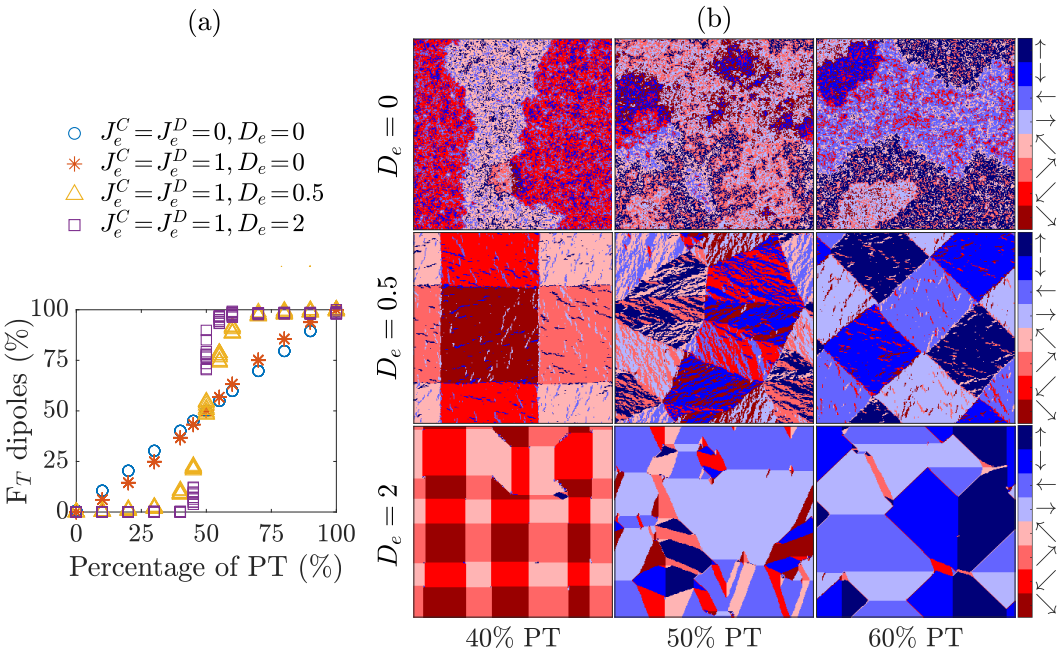

Figure 4.6: The effect of different dipole-dipole interaction strength D_e. (a) and (b) show the dipole orientation and domain patterns in the ordered phase at various compositions and D_e values. $J_e^C = J_e^D = 1$ in (b).

of the disorder within the domains. Finally, at large D_e, we see less fragmented domains at the MPB because the role of disorder becomes comparably smaller.

The complex domain patterns at the MPB also do not appear when the composition is not random. This can be seen in the two examples in Figure 4.7 where the compositions comprise of 50% PZ and 50% PT, but are void of randomness.

Claim: There is a lack of long-range order in a multistate random-field Ising model when the dimension is $d \leq 2$.

Proof by scaling-type argument.

Following the simple scaling-type argument in [93], it can be shown that there is a lack of long-range ordering for dimension $d \leq 2$ in the absence of the dipole-dipole interaction term. Here we adapt the argument to show that the same statement applies to our PZT model when $D_e = 0$. For convenience, we denote $h = h_{C\mathcal{D}} = h_{DC}$ and $J_e = J_e^C = J_e^D$.

Consider neighboring domains of linear size $\sim L$ in lattice unit. The domain wall energy or the so-called surface energy is $kL^{d-1}J_e p_0^2 \cos\theta$, i.e. $O(L^{d-1}J_e)$, where k is a constant associated with the shape of the domain, p_0 is the magnitude of the dipole state, and θ is the change in angle of the dipoles across the domain wall. Let $H = \sum_{i \in L^d} h_i$ denote the sum of local energy within each domain. This is also called the bulk energy. It can be shown that the value of H fluctuates from one domain to another with $\langle \Delta H^2 \rangle \sim h^2 L^d$. To show this, note that the overall system size is much larger than the domain size L^d. Therefore it can be assumed that the probability of each lattice site having composition PT (type D) is the same as the fraction of PT sites in the overall system. Let us denote this fraction as λ. With this assumption, the distribution of the values of H/h for different domains then follows a binomial distribution with probability λ and number of selections L^d. It is known that the variance of the distribution is given by $L^d\lambda(1-\lambda)$, hence $\langle \Delta H^2 \rangle \sim L^d h^2$.

By splitting into domains of linear size L, the system will gain a bulk energy of $O(L^{d/2}h)$ and lose a surface energy of $O(L^{d-1})J_e$ per domain. When $d \leq 2$, there exists a sufficiently large L such that it is energetically favorable to decompose the system into domains of that size (in other words, to become disordered) even for relatively small random field h compared to the exchange field J_e.

More parameter studies

Figure 4.8 shows how the phase diagram changes as we change the relative magnitudes of $h_{C\mathcal{D}}$, h_{DC} and J_e^C, J_e^D, while keeping their averages the same. The columns show that the order-disorder transformation temperature becomes composition dependent when $J_e^C \neq J_e^D$ with the slope of the transition temperature dependent on the relative magnitudes of J_e^C and J_e^D, while the rows show that the MPB composition

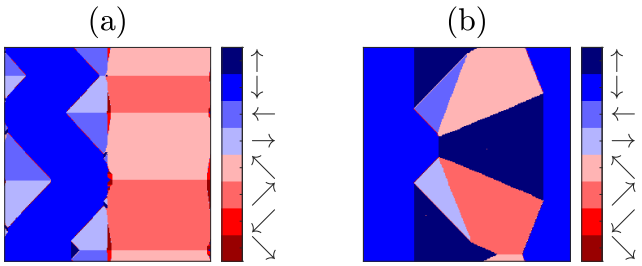

Figure 4.7: Domain patterns obtained when (a) the composition is separated with PZ (C) sites on the left side and PT (D) sites on the right side, and (b) the composition is regularly alternating (that is, it has a checkerboard pattern). Note that complex domain patterns do not appear in these two cases.

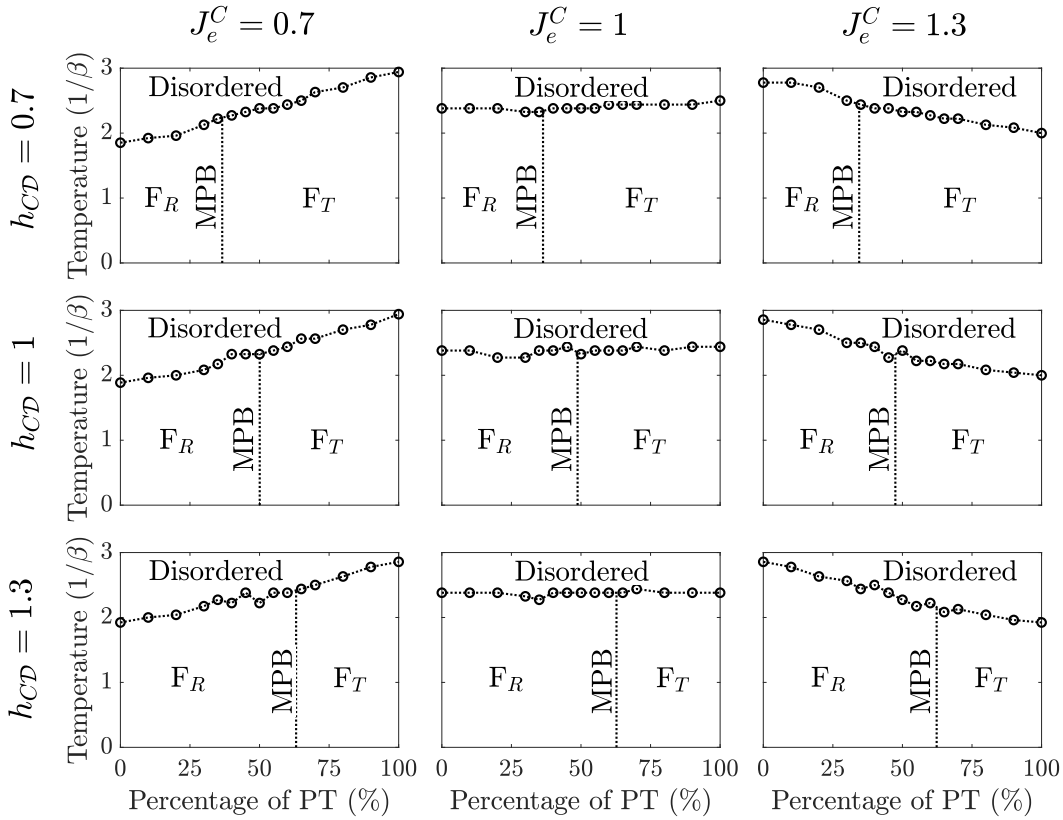

Figure 4.8: The effect of different energetic penalties and exchange constants for different composition types of phase diagram. $h_{C\mathcal{D}}$ and J_e^C are varied with both $(h_{C\mathcal{D}} + h_{DC})/2$ and $(J_e^C + J_e^D)/2$ kept constant at 1.

depends critically on the relative magnitude of $h_{C\mathcal{D}}$ and h_{DC}. Figure 4.9 shows that the MPB composition also depends sensitively on the relative polarization magnitudes p_0^C and p_0^D.

An explicit solution of this problem remains open, but we can understand various

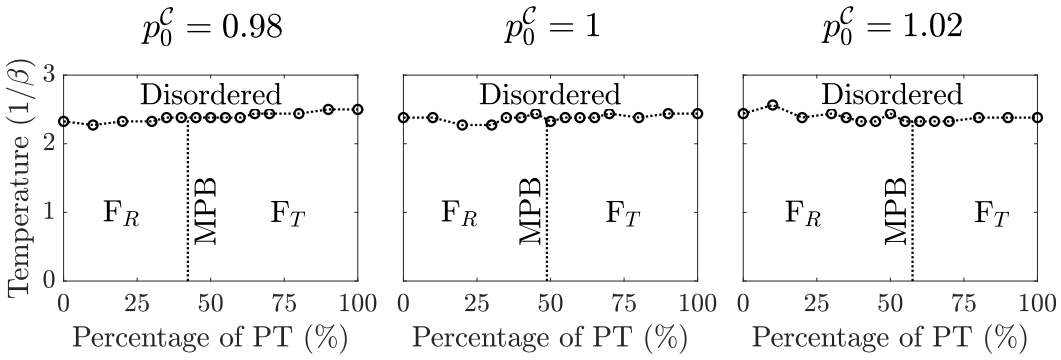

Figure 4.9: The effects of dipole magnitude $(p_0^{\mathcal{C}}, p_0^{\mathcal{D}})$. $p_0^{\mathcal{C}}$ is varied with $(p_0^{\mathcal{C}} + p_0^{\mathcal{D}})/2$ kept constant at 1.

aspects qualitatively. We first consider the order-disorder phase transition temperature T_c. Recall that according to the Onsager solution to the (two-state) Ising model on a square lattice, $T_c = 2J_e/\ln(1+\sqrt{2}) = 2.27$ for $J_e = 1$. At the two pure end states, there is no disorder, but we differ from the Ising model in two important ways. First, we have eight allowable states and we expect this to depress T_c. Second, we have dipole-dipole interactions; the energy due to this is high in the disordered state, but is driven to almost zero by the formation of domains in the ordered states. Consequently, we expect the T_c to increase with D_e. We have confirmed this: For $J_e^C = J_e^D = 1$, we find T_c to be $1.3, 2.0, 2.3, 2.9$ for $D_e = 0, 0.5, 1, 2$, respectively, for the end states. In any case, for D_e fixed, we expect T_c to be proportional to J_e as we see in Figure 4.8 for the end states. In fact, this is also true in the intermediate compositions since the disorder in chemical composition has little effect on T_c. The average J_e is $(1-\lambda)J_e^C + \lambda J_e^D$ for a disordered lattice with volume fraction λ of D sites. Consequently, we expect T_c to be proportional to λ as we see in Figure 4.8.

We now turn to the MPB composition λ_c. We consider a very low temperature where the entropy can be neglected. Since the dipole-dipole energy suppresses the disorder, we simply need to compare the energy between the configuration where every lattice point is in a $\mathcal{C}$ state with one where every lattice point is in a $\mathcal{D}$ state. Further, the formation of domains can reduce the dipole-dipole energy. Therefore, to leading order, the energy in these configurations is

$$\begin{cases} W^{\mathcal{C}} = \lambda h_{DC} - 2[(1-\lambda)J_e^C + \lambda J_e^D](p_0^{\mathcal{C}})^2, \\ W^{\mathcal{D}} = (1-\lambda)h_{C\mathcal{D}} - 2[(1-\lambda)J_e^C + \lambda J_e^D](p_0^{\mathcal{D}})^2. \end{cases} \tag{4.13}$$

Equating the two, we obtain

$$\lambda_c = \frac{h_{C\mathcal{D}} + 2J_e^C[(p_0^C)^2 - (p_0^{\mathcal{D}})^2]}{h_{C\mathcal{D}} + h_{DC} + 2(J_e^C - J_e^D)[(p_0^C)^2 - (p_0^{\mathcal{D}})^2]} \,. \tag{4.14}$$

This is consistent with the results in Figures 4.8 and 4.9. For example, in the middle column of Figure 4.8 where $J_e^C = J_e^D = p_0^C = p_0^{\mathcal{D}} = 1$, $\lambda_c = h_{C\mathcal{D}}/(h_{C\mathcal{D}} + h_{DC}) = h_{C\mathcal{D}}/2$ which is $0.35, 0.5, 0.65$ in the three rows. In Figure 4.9, $h_{C\mathcal{D}} = h_{DC} = J_e^C = J_e^D = 1$, so $\lambda_c = 1/2 + 2(p_0^C - p_0^{\mathcal{D}})$ which is $0.42, 1, 0.58$ in the three cases.

Some results in 3D

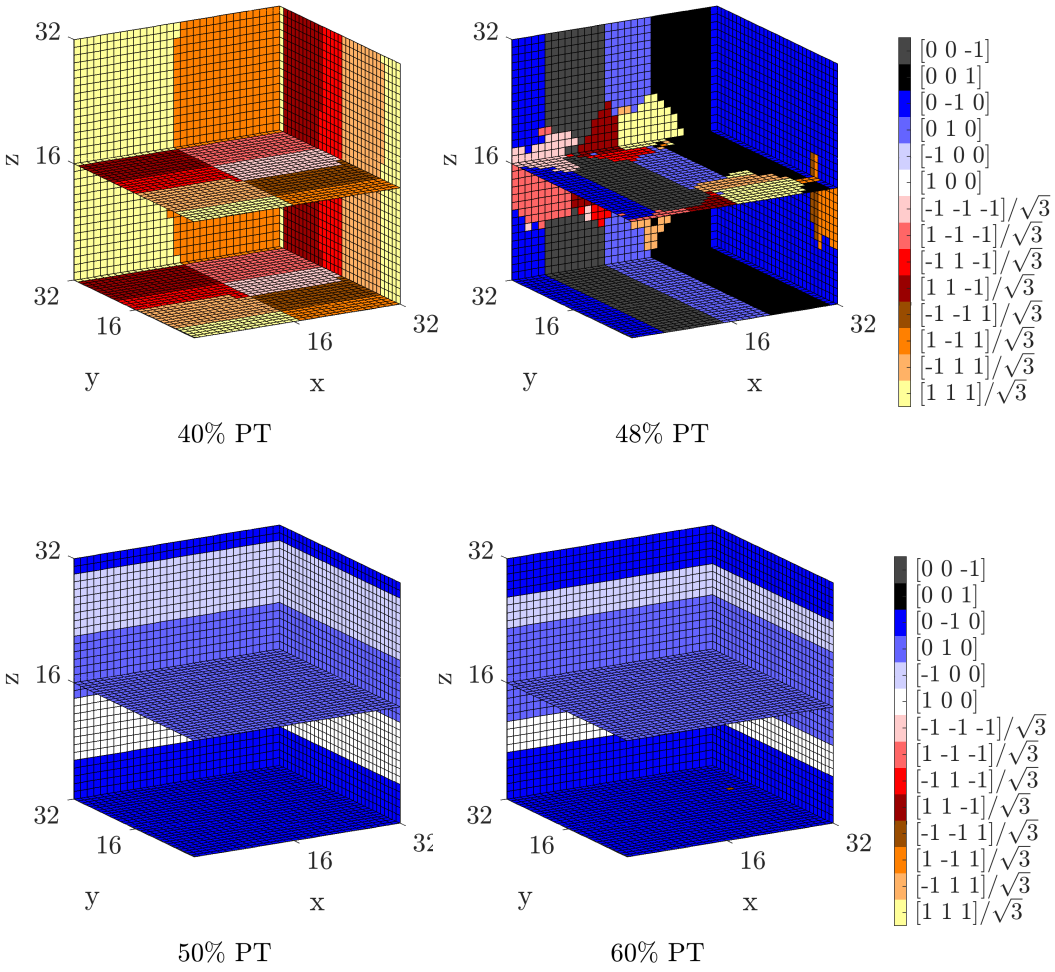

Figure 4.10: Domain patterns at various compositions for 3D simulations ($h_{C\mathcal{D}} = h_{DC} = 1, J_e^C = J_e^D = 0.5, D_e = 1$). Due to the much higher computational costs of the 3D simulations, these are performed using a small lattice size of 32^3.

The situation is largely similar with some difference in detail in three dimensions. Similarly to the 2D simulations, rhombohedral dipole states dominate at 40% PT

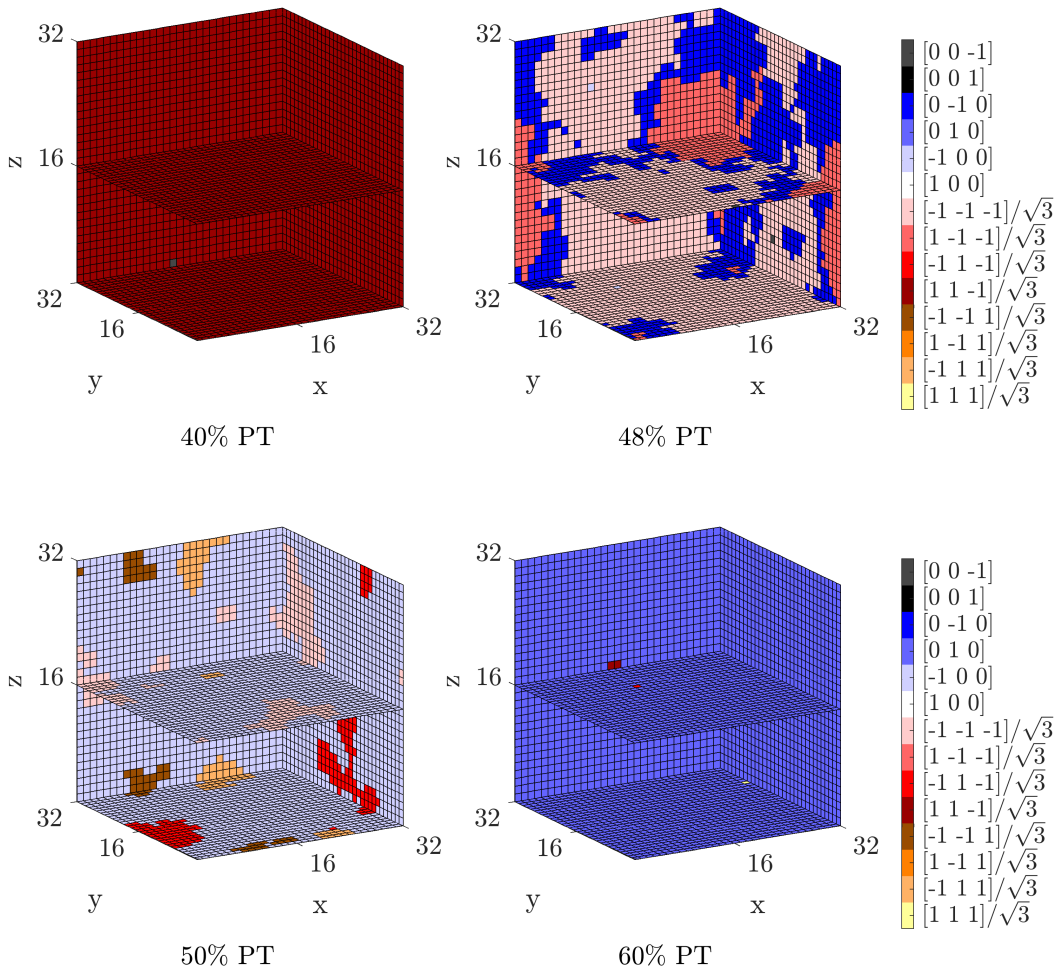

Figure 4.11: Domain patterns at various compositions for 3D simulations in the absence of dipole-dipole interactions ($h_{C\mathcal{D}} = h_{DC} = 1, J_e^C = J_e^D = 1, D_e = 0$).

composition while tetragonal dipole states dominate at 60% PT composition as shown in Figure 4.10. At a composition of 48%, we see the emergence of the morphotropic phase boundary (MPB). The smaller-scale domain patterns at the MPB are less obvious in this case and this may be attributed to the smaller lattice size limit imposed by the significantly higher computational costs of the 3D simulations. On the other hand, we observe that the MPB emerges with local and exchange energies even in the absence of long-range dipole-dipole interactions ($D_e = 0$) (Figure 4.11). This is consistent with the fact that the local critical dimension of a random-field Ising model is two. In a random-field Ising model with two states and positive exchange constant, the lattice is disordered in two dimensions (i.e., does not undergo the order-disorder transition) while the lattice can be ordered in three

dimensions under a small random field at sufficiently low temperature [94, 95]. We have also proven that this is true in our multistate setting. However, the domain patterns look more like those shown in the first row of Figure 4.6(b) than actual ferroelectric domains in the absence of long-range interactions. Our results are also consistent with the observation that dipolar interactions in an Ising model with two states leads to stripe domains in two dimensions [96].

Effect of external electric field

Finally, we consider the effect of an applied external electric field in Figure 4.12. Under [1 0] field that makes the tetragonal ($\mathcal{D}$) dipoles energetically more favorable, we still see that the tetragonal dipoles continue to be suppressed for small Ti (D) concentrations. However, tetragonal dipoles emerge gradually at a composition smaller than the MPB, increasing with composition until they become all tetragonal at a composition slightly larger than the MPB. So, there is a transition with composition, but transition is gradual and not sharp as in the case of the zero electric field. There is a corresponding behavior when an electric field is applied in the [1 1] direction. This shows that materials close to the MPB can undergo an electric-field-imposed rhombohedral/tetragonal transition close to the MPB but not at other compositions. This is consistent with experimental observations [97]. The corresponding microstructures are shown in Figure 4.13.

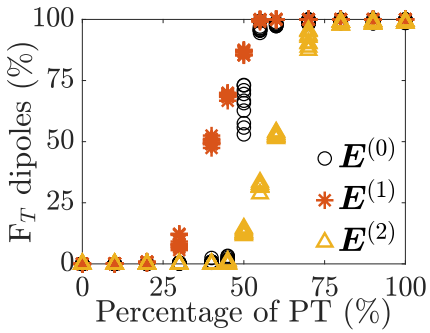

Figure 4.12: The effects of the external electric field ($\mathbf{E}^{(0)}$ = [0 0], $\mathbf{E}^{(1)}$ = [6 0], $\mathbf{E}^{(2)}$ = $[\frac{6}{\sqrt{2}}\ \frac{6}{\sqrt{2}}]$). There is superior ability to pole at the MPB.

4.5 Model for multiferroic materials

We now seek to apply the insights offered by the model to explore new phenomena. A number of perovskites are known to be ferromagnetic [98]. We explore the possibility of creating a multiferroic material (one that shows a strong coupling between electric and magnetic polarization) by exploiting the insight that the competition

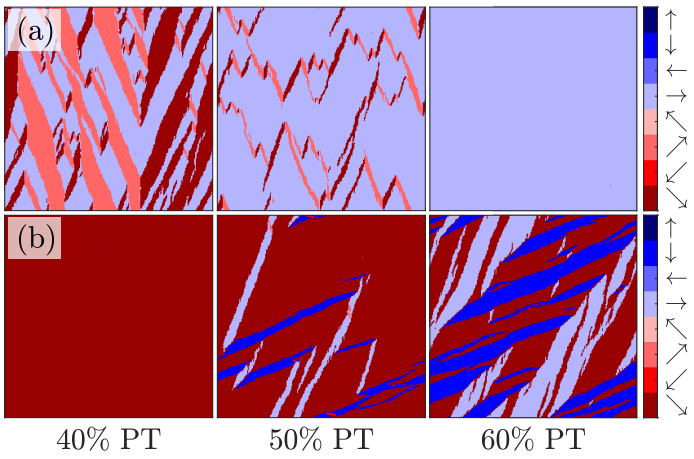

Figure 4.13: Domain patterns at various compositions under applied electric fields (a) $\mathbf{E}^{(1)} = [6\ 0]$ and (b) $\mathbf{E}^{(2)} = [\frac{6}{\sqrt{2}}\ \frac{6}{\sqrt{2}}]$.

between short-range disorder and long-range interaction can lead to unique ordering behavior. Such multiferroic coupling is limited in single materials [99], and is typically realized using composite media.

Consider a solid solution of two materials, C which prefers the $\mathcal{C}$ states that are ferroelectrically polarized in one crystallographic direction but with no ferromagnetism, and a material D that prefers the $\mathcal{D}$ states that are ferromagnetically polarized in a different crystallographic direction but with no ferroelectricity. The states are also mechanically distorted with the spontaneous strain corresponding to their ferroelectric/ferromagnetic directions. Since perovskites readily form solid solutions, and since perovskites can be both ferroelectric and ferromagnetic, it is natural to look for such systems in this class of materials.

As before, consider a d-dimensional periodic lattice ($d = 2$ or 3) with N lattice points where each lattice point has a fixed (quenched) chemical composition ($c_i \in \{0, 1\}$). The state s_i at the ith lattice point is characterized by an electrical dipole $\boldsymbol{p}_i$, magnetic dipole $\boldsymbol{m}_i$, and an elastic strain $\boldsymbol{e}_i$, and governed by the Hamiltonian

$$W(\{s_i\};\{c_i\}) = \sum_{i=1}^{N} h_i - \frac{J_e}{2}\sum_{<i,j>} \boldsymbol{p}_i \cdot \boldsymbol{p}_j - \frac{J_m}{2}\sum_{<i,j>} \boldsymbol{m}_i \cdot \boldsymbol{m}_j + W_e + W_m + W_s, \tag{4.15}$$

where

$$h_i = \begin{cases} 0 & c_i = 0\ \&\ s_i \in \mathcal{C},\ \text{or},\ c_i = 1\ \&\ s_i \in \mathcal{D} \\ h & \text{otherwise} \end{cases} \tag{4.16}$$

describes the local preference, W_e is the electrostatic interaction as in (4.4), W_m is the magnetostatic interaction under an applied magnetic field $\mathbf{H}$ ($W_m = W_{em}(\{\boldsymbol{m}_i\}, D_m, \mathbf{H})$), and W_s is the strain energy. The strain energy is scaled by the parameter D_s. The details regarding the strain energy term can be found in Section 4.6. We find the equilibrium states at low temperatures using an MCMC method with cooling as before.

4.6 Implementation for multiferroic materials

We implement the model in a similar manner as Section 4.3 except that we will also need to determine the expression of strain energy.

Strain energy

The strain energy W_s in (4.15) is taken to be the strain energy of a continuum region with transformation strain $\varepsilon^*(\mathbf{x})$ and uniform isotropic elastic modulus characterized by Lamé constants λ and μ. We set $\varepsilon^*(\mathbf{x}) = \begin{bmatrix} \varepsilon_1^*(\mathbf{x}) & \varepsilon_2^*(\mathbf{x}) \\ \varepsilon_2^*(\mathbf{x}) & -\varepsilon_1^*(\mathbf{x}) \end{bmatrix}$ and assume that $\varepsilon^*(\mathbf{x})$ is pixelated with $\varepsilon^* = \varepsilon_i$ in the pixel containing the ith lattice point. We will show

$$W_s = W_s^k + W_s^{self}, \tag{4.17}$$

where

$$W_s^k = \frac{D_s}{2V} \sum_{\mathbf{k}\neq\mathbf{0}} \left(B_{11}(\mathbf{k})|\widetilde{\varepsilon}_1^*(\mathbf{k})|^2 + B_{22}(\mathbf{k})|\widetilde{\varepsilon}_2^*(\mathbf{k})|^2 + 2B_{12}(\mathbf{k})\,\mathrm{Re}\left(\overline{\widetilde{\varepsilon}_1^*(\mathbf{k})}\widetilde{\varepsilon}_2^*(\mathbf{k})\right)\right),$$

$$W_s^{self} = \frac{D_s}{2V}\left(D_{11}\sum_{\alpha=1}^{N}|\varepsilon_1^{*\alpha}|^2 + D_{22}\sum_{\alpha=1}^{N}|\varepsilon_2^{*\alpha}|^2 + 2D_{12}\sum_{\alpha=1}^{N}\varepsilon_1^{*\alpha}\varepsilon_2^{*\alpha}\right),$$

$$D_s = \frac{2\mu}{1-\nu},$$

$$B_{11}(\mathbf{k}) = \frac{(k_1^2 - k_2^2)^2}{k^4}\exp(-k^2\sigma^2),$$

$$B_{12}(\mathbf{k}) = \frac{2k_1k_2(k_1^2 - k_2^2)}{k^4}\exp(-k^2\sigma^2),$$

$$B_{22}(\mathbf{k}) = \frac{4k_1^2k_2^2}{k^4}\exp(-k^2\sigma^2),$$

and $\widetilde{\varepsilon}^*(\mathbf{k})$ is the discrete Fourier transform of ε^*. The constants D_{11}, D_{22}, and D_{12} in the term are determined such that the total strain energy is zero for the homogeneous case.

To obtain these formulae, consider an infinite elastic body with a periodic volume V that undergoes a field of transformation strain $\varepsilon_{ij}^*(\mathbf{x})$. The transformation strain

field is also periodic with V, i.e. $\varepsilon^*_{ij}(\mathbf{x}) = \varepsilon^*_{ij}(\mathbf{x}+\mathbf{R})$ for any translation vector $\mathbf{R}$. Using Einstein notation, the elastic strain energy stored in the periodic volume V is given by

$$W_s = \frac{1}{2}\int_V C_{ijkl}\left(\varepsilon_{ij}(\mathbf{x}) - \varepsilon^*_{ij}(\mathbf{x})\right)\left(\varepsilon_{kl}(\mathbf{x}) - \varepsilon^*_{kl}(\mathbf{x})\right) d\mathbf{x}. \tag{4.18}$$

Next, we assume 2D plane strain, stress-free boundary condition in the infinity, and homogeneous isotropic linear elastic material, i.e. $C_{ijkl} = \lambda\delta_{ij}\delta_{kl} + \mu(\delta_{ik}\delta_{jl} + \delta_{il}\delta_{jk})$, where λ and μ are the Lamé constants. By solving the equilibrium equation $C_{ijkl}\frac{\partial}{\partial x_j}(\varepsilon_{kl}(\mathbf{x}) - \varepsilon^*_{kl}(\mathbf{x})) = 0$ in Fourier space and converting equation (4.18) into a similar form using Parseval's theorem, we conclude [100]

$$W_s = W_1 + W_2 + W_3, \tag{4.19}$$

$$W_1 = -\frac{1}{2\mu V}\sum_{\substack{\mathbf{k}\neq\mathbf{0}\\ \mathbf{k}\in\mathbb{K}^2}} \overline{\widetilde{M}_{ij}(\mathbf{k})}\widetilde{M}_{kl}(\mathbf{k})\left[\frac{k_j k_l}{k^2}\delta_{ik} - \frac{1}{2(1-\nu)}\frac{k_i k_j k_k k_l}{k^4}\right], \tag{4.20}$$

$$W_2 = \frac{1}{2}\int_V C_{ijkl}\varepsilon^*_{ij}(\mathbf{x})\varepsilon^*_{kl}(\mathbf{x})d\mathbf{x}, \tag{4.21}$$

$$W_3 = -\frac{V}{2}C_{ijkl}\langle\varepsilon^*_{ij}(\mathbf{x})\rangle\langle\varepsilon^*_{kl}(\mathbf{x})\rangle, \tag{4.22}$$

where $M_{ij}(\mathbf{x}) = C_{ijkl}\varepsilon^*_{kl}(\mathbf{x})$ and $\widetilde{M}$ refers to the Fourier transform of M.

For our problem, it suffices to write $\boldsymbol{\varepsilon}^*(\mathbf{x})$ as

$$\boldsymbol{\varepsilon}^*(\mathbf{x}) = \begin{bmatrix} \varepsilon^*_1(\mathbf{x}) & \varepsilon^*_2(\mathbf{x}) \\ \varepsilon^*_2(\mathbf{x}) & -\varepsilon^*_1(\mathbf{x}) \end{bmatrix}. \tag{4.23}$$

Then,

$$\widetilde{\mathbf{M}}^*(\mathbf{x}) = 2\mu\begin{bmatrix} \widetilde{\varepsilon}^*_1(\mathbf{k}) & \widetilde{\varepsilon}^*_2(\mathbf{k}) \\ \widetilde{\varepsilon}^*_2(\mathbf{k}) & -\widetilde{\varepsilon}^*_1(\mathbf{k}) \end{bmatrix} \tag{4.24}$$

and

$$\begin{aligned} W_1 = &-\frac{2\mu}{V}\sum_{\substack{\mathbf{k}\neq\mathbf{0}\\ \mathbf{k}\in\mathbb{K}^2}}\left[|\widetilde{\varepsilon}^*_1(\mathbf{k})|^2 + |\widetilde{\varepsilon}^*_2(\mathbf{k})|^2\right] \\ &+ \frac{\mu}{V(1-\nu)}\sum_{\substack{\mathbf{k}\neq\mathbf{0}\\ \mathbf{k}\in\mathbb{K}^2}}\left[\frac{(k_1^2-k_2^2)^2}{k^4}|\widetilde{\varepsilon}^*_1(\mathbf{k})|^2 + \frac{4k_1^2k_2^2}{k^4}|\widetilde{\varepsilon}^*_2(\mathbf{k})|^2\right. \\ &\left. + \frac{4k_1k_2(k_1^2-k_2^2)}{k^4}\,\mathrm{Re}\left(\overline{\widetilde{\varepsilon}^*_1(\mathbf{k})}\widetilde{\varepsilon}^*_2(\mathbf{k})\right)\right]. \end{aligned} \tag{4.25}$$

The first term above cancels out with $W_2 + W_3$ since

$$\begin{aligned} W_2 + W_3 &= 2\mu V \left[\left\langle (\varepsilon_1^*)^2 \right\rangle + \left\langle (\varepsilon_2^*)^2 \right\rangle\right] - 2\mu V \left[\langle \varepsilon_1^* \rangle^2 + \langle \varepsilon_2^* \rangle^2\right] \\ &= \frac{2\mu}{V} \sum_{\mathbf{k}} \left[|\widetilde{\varepsilon_1^*}|^2 + |\widetilde{\varepsilon_2^*}|^2\right] - 2\mu V \left[\langle \varepsilon_1^* \rangle + \langle \varepsilon_2^* \rangle\right] \\ &= \frac{2\mu}{V} \sum_{\mathbf{k}\neq\mathbf{0}} \left[|\widetilde{\varepsilon_1^*}|^2 + |\widetilde{\varepsilon_2^*}|^2\right]. \end{aligned}$$

Considering N point inclusions, the field of transformation strain in the periodic volume V is

$$\varepsilon^*(\mathbf{x}) = \sum_{\alpha=1}^{N} \varepsilon^{*\alpha} \delta(|\mathbf{x} - \mathbf{x}^\alpha|). \tag{4.26}$$

However, the Dirac delta function above introduces an issue when computing the self-energy. It also makes the sum in the Fourier space only conditionally convergent. Instead, we replace the delta function by a Gaussian function $g_\sigma(r)$. We then add a self-energy correction term W_s^{self}, similarly to the case of electrostatic energy or magnetostatic energy. The constants D_{11} and D_{22} in the term are determined such that the total strain energy is zero for the homogeneous case, that is when all the elastic dipoles are equal ($\varepsilon^{*1} = \varepsilon^{*2} = \cdots = \varepsilon^{*N}$).

With these, we obtain (4.17).

For easy computation of the change in energy due to the change in strain states, we introduce the corresponding generalized stress values.

$$\begin{aligned} \sigma_1^\alpha &= \frac{\partial (W_s^k - W_s^{k\_self})}{\partial \varepsilon_1^{*\alpha}} \\ &= \frac{2\mu}{V(1-\nu)} \sum_{\mathbf{k}\neq\mathbf{0}} \mathrm{Re}\left\{\left[B_{11}(\mathbf{k})\widetilde{\varepsilon_1^*}(\mathbf{k}) + B_{12}(\mathbf{k})\widetilde{\varepsilon_2^*}(\mathbf{k})\right] \exp(i\mathbf{k}\cdot\mathbf{x}^\alpha)\right\} \\ &\quad - \frac{2\mu}{V(1-\nu)}(C_{11}\varepsilon_1^{*\alpha} + C_{12}\varepsilon_2^{*\alpha}) \end{aligned}$$

$$\begin{aligned} \sigma_2^\alpha &= \frac{\partial (W_s^k - W_s^{k\_self})}{\partial \varepsilon_2^{*\alpha}} \\ &= \frac{2\mu}{V(1-\nu)} \sum_{\mathbf{k}\neq\mathbf{0}} \mathrm{Re}\left\{\left[B_{12}(\mathbf{k})\widetilde{\varepsilon_1^*}(\mathbf{k}) + B_{22}(\mathbf{k})\widetilde{\varepsilon_2^*}(\mathbf{k})\right] \exp(i\mathbf{k}\cdot\mathbf{x}^\alpha)\right\} \\ &\quad - \frac{2\mu}{V(1-\nu)}(C_{12}\varepsilon_1^{*\alpha} + C_{22}\varepsilon_2^{*\alpha}). \end{aligned}$$

The change in strain energy due to the change in the elastic dipole at lattice point α can then be approximated as

$$\Delta W_s \approx (\sigma_1^\alpha \Delta\varepsilon_1^{*\alpha} + \sigma_2^\alpha \Delta\varepsilon_2^{*\alpha}) + \Delta W_s^{k\_self} + \Delta W_s^{self}. \tag{4.27}$$

4.7 Results for multiferroic materials

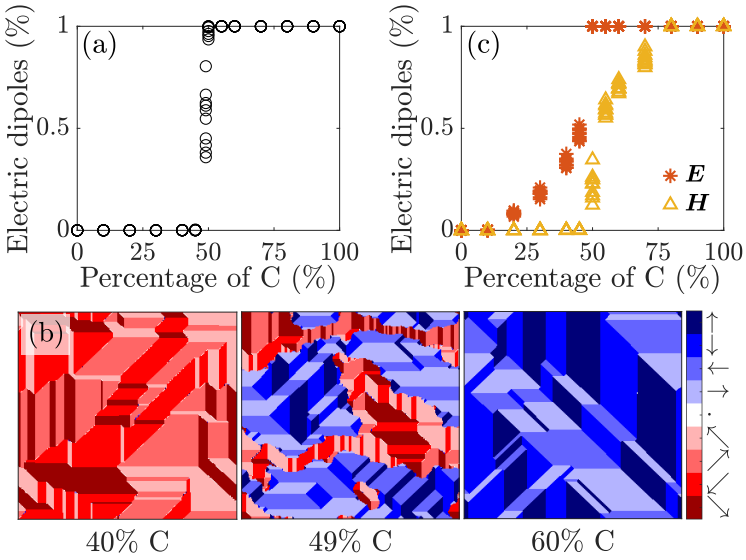

Figure 4.14: Morphotropic phase boundary as means of creating a multiferroic material. (a) The ordered phase in a random lattice of a ferroelectric and ferromagnetic material shows a MPB between a ferroelectric phase and a ferromagnetic phase. (b) Domain patterns at various compositions. (c) The effect of applied field ($\mathbf{E} = [2\ 0]$ or $\mathbf{H} = [\sqrt{2}\ \sqrt{2}]$) and a ferromagnetic/ferroelectric transformation.

We consider two dimensions and assume that each lattice point can take one of nine states: four ferroelectric $\mathcal{C}$ states with $s_1 = \{\boldsymbol{p}_1 = [1, 0], \boldsymbol{m}_1 = 0, \varepsilon_1 = [[1, 0], [0, -1]]\}$ and states s_2 through s_4 related to s_1 by symmetry; one zero state $s_5 = \{\boldsymbol{p}_5 = 0, \boldsymbol{m}_5 = 0, \varepsilon_5 = 0\}$; and four ferromagnetic $\mathcal{D}$ states with $s_6 = \left\{\boldsymbol{p}_6 = 0, \boldsymbol{m}_6 = 1/\sqrt{2}[1, -1], \varepsilon_6 = [[0, 1], [1, 0]]\right\}$ and states s_7 through s_9 related by symmetry. The different states are clearly listed in Table 4.1.

Figure 4.14 shows the results when $h = 2$, $J_e = J_m = D_e = D_m = D_s = 1$. Once again, we have an order-disorder phase transition, and we observe the emergence of a MPB in the form of a sharp transition at 49% from a ferromagnetic phase at low C compositions to a ferroelectric phase at high C compositions in the absence of any external fields. In particular, all ferroelectric $\mathcal{C}$ states are suppressed at low C compositions, and all ferromagnetic $\mathcal{D}$ are suppressed at high C compositions as shown in Figure 4.14(a). Further, the zero state is always suppressed except

State	$\boldsymbol{p}$	$\boldsymbol{m}$	$\boldsymbol{\varepsilon}$
s_1	$\begin{bmatrix}1\\0\end{bmatrix}$	$\begin{bmatrix}0\\0\end{bmatrix}$	$\begin{bmatrix}1 & 0\\0 & -1\end{bmatrix}$
s_2	$\begin{bmatrix}-1\\0\end{bmatrix}$	$\begin{bmatrix}0\\0\end{bmatrix}$	$\begin{bmatrix}1 & 0\\0 & -1\end{bmatrix}$
s_3	$\begin{bmatrix}0\\1\end{bmatrix}$	$\begin{bmatrix}0\\0\end{bmatrix}$	$\begin{bmatrix}-1 & 0\\0 & 1\end{bmatrix}$
s_4	$\begin{bmatrix}0\\-1\end{bmatrix}$	$\begin{bmatrix}0\\0\end{bmatrix}$	$\begin{bmatrix}-1 & 0\\0 & 1\end{bmatrix}$
s_5	$\begin{bmatrix}0\\0\end{bmatrix}$	$\begin{bmatrix}0\\0\end{bmatrix}$	$\begin{bmatrix}0 & 0\\0 & 0\end{bmatrix}$
s_6	$\begin{bmatrix}0\\0\end{bmatrix}$	$\frac{1}{\sqrt{2}}\begin{bmatrix}1\\1\end{bmatrix}$	$\begin{bmatrix}0 & 1\\1 & 0\end{bmatrix}$
s_7	$\begin{bmatrix}0\\0\end{bmatrix}$	$\frac{1}{\sqrt{2}}\begin{bmatrix}-1\\-1\end{bmatrix}$	$\begin{bmatrix}0 & 1\\1 & 0\end{bmatrix}$
s_8	$\begin{bmatrix}0\\0\end{bmatrix}$	$\frac{1}{\sqrt{2}}\begin{bmatrix}1\\-1\end{bmatrix}$	$\begin{bmatrix}0 & -1\\-1 & 0\end{bmatrix}$
s_9	$\begin{bmatrix}0\\0\end{bmatrix}$	$\frac{1}{\sqrt{2}}\begin{bmatrix}-1\\1\end{bmatrix}$	$\begin{bmatrix}0 & -1\\-1 & 0\end{bmatrix}$

Table 4.1: All possible dipole states (normalized)

at some domain walls. Thus, there are no multiferroic states, except at the MPB. Furthermore, as shown in Figure 4.14(b), we have classical domain walls at low and high compositions, but fragmented nonclassical domain walls at the MPB.

Figure 4.14(c) shows the effect of external electric and magnetic fields. The application of external magnetic field leads to a ferroelectric-to-ferromagnetic phase transition while the application of an external electric field leads to a ferromagnetic-to-ferroelectric phase transition at compositions close to the MPB. In other words, we have a strongly coupled multiferroic material close to the MPB. In fact, recent experiments have shown the capability of chemically engineering a related type of MPB called multiferroic MPB (which is the MPB between multiferroic phases) [101, 102]. Multiferroic characteristics are also found to be enhanced at the MPB of bismuth ferrite-based systems [103].

In Figure 4.15, we also explore the effects of the different energy contributions in the model. Removing the strain energy (i.e. setting $D_s = 0$) does little effect in the case

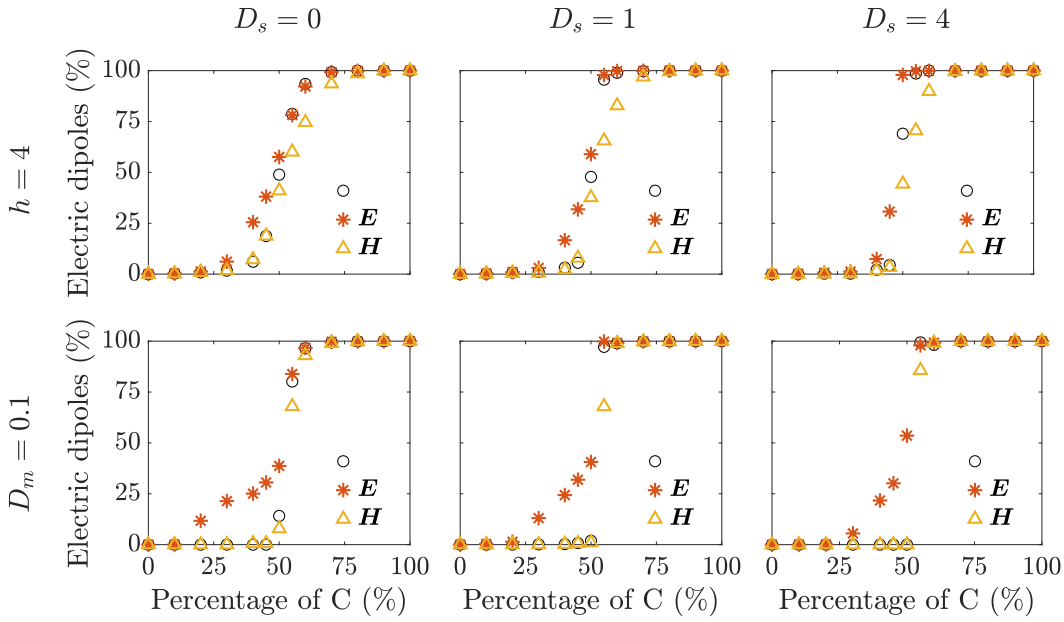

Figure 4.15: The effect of local (h), magnetic (D_m), and elastic (D_s) contributions on ferromagnetic/ferroelectric transformation with and without applied field ($\mathbf{E}$ = [2 0] or $\boldsymbol{H}$ = [$\sqrt{2}$ $\sqrt{2}$]).

of the parameters used in Figure 4.14. However with a stronger local field (e.g., by increasing h from 2 to 4), we find that a stronger elastic field helps to further suppress compositional disorder, leading to a sharper MPB that occurs over a narrower range of composition. This in turn results in a stronger response to external fields at the MPB and hence a more strongly coupled multiferroic system. The figure also shows the effect of reducing the magnetic contribution (D_m) relative to the electric contribution. We observe that the magneto-electric coupling becomes asymmetric with the material being more sensitive to the applied electric field compared to the applied magnetic field.

All of these show that the origin of the ME coupling at the MPB is a ferroelectric-ferromagnetic phase transition. The material is ferromagnetic at low concentrations and ferroelectric at high concentrations with an exchange of stability at the MPB. The application of an electric or magnetic field changes the balance leading to the magnetoelectric coupling. Strain coupling is not necessary but can magnify the coupling.

4.8 Conclusion

In this work, we have proposed a model based on the random field Ising model with long-range interactions motivated by perovskite solid solutions. We have used the model to study the morphotropic phase boundary, and the model provides qualitative answers to the critical open questions raised in the introduction. Specifically, the results show that both the long-range dipole-dipole interaction as well as the short-range chemical disorder are necessary for an MPB. The long-range dipole-dipole interaction overwhelms and suppresses the chemical disorder leading to a well-defined phase (crystal structure) at all compositions except the MPB. This is the reason we see distinct crystal structures away from the MPB. At the MPB, there is a change of stability from one phase to another. This balance in the other energies enables the chemical disorder to reveal itself at the MPB. This in turn leads to a frustrated and fragmented domain pattern as the disorder leads to a local preference of one structure over the other. In particular, no stable and well-defined phase emerges from this disorder. Further, the disorder also leads to a number of metastable states at the MPB and these aid in domain switching and the ability to pole the material. In contrast, away from the MPB, the stable structure suppresses domain switching and the ability to pole the material.

The parameters of the model also provide various trends that can be used to tune material behavior. The paraelectric-to-ferroelectric phase transition temperature is controlled by the short-range exchange energy that manifests the balance between the short-range repulsions of electron clouds and the short-range portion of the Coulomb interaction with a range of the lattice constant. Since the exchange energy depends on the average concentration, so does the transition temperature. The composition of the MPB on the other hand is controlled by the relative stability of the two phases and the relative magnitude of the polarization of the two phases.

Finally, the insights gained from the model suggest a new multiferroic material where the magnetoelastic coupling is a result of an MPB-enabled phase transition from a ferroelectric state to a ferromagnetic state.

In short, the model is able to describe a whole range of complex phenomenology and provide qualitative answers to the questions raised in the introduction. In order to make these quantitative, it would be necessary to link the model quantitatively to first principles calculations through multi-scale modeling. This remains a task for the future. Further, we have largely studied the model through numerical simulations and mean-field arguments. It would be useful to conduct more detailed theoretical

studies of the model. Finally, it would be exciting to search for new multiferroic materials based on the insights here. All of these remain open issues for the future.

Chapter 5

MACHINE-LEARNED PREDICTION OF THE ELECTRONIC FIELDS IN A CRYSTAL

The work presented in this chapter has been adapted from the following publication:

> Y. S. Teh, S. Ghosh, K. Bhattacharya. Machine-learned prediction of the electronic fields in a crystal. *In submission*. 2021.

5.1 Introduction

A number of studies over the recent years have shown that the electronic structure of crystalline solids depends sensitively on the deformation, and therefore straining a lattice from its equilibrium structure can lead to new properties. For example, the perovskite $SrTiO_3$ which is usually paraelectric becomes ferroelectric when subjected to a lattice strain [104]. Silicon becomes electrically polarized under strain, and the role of strain on various functional materials has been extensively studied [105]. In metals, strain can lead to deformation twinning [106]. Strain-induced martensitic phase transitions are widely observed and exploited in shape-memory alloys and steels [107–109]. Finally, strain engineering is emerging as an important tool in 2D materials [110].

Density functional theory (DFT) [111] is a powerful tool to understand the electronic structure of matter, and thus has been instrumental to the understanding, design, and optimization of materials. Examples include the predictions of energy materials [112], the geometric design of polar metals [113], and the screening for high-performance piezoelectrics [114]. Strain-induced phenomena can also be studied using DFT but it requires the repeated electronic structure calculation of a crystalline lattice unit cell subject to various strains. Consequently, a systematic exploration of the strain space can be computationally expensive. In this work, we study if a neural network approximation can assist in this exploration. We are motivated by the success of machine learning, particularly deep neural networks in image recognition [115, 116] and natural language processing tasks [117, 118]. There is also a growing literature on the use of these methods in materials science [119].

Another motivation for our work comes from the study of defects in crystalline solids that play a critical role in determining mechanical and other properties of various solids: for example, vacancies are critical for creep and dislocations for plasticity. The perturbations caused by these defects decay very slowly, and therefore their direct study requires very large computational domains. Solving the DFT equations is prohibitive on such large computational domains, and a variety of approaches have been proposed (e.g., quantum mechanics/molecular mechanics [120–124] and embedded DFT [125]). Fago *et al.* [25] introduced a "local" DFT-based quasicontinuum method where the deformation of the atoms is assumed to follow a piece-wise affine deformation, and the energy density of each region is computed using a unit cell DFT calculation. A new approach was introduced by Suryanarayana *et al.* [26] that solves the DFT equations by introducing a numerical basis that exploits the decay. Specifically, the electronic fields are taken to be a sum of a piece-wise periodic 'predictor' and a slowly decaying 'corrector.' The approach leads to accurate solutions over millions of atoms. It can resolve the core, the far field, as well as the interactions between far-field stress and core of defects including dislocations [27, 126]. The implementation of these approaches also requires the repeated solution of the unit cell subject to distortion.

Here, we study a deep neural network approximation for the energy and the underlying electronic fields in a unit cell of magnesium subjected to strain. We generate data by repeatedly solving the unit cell problem and use it to train a deep neural network. An important challenge is the representation of the electronic fields: these are elements of infinite dimensional function spaces whereas neural networks typically approximate maps between finite dimensional spaces. Therefore, we use the approach that combines model reduction and neural networks for high-fidelity approximations of maps between function spaces [127]. We show excellent, specifically chemical, accuracy of the trained neural network approximation over a range of strain. In fact, the approximation is able to learn the onset of an instability.

Some recent works have focused on approximating electronic structure quantities, mainly electronic density, using machine learning as a means to bypassing DFT calculations. Chandrasekaran *et al.* [128] used a representation that encodes the atomic arrangement around any grid point and mapped it to electron charge density and local density of states (LDOS) spectrum at the corresponding grid point. This grid point method allows the quantities at each grid point to be evaluated independently and hence in parallelization. It can also be highly dependent on the

discretization used and quickly become intractable as the system size grows. Grisafi and co-workers [129] expanded the electronic charge densities of different hydrocarbons as sums of atom-centered basis functions and machine-learned them using symmetry-adapted Gaussian process regression. The use of such localized basis set allows for transferability across different molecular systems, but is not applicable to metals. A work by Brockherde *et al.* [130] explores the mappings from potential to ground-state density represented in Fourier basis. One interesting finding was that learning energy indirectly – from potential to electron density followed by electron density to energy – yields better predictions than the direct map from potential to energy. It is noteworthy that all these methods use the atomic environment typically within some cutoff radius as the input of the learning maps, and this requires careful selection of descriptors. Our work focuses on crystals or solids and uses strain as its input. Its simplicity allows for highly accurate predictions of electronic fields along with the combination of data-based model reduction and neural networks. It also offers a convenient way to relate to constitutive response of materials at the larger continuum level.

The remainder of the chapter is organized as follows. Section 5.2 provides some background information on density functional theory and in particular the electronic fields that will be used for machine learning. Section 5.3 discusses the machine learning approach, which is subsequently applied to magnesium – a promising light weight structural material – as an example in Section 5.4. Finally, Section 5.5 concludes our findings.

5.2 Background

Density functional theory

Given atomic positions $\{\mathbf{R}_I\}$, density functional theory seeks to find the total electronic free energy system $\mathcal{F}(\{\mathbf{R}_I\})$, the electronic charge density $\rho(\mathbf{x})$, and other electronic functions of interest. To do so, we solve the Kohn-Sham equation for energy states E_i and orbitals $\psi_i(\mathbf{x})$ (ignoring spins for simplicity of presentation and assuming a non-local pseudo-potential in the Kleinman-Bylander form),

$$\mathcal{H}\psi_i = E_i\psi_i, \quad \mathcal{H} = -\frac{1}{2}\nabla^2 + V_{\text{ps}}^{\text{nl}} + V_{\text{xc}} + V_{\text{H}} + V_{\text{ext}} \tag{5.1}$$

where $V_{\text{ps}}^{\text{nl}}(\mathbf{x}, \mathbf{x}'; \{\mathbf{R}_I\})$ is the non-local portion of the psuedopotential and depends on the atomic positions $\{\mathbf{R}_I\}$, and V_{xc}, V_{H}, V_{ext} are the exchange-correlation, Hartree,

and external potential due to ions given by

$$V_{\text{xc}} = \frac{\partial e_{\text{xc}}}{\partial \rho}, \quad -\frac{1}{4\pi}\nabla^2 V_{\text{H}} = \rho, \quad -\frac{1}{4\pi}\nabla^2 V_{\text{ext}} = b, \tag{5.2}$$

with valence electron density ρ, charge density $b = b(\mathbf{x}; \{\mathbf{R}_I\})$ describing the local part of the pseudopotential, and exchange-correlation density $e_{xc}(\rho)$. It is convenient to write the Hamiltonian $\mathcal{H}$ in operator form, and introduce the corresponding (one-point) density operator whose diagonal component gives the electron density

$$\mathcal{H} = \sum_i E_i \psi_i(\mathbf{x})\psi_i(\mathbf{x}'), \tag{5.3}$$

$$\gamma(\mathbf{x}, \mathbf{x}') = \sum_i f(E_i)\psi_i(\mathbf{x})\psi_i(\mathbf{x}'), \quad \rho(\mathbf{x}) = \gamma(\mathbf{x}, \mathbf{x}), \tag{5.4}$$

where f describes the occupancy and satisfies $\sum_i f(E_i) = n$ with n being the total number of electrons in the system. The total electronic free energy of the system may be written as

$$\mathcal{F}(\{\mathbf{R}_I\}) = \text{Tr}\,(\mathcal{H}\gamma) + \int \left(e_{\text{xc}} - V_{\text{xc}}\rho - \frac{1}{2}V_{\text{H}}\rho + \frac{1}{2}V_{\text{ext}}b\right) d\mathbf{x} - \text{Tr}(S(\gamma))/\beta, \tag{5.5}$$

where $\beta = 1/(k_B T)$, T is the fictitious electronic temperature, and S is the generalized entropy that determines the occupancy f. We label the first term of (5.5) the band structure energy ($U = \text{Tr}(\mathcal{H}\gamma)$) and note that its density is

$$u(\mathbf{x}) = \sum_i E_i f(E_i)|\psi_i(\mathbf{x})|^2. \tag{5.6}$$

If we view $\mathcal{F}$ as a functional on γ, then the Kohn-Sham equation (5.1) and an equation for f are the Euler-Lagrange equation associated with the variational problem. Note that the Kohn-Sham equation is non-linear because the exchange-correlation and the Hartree potential depend on the electron density, so it is usually solved by a fixed point iteration approach (also known as the self-consistent field approach).

We specifically consider the entropy associated with the Marzari cold smearing with broadening [131]

$$\frac{1}{\beta}f'(E) = \frac{2}{\sqrt{\pi}}\left(\kappa t^3 - t^2 - \frac{3}{2}\kappa t + \frac{3}{2}\right)e^{-t^2}, \quad t = \beta(E - E_f). \tag{5.7}$$

$\kappa = -0.5634$ and E_f is the Fermi energy or the Lagrange multiplier that enforces the constraint $\sum_i f(E_i) = n$[1]. The volumetric entropy (i.e. entropy per unit volume)

[1] We have also repeated our work with the entropy of mixing $S(f) = -f\log\frac{f}{2} + (2-\frac{f}{2})\log(1-\frac{f}{2})$ that gives $\frac{f}{2}$ to be the Fermi-Dirac function.

is

$$s(\mathbf{x}) = -\frac{1}{\sqrt{\pi}} \sum_i |\psi_i(\mathbf{x})|^2 e^{-t^2} (\kappa t^3 + t^2 - \frac{1}{2}). \tag{5.8}$$

Putting all these together, we view density functional theory as a map,

$$\Phi_{\text{DFT}} : \{\mathbf{R}_I\} \to \{\rho(\mathbf{x}), \phi(\mathbf{x}), u(\mathbf{x}), s(\mathbf{x}), \mathcal{F}\}, \tag{5.9}$$

where $\phi = V_{\text{H}} + V_{\text{ext}}$ is the Coulomb potential.

Crystals

A crystal is a periodic arrangement of N atoms described by a unit cell $\mathcal{U}$ bounded by three lattice vectors $\{\mathbf{a}, \mathbf{b}, \mathbf{c}\}$ and N atomic positions or basis vectors $\mathbf{R}_I$, $I = 1, \ldots, N$. It is customary to introduce fractional coordinates $\bar{\mathbf{R}}_I$ with respect to the lattice vectors.

Using the Bloch theorem, the electronic orbitals may be written as $\psi_{i,\mathbf{k}} = \exp(i\mathbf{k} \cdot \mathbf{x})\Psi_{i,\mathbf{k}}(\mathbf{x})$ where $\Psi_{i,\mathbf{k}}$ is periodic and $\mathbf{k}$ is a vector in the Brillouin zone associated with $\mathcal{U}$. The formulas above can be naturally extended (see Appendix E.1) and we obtain $\rho(\mathbf{x})$, $\phi(\mathbf{x})$, $u(\mathbf{x})$, $s(\mathbf{x})$, to be periodic functions while the free energy $\mathcal{F}$ is now interpreted as energy per unit cell.

We are interested in the deformations of the crystal, so we choose a reference crystal structure with lattice vectors $\{\mathbf{a}^0, \mathbf{b}^0, \mathbf{c}^0\}$ and atomic coordinates $\{\bar{\mathbf{R}}_I^0\}$. We can then describe the deformation (up to rotations) in terms of

$$D = \{\lambda_a, \lambda_b, \lambda_c, \theta_a, \theta_b, \theta_c\} \quad \text{where} \quad \lambda_a = \frac{|\mathbf{a}|}{|\mathbf{a}^0|}, \ \theta_a = \arcsin\left(\frac{\mathbf{b} \times \mathbf{c}}{|\mathbf{b}||\mathbf{c}|}\right), \ \text{etc.} \tag{5.10}$$

Now, given any deformed crystal and any set of atomic coordinates, we can find the electronic states by solving the electronic states as described above. Further, we can find the equilibrium states of the atoms $\{\bar{\mathbf{R}}_I^e\}$ by solving $\frac{\partial \mathcal{F}}{\partial \bar{\mathbf{R}}_I} = 0, I = 1, \ldots N - 1$.

Finally, the electronic quantities are functions defined on the deformed unit cell or a domain that depends on the strain. It is convenient to define them on a fixed domain, so we map them back to the reference lattice with a change of variables $\bar{\rho}(\mathbf{F}^{-1}\mathbf{x}) = \rho(\mathbf{x})$,$\bar{\phi}(F^{-1}x) = \phi(x)$, etc., where $\mathbf{F}$ is a tensor that maps the reference unit cell to the deformed unit cell $\mathbf{a} = \mathbf{F}\mathbf{a}^0, \mathbf{b} = \mathbf{F}\mathbf{b}^0, \mathbf{c} = \mathbf{F}\mathbf{c}^0$.

In summary, the deformation behavior of a crystal is described by the map

$$\Phi : D \to \{\{\bar{\mathbf{R}}_I^e\}, \bar{\rho}(\mathbf{x}), \bar{\phi}(\mathbf{x}), \bar{u}(\mathbf{x}), \bar{s}(\mathbf{x}), \mathcal{F}\}, \tag{5.11}$$

where the electronic states are computed for the deformed crystal with the atoms in their equilibrium positions.

Implementation

The density functional theory calculations to evaluate the map Φ are conducted using the software ABINIT [132]. We use a plane-wave basis set with a kinetic energy cut-off of 24 Ha (Hartree), a Troullier-Martins norm-conserving pseudopotential with local channel $l = 1$, and local density approximation (LDA) in the Perdew-Wang 92 functional form as the exchange-correlation energy. Cold smearing of magnitude 0.01 Ha is used [131] and the Brillouin zone integration is performed using a $12\times12\times12$ k-point sampling. Furthermore, the atomic positions are relaxed using the Broyden-Fletcher-Goldfarb-Shanno minimization.

5.3 Approach

We seek to learn an approximation for the map Φ for a given material. We first generate data by evaluating the map using DFT and seek to use this data to learn an approximation. However, note that the quantities ρ, ϕ, u, s are functions and thus elements of infinite-dimensional linear spaces. In practice, these are evaluated on a finite-dimensional discretization, but still we want our approximation to be independent of the particular discretization. Therefore we use an approach by Bhattacharya *et al.* [127] that combines model reduction with a deep neural net to learn the map Φ. The idea is to use model reduction to find a finite dimensional representation for each function and then use a deep neural net to learn the map. Specifically, we find maps $p_\rho : \bar{\rho} \to \{\rho_\alpha\}_{\alpha=1}^{d_\rho}$, $p_\phi : \bar{\phi} \to \{\phi_\alpha\}_{\alpha=1}^{d_\phi}$, etc. that reduce (project) the infinite-dimensional spaces to a d_ρ-dimensional space, and maps $\ell_\rho : \{\rho_\alpha\}_{\alpha=1}^{d_\rho} \to \bar{\rho}$, $\ell_\phi : \{\phi_\alpha\}_{\alpha=1}^{d_\phi} \to \bar{\phi}$, etc. that lift (reconstruct) the d_ρ-dimensional space to the infinite dimensional space. We then find an approximate map

$$\Phi_{\text{ml}} : D \to \{\{\bar{\mathbf{R}}_I^e\}, \{\rho_\alpha\}, \{\phi_\alpha\}, \{u_\alpha\}, \{s_\alpha\}, \mathcal{F}\} \tag{5.12}$$

such that $\Phi \approx \ell \circ \Phi_{\text{ml}}$. In this work, we use principal component approximation (PCA) for model reduction p, ℓ and a deep neural net for Φ_{ml}.

5.4 Demonstration on Magnesium

Magnesium

Magnesium is a hexagonal close-packed (HCP) material. It is the lightest of all structural materials, and of significant interest as a light-weight structural material

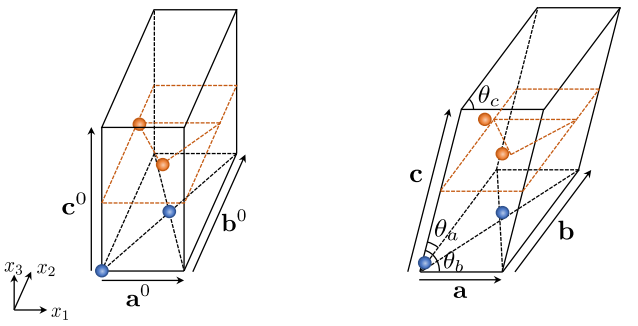

Figure 5.1: A 4-atom magnesium unit cell in both undeformed and deformed configurations.

for bio-medical, automotive, and protective applications [133–135]. We consider the four-atom unit cell shown in Figure 5.1 where $\mathbf{a}^0$, $\mathbf{b}^0$, and $\mathbf{c}^0$ directions are the $[10\bar{1}0]$, $[0, \bar{1}, 1, 0]$, and $[0001]$ directions, respectively, in the HCP crystallographic notation. The atoms in the reference unit cell are located at fractional coordinates $\{0, 0, 0\}$, $\{1/2, 1/2, 0\}$, $\{0, 2/3, 1/2\}$, and $\{1/2, 1/6, 1/2\}$ in the reference configuration. The $\mathbf{a}^0$-$\mathbf{b}^0$ plane perpendicular to the $\mathbf{c}^0$-axis or (0001) plane is the basal plane. We have observed in our calculations that the basal planes deform uniformly, but slide relative to each other. After eliminating free translation of the unit cell, the fractional coordinates in the deformed configuration can be taken as $\{\bar{R}^e_1, \bar{R}^e_2, \bar{R}^e_3\}$, $\{1/2 + \bar{R}^e_1, 1/2 + \bar{R}^e_2, \bar{R}^e_3\}$, $\{-\bar{R}^e_1, 2/3 - \bar{R}^e_2, 1/2 - \bar{R}^e_3\}$, $\{1/2 - \bar{R}^e_1, 1/6 - \bar{R}^e_2, 1/2 - \bar{R}^e_3\}$.

Architecture and training

We use PCA dimensions of $d_\rho = d_\phi = d_u = d_s = 50$ and the following neural network architecture: (1) a two-layer dense network with hidden layer widths of 500 and the hyperbolic tangent activation function for each of Φ^ρ_{ml},Φ^ϕ_{ml},Φ^u_{ml} and Φ^s_{ml}; (2) a three-layer dense network with hidden layer widths of 50, 100, 50, respectively, and the same type of activation function for Φ^R_{ml} and $\Phi^{\mathcal{F}}_{\text{ml}}$. These hyperparameters are selected based on four-fold cross-validation results.

We generate a total of 3000 data, with each input sample D drawn independently from a normal distribution truncated to two standard deviations satisfying $\lambda_a, \lambda_b, \lambda_c \in [0.9, 1.1]$ and $\theta_a, \theta_b, \theta_c \in [84°, 96°]$. Such a distribution reflects the fact that smaller deformations are more likely to be encountered in real materials. Out of all the data generated, 2000 of them are reserved for training and validation, while the rest are used for testing.

Using the training data, we first identify the map p via PCA. This is followed by standardizing both the input and output of Φ_{ml} to zero mean and unit variance, before we train the neural network parameters using the Adam optimization algorithm at a training rate of 0.001, a small l2 regularization of 0.0001 on the weights, and a batch size of 128 for a total of 4000 epochs. Subsequently, given any deformation in the testing data, we generate predictions by applying the map $\ell \circ \Phi_{\text{ml}}$ and compare them with the true values.

Computational costs

There are two elements to the computational cost. The first is the online cost of evaluation. This takes fractions of a second (0.002 second) on an Intel Skylake (2.1 GHz) core compared to 30 minutes on 14 cores for a full DFT evaluation. Thus, learned approximations provide significant savings. The second is the one-time offline cost of generating the data and training. As noted, each data set takes 30 minutes on 14 cores Intel Skylake (2.1 GHz) and we generate 2000 data sets for training. This is comparable to a single evaluation in a MacroDFT calculation. However, since each data set is independent, it is is trivially parallelizable. The cost of training is about 5 minutes on a single core.

Results: Electronic fields and energy

A typical result is shown in Figure 5.2. We observe that our approach is able to capture the main features of the electronic fields, with very small errors. Figure 5.3 compares the predicted and actual energies (band structure energy, entropic energy, and total free energy). The mean errors are 0.15 mHa, 0.014 mHa, and 0.10 mHa while the maximum errors are 2.4 mHa, 0.13 mHa, and 1.5 mHa for Figure 5.3 (a), (b), and (c), respectively. Importantly, since there are four atoms in this unit cell, all the errors are significantly smaller than 1.6 mHa/atom (or 1 kcal/mol) which is widely accepted as the accuracy required for chemical accuracy [136].

We now turn to understanding the training and the actual distribution of errors. We introduce a normalized root-mean-square error (NRMSE), defined as root-mean-square error divided by the range of the data (evaluated on a discretized grid of size N_d for field quantities)

$$\text{NRMSE} = \frac{\sqrt{\frac{1}{N_d}\sum_{j=1}^{N_d}(y_j^{pred} - y_j^{true})^2}}{y_{max}^{true} - y_{min}^{true}}. \tag{5.13}$$

Figure 5.4 shows how the normalized root-mean-square error (evaluated on a $N_d =$

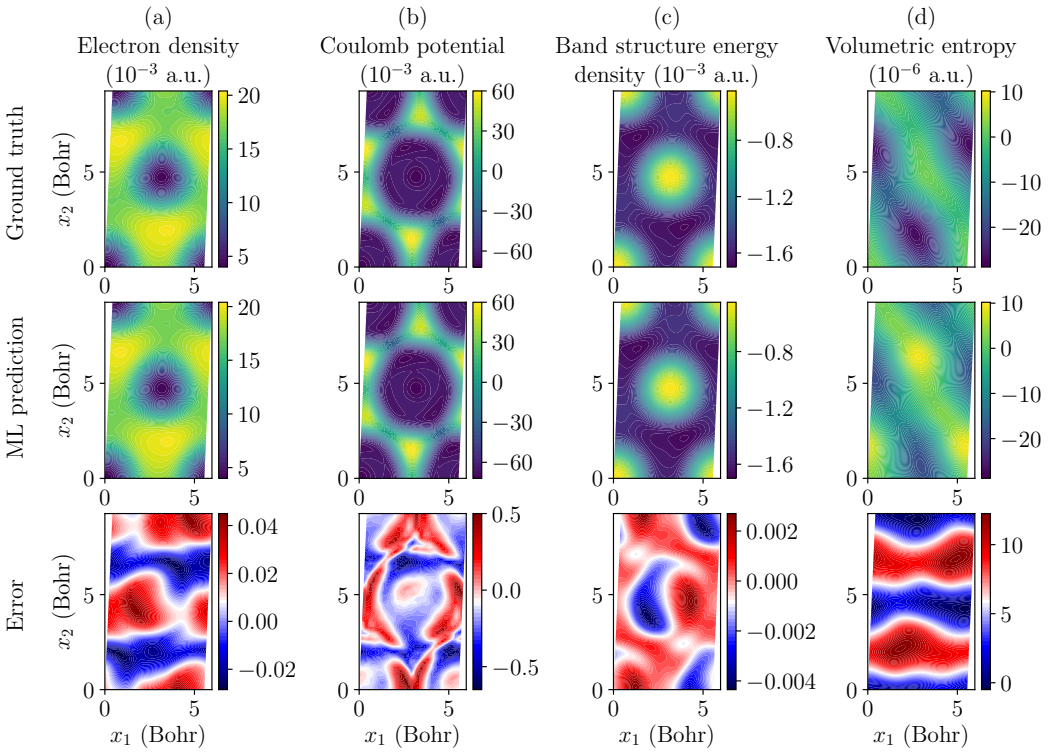

Figure 5.2: Typical results. (a) Electron density, (b) Coulomb potential, (c) band structure energy density, and (d) volumetric entropy in atomic unit (a.u.) along the $x_3 = 0$ plane for $\lambda_a = 0.9696, \lambda_b = 0.9237, \lambda_c = 0.9906, \theta_a = 92.1598°, \theta_b = 85.6196°, \theta_c = 87.3824°$. Notice that the scale used to display the error is significantly smaller than the scale used to display the quantities except for entropy, which is small.

$36 \times 64 \times 60$ grid for field quantities) averaged over the 1000 test samples decreases with an increasing number of training samples. We see that the error has stabilized at 2000 training samples for this set of test samples. The figure also shows the error due to PCA, i.e., the error associated with the model reduction from an infinite dimensional function space to a finite dimensional representation of the electronic fields. We see that the overall error is about ten times the PCA error. Figure 5.5 shows how the NRMSE changes with volumetric strain for these 1000 test samples. We notice that the error in electron density, Coulomb potential, and band structure energy density is extremely small (~0.1%) in almost all cases with a maximum error of ~8% in isolated cases. Indeed, the five points with the largest error in all these plots all correspond to the same five test data points and are associated with very large distortions in the unit cell that were poorly represented in the normal distribution used to sample the training data. The error is larger in volumetric entropy averaging

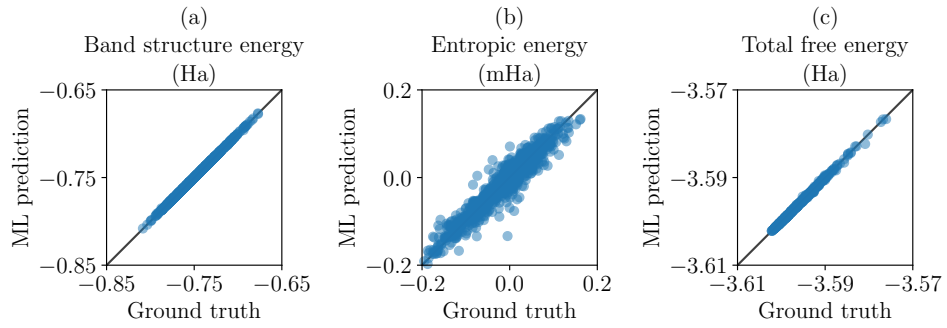

Figure 5.3: Comparisons between predicted and true values for (a) band structure energy ($U = \int u(x)dx$), (b) entropic energy ($-S/\beta = -\int s(x)dx/\beta$), and (c) total free energy ($\mathcal{F}$). Predictions are perfectly accurate if all the data points lie on the black solid line of $y = x$. The mean errors are 0.15 mHa, 0.014 mHa, and 0.10 mHa while the maximum errors are 2.4 mHa, 0.13 mHa, and 1.5 mHa for (a), (b) and (c), respectively.

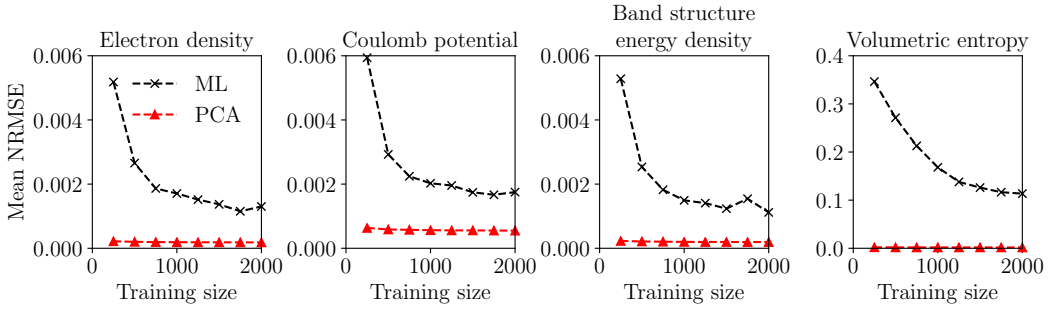

Figure 5.4: Training error. Variation of test error (NRMSE, equation (5.13)) marked as ML with training size for the four scalar field quantities. The NRMSE shown in the plot is averaged over all 1000 test samples. The figure also shows the PCA error.

∼11% mainly because this is a very small number. Finally, the error displacement of the basis atoms is 0.0035 Bohr which is much smaller than the maximum and average atomic displacements of 0.66 Bohr and 0.097 Bohr, respectively. Again, the five points with the largest error here correspond to the same data points with large error in Figure 5.5.

An intended goal of this work is the use of the electronic fields as pre-conditioners or predictor fields in larger multiscale calculations. To evaluate their efficacy in doing so, we calculate the total free energy in four ways. First, in the *direct* approach, we learn the map from the deformation to the total energy ($\Phi^{\mathcal{F}}_{\text{ml}}$). In the second *sum* approach, we evaluate the total energy using equation (5.5) from the learned electron

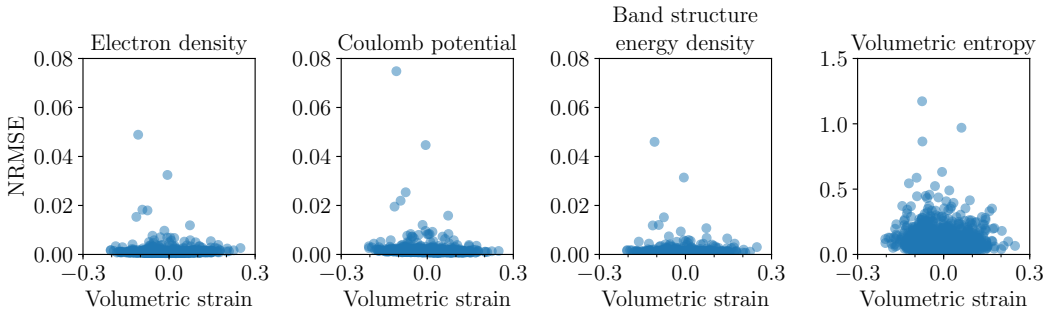

Figure 5.5: Distributions of normalized root-mean-square errors (NRMSE) between predicted and true values evaluated on a $36 \times 64 \times 60$ grid across 1000 test samples.

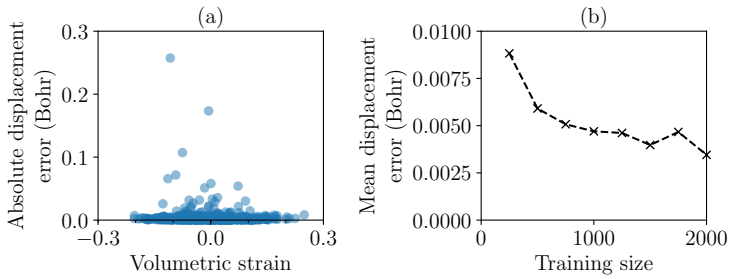

Figure 5.6: Test errors for reduced coordinates of magnesium atoms in terms of absolute displacement errors. (a) shows the distribution of errors for 1000 test samples. (b) shows how the mean error varies with training size.

density, band structure energy and entropy fields, and atomic coordinates. Third, in the *orbital* approach, we use the learned electron density and atomic coordinates to construct the Hamiltonian, find the electronic orbitals, and then use the combination of the learned electron density and atomic coordinates with the computed orbitals (to compute the kinetic energy). Note that in the third approach, we do not use the band structure energy, but effectively recompute it by computing the orbitals. So, the difference between the direct and orbital energies is a measure of the inconsistency between the learned band structure energy and the learned energy density. Finally, in the *SCF* approach, we perform one SCF iteration starting from the learned electron density and atomic coordinates before computing the energy. Note that we do not directly use the learned electron density, but recompute it using a SCF iteration. So, the difference between orbital and SCF values indicates whether the learned electron density is close to convergence, or to use this electron density as a precursor.

Figure 5.7 shows how closely the free energy predicted from the four approaches match to their true values. The sum approach leads to a very low average error of

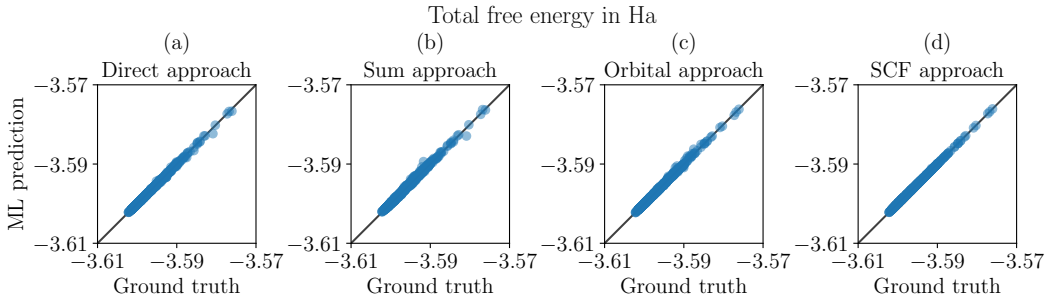

Figure 5.7: Comparisons between predicted and true total free energy values for a 4-atom magnesium unit cell where the prediction is made using four separate ML approaches: (a) direct (same as Figure 5.3(c)), (b) sum, (c) orbital, and (d) SCF. The average absolute error changes from 0.10 mHa, 0.16 mHa, 0.087 mHa, to 0.0015 mHa, going from cases (a) to (d). Similarly, the maximum absolute error changes from 1.5 mHa, 2.3 mHa, 1.2 mHa, to 0.37 mHa.

0.15 mHa across all 1000 test data with the maximum error standing at 2.4 mHa. These errors are consistent with those of the band structure energy in Figure 5.3, emphasizing the contribution of this band structure energy to the total energy. The orbital and SCF approaches lead to further reductions, and they even outperform the direct approach. All of these signify that our proposed approach not only learns the energy but also the fields extremely accurately, and thus can be used as predictors in larger calculations.

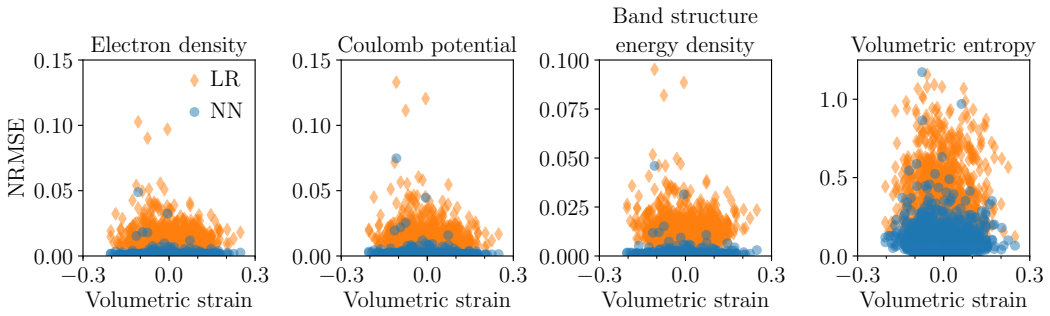

Figure 5.8: Comparison of prediction errors when a linear regression (LR) is used in place of a neural network (NN) for each map Φ_{ml}. The NN results are reproduced from Figure 5.5.

Finally, we compare our approximation with linear regression in Figure 5.8. It shows that the error due to linear regression (LR) is significantly higher than that due to our nonlinear approximation using neural networks (NN), thus demonstrating the efficacy of our architecture (NN).

Results: Stresses and instability

In order to further assess the accuracy of the learned electronic fields and energy, and to understand its efficacy in practice, we study the derivative quantities (i.e. stresses), in the crystal subjected to deformation. According to the Cauchy-Born rule [137], the macroscopic deformation gradient in any macroscopic deformation is equal to the matrix $\mathbf{F}$ that maps the reference lattice to the current lattice. The corresponding nonlinear strain measure $\mathbf{E} = 1/2(\mathbf{F}^T\mathbf{F} - \mathbf{I})$ where $\mathbf{I}$ is the identity. The Cauchy or true stress in the material is given by

$$\boldsymbol{\sigma} = \frac{1}{V}\mathbf{F}\frac{\partial \mathcal{F}}{\partial \mathbf{E}}\mathbf{F}^T, \tag{5.14}$$

where V is the volume of the deformed unit cell and $\mathcal{F}$ is the free energy of the unit cell. It is common [138, 139] to approximate this using a small distortion approximation

$$\boldsymbol{\sigma} = \frac{1}{V(\boldsymbol{\varepsilon})}\frac{\partial \mathcal{F}}{\partial \boldsymbol{\varepsilon}} \quad \text{or} \quad \sigma_{ij} = \frac{1}{V(\boldsymbol{\varepsilon})}\frac{\partial \mathcal{F}}{\partial \varepsilon_{ij}}, \tag{5.15}$$

where $\boldsymbol{\varepsilon} = 1/2(\mathbf{F} + \mathbf{F}^T - \mathbf{I}) \approx \mathbf{E}$ is the linear strain measure. We use this expression in our work, though the results can easily be adapted to the nonlinear counterpart. The linear strain is related to the variables we use to describe the lattice $(\lambda_a, \lambda_b, \lambda_c, \theta_a, \theta_b, \theta_c)$ through the relation

$$\begin{aligned}
\lambda_a^2 &= (1+\varepsilon_{11})^2 + \varepsilon_{12}^2 + \varepsilon_{13}^2, \\
\lambda_b^2 &= \varepsilon_{12}^2 + (1+\varepsilon_{22})^2 + \varepsilon_{23}^2, \\
\lambda_c^2 &= \varepsilon_{13}^2 + \varepsilon_{23}^2 + (1+\varepsilon_{33})^2,
\end{aligned} \tag{5.16}$$

$$\frac{\pi}{2} - \theta_a = 2\varepsilon_{23}, \quad \frac{\pi}{2} - \theta_b = 2\varepsilon_{13}, \quad \frac{\pi}{2} - \theta_c = 2\varepsilon_{12}, \tag{5.17}$$

and we may obtain $\partial\mathcal{F}/\partial\varepsilon_{ij}$ using the chain rule (see Appendix E.2 for details).

We focus specifically on the state of uniaxial stress where σ_{ii} (for i =1, 2 or 3) is non-zero, but all the other components are zero. We therefore prescribe ε_{ii}, and solve (5.15) to obtain the other components of strain. The solution to this equation is equivalent to minimizing the energy, and we use gradient descent with the step size chosen according to the Barzilai-Borwein method [140].

The results are shown in Figure 5.9 for the stress in the x_1, x_2, and x_3 directions as well as the corresponding transverse strains[2]. Figure 5.9(a) compares the ground

[2] The use of cold smearing in our DFT calculations requires a pre-stress or residual stress to stabilize the HCP configuration. We have subtracted the uniaxial residual stress in (a) and the corresponding residual strains in the other two transverse directions in (b–d) of this figure.

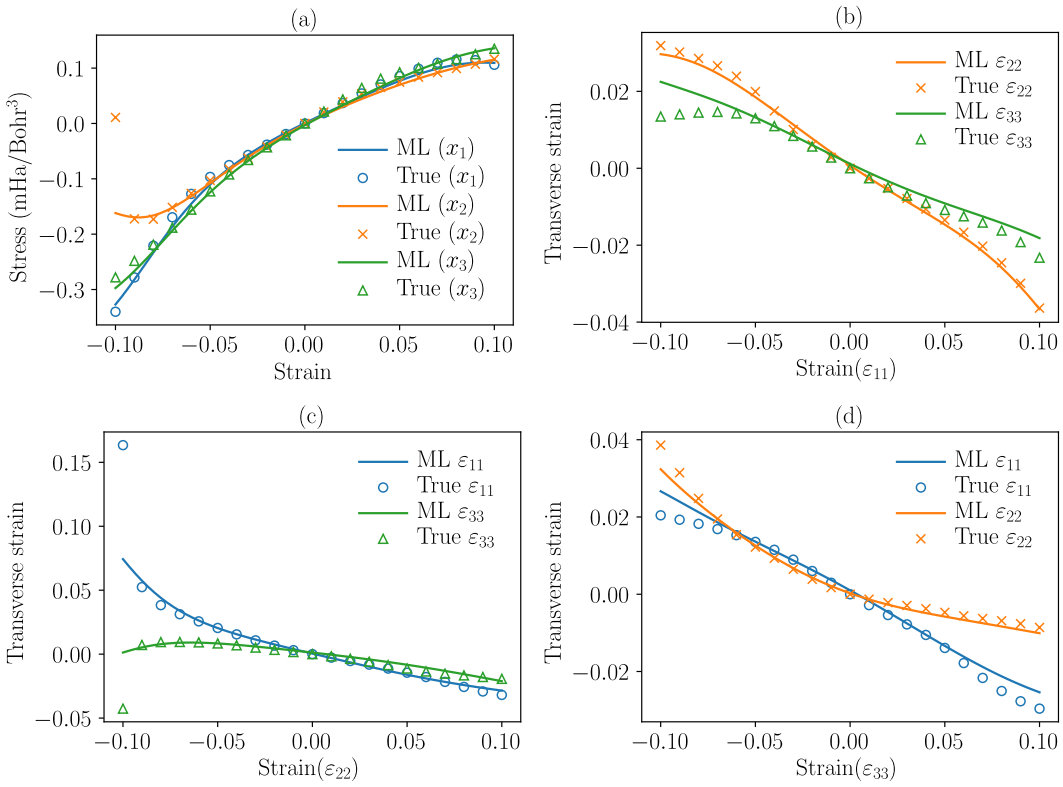

Figure 5.9: Uniaxial test results. The results obtained from our machine learning model are marked as 'ML', while the results obtained directly from DFT calculations with stress relaxation are marked as 'true.' (a) Stress-strain curves for uniaxial stress in the x_1, x_2, and x_3 directions. (b–d) Corresponding transverse strain.

truth stress to that of the ML approach, where the free energy is computed using the direct approach described earlier[3]. We see that the ML approach predicts the stress extremely well except for high compression in the x_2 direction where there is an instability. Still, the approach captures the onset of this instability. Figures 5.9(b–d) show the corresponding transverse strains. We see that this is not linear in any case. Further, there is a dramatic expansion in the x_1 direction (**a**-axis) as we reach the instability during severe compression in the x_2 direction.

Figure 5.10(a) shows the corresponding electronic fields and positions of the internal atoms. Specifically, given the value of ε_{22}, we find the other components of strain and the corresponding deformation variables. We then interrogate our learned map to find the electronic fields and atomic positions. The figure also compares the learned and ground truth atomic positions, and we see good agreement except at the instability. We observe that in most cases, the atoms in the unit cell lie very near

[3]In Appendix F, we also present the uniaxial stress results obtained using the sum approach.

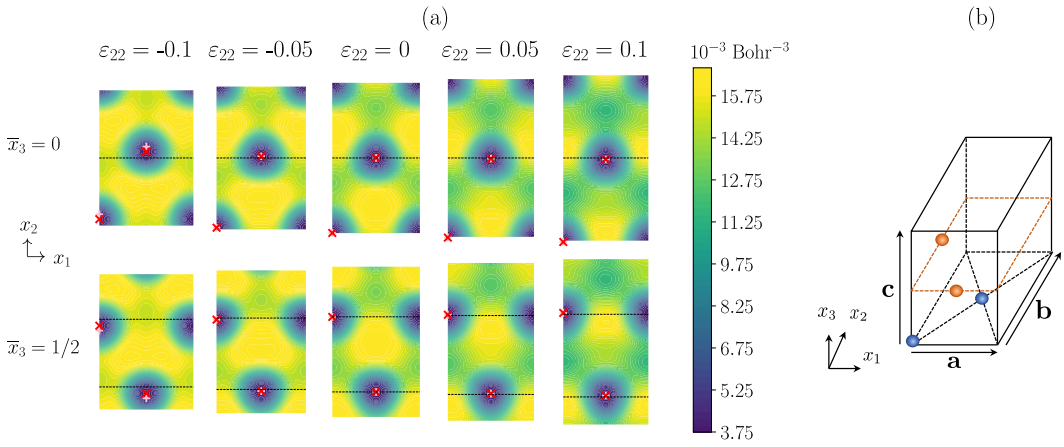

Figure 5.10: Uniaxial test results in the x_2 direction obtained from our machine learning models. (a) Snapshots of a magnesium unit cell undergoing uniaxial test. The color gradient shows the electron density distribution, while the red crosses (×) mark the atomic positions. The dashed lines on the plots correspond to $\bar{x}_2 = 1/2$ on the basal plane $\bar{x}_3 = 0$, as well as $\bar{x}_2 = 1/6$ and $\bar{x}_2 = 2/3$ on the basal plane $\bar{x}_3 = 1/2$. The actual atomic positions obtained from DFT calculations are shown as pink plusses (+) for reference. (b) An illustration of the deformed face-centered cubic (FCC) structure exhibited by the unit cell under uniaxial compression with $\varepsilon_{22} = -0.1$.

to the dashed lines, thus exhibiting a stretched HCP structure. However the atomic positions change very abruptly under high compression in the x_2 direction. The learned atomic positions capture this abrupt change to some extent.

Together, Figures 5.9 and 5.10 show that as the crystal is compressed in the x_2 direction and reaches its instability, it elongates dramatically along the x_1 direction. Consequently, the lengths of **a**, **b**, and **c** edges become similar. This is accompanied by the relative sliding of the basal planes (see Figure 5.10(a) where the atoms in the $\bar{x}_3 = 0$ plane move in the positive x_2 direction whereas the atoms in the $\bar{x}_3 = 1/2$ basal plane move in the negative x_2 direction), bringing the atoms on the middle basal plane to the face centers of the 4-atom unit cell. Thus, the structure approaches that of a face-centered cubic (FCC) lattice as shown in Figure 5.10(b). In other words, we see a HCP to FCC phase transition. This has been observed under high hydrostatic confinement [141], but is generally overshadowed by the $(10\bar{1}2)$ tension twin mode at lower confinements[4].

[4]Magnesium has a soft "tension" twinning mode with a $(10\bar{1}2)$ twin plane and a $[\bar{1}011]$ shear direction [106]. This twin causes a compression along the $[10\bar{1}0]$ or x_2 direction. The observed instability is associated with this soft twinning mode.

5.5 Conclusion

In this chapter, we have presented a machine learning approximation for the change in the electronic structure as a crystal is deformed. We have demonstrated the approach on magnesium and shown that the machine-learned predictions reach the level of chemical accuracy. In particular, we not only learn energy values accurately, but also predict electronic fields with minimal error. These show that the models can indeed be sufficiently accurate to be useful as predictors or pre-conditioners for large-scale DFT methods. Finally, we have computed derivative quantities such as stresses under specific loading conditions from the learning models and found that they match very well with the ground truth DFT results. The model can even capture the onset of strain-induced phase transformation. All these further indicate another future direction of extending the learning model to one that can extract DFT-informed constitutive relations that can be easily incorporated in continuum level calculations.

Chapter 6

SUMMARY AND CONCLUSIONS

Imperfections and instabilities are inevitable in crystals, but can lead to unique and useful material properties if they are properly understood and exploited. This thesis presents the development of three computational models at appropriate length scales to study these aspects of crystalline solids.

Chapter 3 details a device model that sheds light on the key mechanisms of the photovoltaic (PV) effect observed in multi-domain perovskite oxides and in particular the role of domain walls. Importantly the model takes into account the complex interactions among ferroelectric polarization, space charges, photo-generation, and electronic transport. It predicts a significant electric potential step across both 71° and 109° domain walls, which in turn contributes to the PV effect. This result is found to be generic for non-180° domain walls, which experience a change in the polarization component normal to the domain wall. There is also a strong correlation between polarization and oxygen octahedra tilts, indicating the nontrivial role of the latter in the PV effect. The domain wall-based PV effect is further shown to be additive in nature, allowing for the possibility of generating above-bandgap voltage.

In the next study on the morphotropic phase boundary (MPB) of perovskite solid solutions in Chapter 4, we propose a lattice model based on the random field Ising model with long-range interactions. With the efficient mathematical formulation and implementation of the long-range interactions, we successfully simulate a sufficiently large lattice size. This allows us to capture the local chemical disorder and randomness at the lattice level and understand its competition with long-range interactions. The model shows that the MPB arises as an instability in the form of a frustrated state in a narrow composition range while the disorder is suppressed elsewhere. Both randomness in compositions and long-range interactions are found to be crucial for the emergence of this phenomenon. The model also enables us to demonstrate the possiblity of creating new materials with strong magnetoelectric coupling by exploiting MPBs.

The final work presented in this thesis focuses on more predictive models based on first principles calculations such as density functional theory (DFT), rather than

models constructed at the continuum or lattice level of the former two. In particular, we explore how machine learning techniques can assist in such calculations. Chapter 5 discusses the machine learning framework we have developed to approximate electronic fields in crystalline solids subjected to deformation using data from DFT calculations. We demonstrate the approach on magnesium and show that we can predict the energy and electronic fields to the level of chemical accuracy and even capture lattice instabilities. This DFT-based machine learning approach can be very valuable in tuning material properties using strain engineering and the multi-resolution studies of defects in crystalline solids, which in both cases require repeated DFT calculations of a unit cell subjected to different strains.

6.1 Future opportunities and outlook

This thesis presents both physics-based and data-driven computational models to study various aspects of crystalline materials. However there still exist areas for continued development.

The device model developed in Chapter 3 has currently been implemented numerically in the one-dimensional setting. It is briefly mentioned at the end of the chapter that a two- or three-dimensional numerical implementation would be very useful for future device designs. Indeed such implementation will allow us to more quantitatively investigate how the domain-wall-driven photovoltaic response in perovskite oxides can be affected by numerous factors including the different substrates on which the perovskite film is grown on, the formation of depletion layers around the different conducting electrodes, as well as the amounts of oxygen vacancies and other dopants. We can also incorporate other details to make the model more comprehensive and predictive. One element is the higher conductivity at the domain walls compared to the bulk domains [142]; the current model simply assumes uniform electrical conductivity. Another consideration is to integrate the bulk photovoltaic effect (BPVE) into the model. It has been suggested that the domain-wall-driven photovoltaic response observed in [28] is partially canceled out by the BPVE [143]. We can consider a way to include the BPVE in a consistent manner through the bulk photovoltaic response tensor that can be obtained from first principles calculations [143]. If so, then we will be able to systematically compare the contributions from the BPVE and the domain wall effect. Subsequently we can modify the device design accordingly to allow cooperative existence of both effects, hence further enhancing the overall photovoltaic performance. All these additional considerations can render the device model more robust and useful for future device

design.

With regards to the lattice model in Chapter 4, it would be useful to perform a more thorough theoretical analysis of the model since we have mainly only studied it using numerical simulations and mean field approach. It will also be helpful to check if the proposed multiferroic system can be realized experimentally, as well as if our model can be adapted to describe relaxor ferroelectrics, which are ferroelectric materials with high electrostriction and are currently a subject of active research. Moreover we mention at the end of the chapter about extending the model and linking it to first principles calculations like DFT. Such extension can be similar to the first-principles-based effective Hamiltonian construction in [80], but it needs to also exhibit the important feature of compositional disorder and randomness in solid solutions analogous to our model that uses a sufficiently large lattice size. Even though this extension can be very challenging, the resulting model will prove to be very valuable in materials design of perovskite solid solutions. In particular, the model can assist experimentalists in tuning the different material properties including piezoelectric, dielectric, ferroelectric, magnetic, and photovoltaic properties by modifying chemical compositions. Currently such process has been done manually in experiments [37, 103, 144] and can be very tedious, but it can be greatly sped up by taking advantage of computational resources.

As for the final work on machine learning approximation of electronic fields, we have so far demonstrated its possible efficacy in larger DFT-based multiscale calculations. The next step is to integrate these learning models into the multiscale implementations, thus allowing these methods to be much more computationally viable for the study of crystal defects that often involves the coupling of the quantum mechanics of local defect core with long-range fields at the continuum level. For instance, instead of solving unit cell DFT problems for different deformations in order to obtain the 'predictor' component of the electronic fields in the macroDFT method [27], we can replace it with our learnt models of electron density, Coulomb potential, band structure energy density, and volumetric entropy. Similarly the unit cell DFT calculations embedded at each quadrature point of the DFT-based local quasicontinuum method can be replaced with our learning model that maps deformation to total electronic energy and its derivatives as stresses. Furthermore we can use the same framework to explore different crystalline material systems and different deformation ranges. In general, we do not expect the machine learning models to be able to extrapolate results out of the deformation range of the train-

ing set since the electronic fields can vary remarkably at large deformations. In the case of macroDFT, the 'corrector' component is meant to compensate for the inaccurate results of the 'predictor' component at limited grid points, and therefore extrapolation is not a concern here. In other cases where highly accurate predictions are vital, one may elect to revert back to full unit cell DFT calculations whenever encountering very large deformations. One may also enlarge the deformation range of the training set, but that may require more training data. Finally, we find that the architecture that combines principle component analysis and neural networks yields the best predictions for magnesium. Nonetheless continual explorations of other machine learning representations or techniques can be very helpful and may potentially lead to better approximations and even more applications.

As a note, the first two studies on the domain-wall-driven photovoltaic effect and the morphotrophic phase boundary of perovskite solid solutions essentially involve perturbing perovskites at the unit cell lattice level. Therefore, a similar machine learning framework as in the final work can be constructed and applied to perovskite crystals to enable these studies at the DFT level. In this case, we may also need to consider polarization or electric dipole moment of each unit cell as an additional component of the learning framework.

Ultimately the computational models we have developed in this thesis improve our understanding of different aspects of crystalline materials. It is possible to turn them into more quantitative models with the incorporation of first principles calculations and machine learning approximations that enable the simulation of larger and more realistic systems. All these enhancements will further contribute to the prediction, design, and manufacturing of useful materials.

BIBLIOGRAPHY

[5] W. Zhang and K. Bhattacharya. A computational model of ferroelectric domains. Part II: grain boundaries and defect pinning. *Acta Materialia*, 53(1): 199–209, 2005. doi: 10.1016/j.actamat.2004.09.015. URL https://www.sciencedirect.com/science/article/pii/S1359645404005579.

[6] S. Choudhury, Y.L. Li, C. Krill, and L.Q. Chen. Effect of grain orientation and grain size on ferroelectric domain switching and evolution: Phase field simulations. *Acta Materialia*, 55(4):1415–1426, 2007. doi: 10.1016/j.actamat.2006.09.048. URL https://www.sciencedirect.com/science/article/pii/S1359645406007294.

[7] A. Vidyasagar, W. L. Tan, and D. M. Kochmann. Predicting the effective response of bulk polycrystalline ferroelectric ceramics via improved spectral phase field methods. *Journal of the Mechanics and Physics of Solids*, 106: 133–151, 2017. doi: 10.1016/j.jmps.2017.05.017. URL https://www.sciencedirect.com/science/article/pii/S0022509617300595.

[8] X. Q. Ke, D. Wang, and Y. Wang. Origin of ultrahigh piezoelectric activity of [001]-oriented ferroelectric single crystals at the morphotropic phase boundary. *Applied Physics Letters*, 108(1):012904, 2016. doi: 10.1063/1.4939626. URL https://doi.org/10.1063/1.4939626.

[9] F. Li, S. Zhang, T. Yang, Z. Xu, N. Zhang, G. Liu, J. Wang, J. Wang, Z. Cheng, Z. G. Ye, J. Luo, T. R. Shrout, and L. Q. Chen. The origin of ultrahigh piezoelectricity in relaxor-ferroelectric solid solution crystals. *Nature Communications*, 7:1–9, 2016. doi: 10.1038/ncomms13807. URL http://dx.doi.org/10.1038/ncomms13807.

[10] F. Li, D. Lin, Z. Chen, Z. Cheng, J. Wang, C. Li, Z. Xu, Q. Huang, X. Liao, L. Q. Chen, T. R. Shrout, and S. Zhang. Ultrahigh piezoelectricity in ferroelectric ceramics by design. *Nature Materials*, 17(4):349–354, 2018. doi: 10.1038/s41563-018-0034-4. URL http://dx.doi.org/10.1038/s41563-018-0034-4.

[11] J.-J. Wang, Y. Wang, J. F. Ihlefeld, P. E. Hopkins, and L.-Q. Chen. Tunable thermal conductivity via domain structure engineering in ferroelectric thin films: A phase-field simulation. *Acta Materialia*, 111:220–231, 2016. doi: 10.1016/j.actamat.2016.03.069. URL https://www.sciencedirect.com/science/article/pii/S1359645416302361.

[12] Y. Xiao and K. Bhattacharya. A Continuum Theory of Deformable, Semiconducting Ferroelectrics. *Archive for Rational Mechanics and Analysis*, 189:59–95, 2008. doi: 10.1007/s00205-

007-0096-y. URL https://link.springer.com/content/pdf/10.1007{%}2Fs00205-007-0096-y.pdf.

[13] N. F. Mott. The mechanical properties of metals. *Proceedings of the Physical Society. Section B*, 64(9):729–741, 1951. doi: 10.1088/0370-1301/64/9/301. URL https://doi.org/10.1088/0370-1301/64/9/301.

[14] Y. Yang and I. Baker. The influence of vacancy concentration on the mechanical behavior of fe-40al. *Intermetallics*, 6(3):167–175, 1998. doi: 10.1016/S0966-9795(97)00062-9. URL https://www.sciencedirect.com/science/article/pii/S0966979597000629.

[15] J. L. Jordan and S. C. Deevi. Vacancy formation and effects in feal. *Intermetallics*, 11(6):507–528, 2003. doi: 10.1016/S0966-9795(03)00027-X. URL https://www.sciencedirect.com/science/article/pii/S096697950300027X.

[16] J. P. Hirth. The influence of grain boundaries on mechanical properties. *Metallurgical Transactions*, 3:3047–3067, 1972. doi: 10.1007/BF02661312. URL https://link.springer.com/content/pdf/10.1007{%}2FBF02661312.pdf.

[17] X. Li and K. Lu. Playing with defects in metals. *Nature Materials*, 16 (7):700–701, 2017. doi: 10.1038/nmat4929. URL https://doi.org/10.1038/nmat4929.

[1] D. I. Woodward, J. Knudsen, and I. M. Reaney. Review of crystal and domain structures in the $PbZr_xTi_{1-x}O_3$ solid solution. *Physical Review B*, 72:104110, 2005. doi: 10.1103/PhysRevB.72.104110. URL https://link.aps.org/doi/10.1103/PhysRevB.72.104110.

[2] J.-J. Wang, B. Wang, and L.-Q. Chen. Understanding, predicting, and designing ferroelectric domain structures and switching guided by the phase-field method. *Annual Review of Materials Research*, 49(1):127–152, 2019. doi: 10.1146/annurev-matsci-070218-121843. URL https://doi.org/10.1146/annurev-matsci-070218-121843.

[3] N. Y. Jin and A. T. Winter. Dislocation structures in cyclically deformed [001] copper crystals. *Acta Metallurgica*, 32(8):1173–1176, 1984. doi: 10.1016/0001-6160(84)90123-8. URL https://www.sciencedirect.com/science/article/pii/0001616084901238.

[18] P. Ghosez, X. Gonze, and J.-P. Michenaud. Lattice dynamics and ferroelectric instability of barium titanate. *Ferroelectrics*, 194(1):39–54, 1997. doi: 10.1080/00150199708016081. URL https://doi.org/10.1080/00150199708016081.

[19] G. H. Jaffari and A. M. Iqbal. Interplay between ferroelectric and quantum paraelectric instabilities in eu0.7ba0.3tio3 perovskite oxide: Defect dipoles and ferroelectric instability induced by oxygen vacancies. *Journal of Applied Physics*, 128(1):014104, 2020. doi: 10.1063/5.0005611. URL https://doi.org/10.1063/5.0005611.

[20] J. H. Haeni, P. Irvin, W. Chang, R. Uecker, P. Reiche, Y. L. Li, S. Choudhury, W. Tian, M. E. Hawley, B. Craigo, A. K. Tagantsev, X. Q. Pan, S. K. Streiffer, L. Q. Chen, S. W. Kirchoefer, J. Levy, and D. G. Schlom. Room-temperature ferroelectricity in strained SrTiO3. *Nature*, 430(7001):758–761, 2004. doi: 10.1038/nature02773. URL http://doi.org/10.1038/nature02773.

[21] G. Grimvall, B. Magyari-Köpe, V. Ozoliņš, and K. A. Persson. Lattice instabilities in metallic elements. *Reviews of Modern Physics*, 84:945–986, Jun 2012. doi: 10.1103/RevModPhys.84.945. URL https://link.aps.org/doi/10.1103/RevModPhys.84.945.

[22] W. Kohn. Nobel lecture: Electronic structure of matter—wave functions and density functionals. *Reviews of Modern Physics*, 71:1253–1266, 1999. doi: 10.1103/RevModPhys.71.1253. URL https://link.aps.org/doi/10.1103/RevModPhys.71.1253.

[23] B. J. Alder and T. E. Wainwright. Studies in molecular dynamics. i. general method. *The Journal of Chemical Physics*, 31(2):459–466, 1959. doi: 10.1063/1.1730376. URL https://doi.org/10.1063/1.1730376.

[24] J. S. Langer. *Models of pattern formation in first-order phase transitions*, pages 165–186. World Scientific, 1986. doi: 10.1142/9789814415309_0005. URL https://www.worldscientific.com/doi/abs/10.1142/9789814415309_0005.

[25] M. Fago, R. L. Hayes, E. A. Carter, and M. Ortiz. Density-functional-theory-based local quasicontinuum method: Prediction of dislocation nucleation. *Physical Review B*, 70:100102, 2004. doi: 10.1103/PhysRevB.70.100102. URL https://link.aps.org/doi/10.1103/PhysRevB.70.100102.

[26] P. Suryanarayana, K. Bhattacharya, and M. Ortiz. Coarse-graining kohn–sham density functional theory. *Journal of the Mechanics and Physics of Solids*, 61(1):38–60, 2013. doi: https://doi.org/10.1016/j.jmps.2012.09.002. URL https://www.sciencedirect.com/science/article/pii/S0022509612001949.

[27] M. Ponga, K. Bhattacharya, and M. Ortiz. A sublinear-scaling approach to density-functional-theory analysis of crystal defects. *Journal of the Mechanics and Physics of Solids*, 95:530–556, 2016. doi: 10.1016/j.jmps.2016.05.029. URL https://www.sciencedirect.com/science/article/pii/S0022509616303489.

[28] S. Y. Yang, J Seidel, S J Byrnes, P Shafer, C-h Yang, M D Rossell, P Yu, Y-h Chu, J F Scott, J W Ager, L W Martin, and R Ramesh. Above-bandgap voltages from ferroelectric photovoltaic devices. *Nature Nanotechnology*, 5(2):143–147, 2010. doi: 10.1038/nnano.2009.451. URL https://www.nature.com/nnano/journal/v5/n2/pdf/nnano.2009.451.pdfhttp://www.nature.com/doifinder/10.1038/nnano.2009.451{%}5Cnhttp://dx.doi.org/10.1038/nnano.2009.451{%}5Cnhttp://www.nature.com/nnano/journal/v5/n2/suppinfo/nnano.2009.451{_}S1.html.

[29] B. Noheda, D. E. Cox, G. Shirane, J. A. Gonzalo, L. E. Cross, and S.-E. Park. A monoclinic ferroelectric phase in the $Pb[Zr_{1-x}Ti_x]O_3$ solid solution. *Applied Physics Letters*, 74, 1999. doi: 10.1063/1.123756. URL https://doi.org/10.1063/1.123756.

[30] D. E. Cox, B. Noheda, and G. Shirane. Low-temperature phases in $PbZr_{0.52}Ti_{0.48}O_3$: A neutron powder diffraction study. *Physical Review B*, 71:134110, 2005. doi: 10.1103/PhysRevB.71.134110. URL https://link.aps.org/doi/10.1103/PhysRevB.71.134110.

[31] N. Zhang, H. Yokota, A. M. Glazer, D. A. Keen, S. Gorfman, P. A. Thomas, W. Ren, and Z.-G. Ye. Local-scale structures across the morphotropic phase boundary in $PbZr_xTi_{1-x}O_3$. *International Union of Crystallography Journal*, 5(1):73–81, 2018. doi: 10.1107/S2052252517016633. URL https://doi.org/10.1107/S2052252517016633.

[32] R. Ragini, R. Ranjan, S. K. Mishra, and D. Pandey. Room temperature structure of $Pb(Zr_xTi_{1-x})O_3$ around the morphotropic phase boundary region: A Rietveld study. *Journal of Applied Physics*, 92(6):3266–3274, 2002. doi: 10.1063/1.1483921. URL https://doi.org/10.1063/1.1483921.

[33] S. Gorfman, D. S. Keeble, A. M. Glazer, X. Long, Y. Xie, Z.-G. Ye, S. Collins, and P. A. Thomas. High-resolution x-ray diffraction study of single crystals of lead zirconate titanate. *Physical Review B*, 84:020102, 2011. doi: 10.1103/PhysRevB.84.020102. URL https://link.aps.org/doi/10.1103/PhysRevB.84.020102.

[34] K. Uchino. *Ferroelectric devices*. CRC Press, 2009.

[35] R. J. D. Tilley. *Perovskites: Structure-Property Relationships*. John Wiley & Sons, Ltd, 2016.

[36] N. Setter. *Piezoelectric Materials in Devices: Extended Reviews on Current and Emerging Piezoelectric Materials, Technology, and Applications*. N. Setter, 2002. ISBN 9782970034605. URL https://books.google.com/books?id=sBGCQgAACAAJ.

[37] J. Vieten, Br. Bulfin, P. Huck, M. Horton, D. Guban, L. Zhu, Y. Lu, K. A. Persson, M. Roeb, and C. Sattler. Materials design of perovskite solid solutions for thermochemical applications. *Energy & Environmental Science*, 12:1369–1384, 2019. doi: 10.1039/C9EE00085B. URL http://dx.doi.org/10.1039/C9EE00085B.

[38] Y. Marinova, J. M. Hohemberger, E. Cordoncillo, P. Escribano, and J. B. Carda. Study of solid solutions, with perovskite structure, for application in the field of the ceramic pigments. *Journal of the European Ceramic Society*, 23(2):213–220, 2003. doi: 10.1016/S0955-2219(02)00182-6. URL https://www.sciencedirect.com/science/article/pii/S0955221902001826.

[39] Z. Tan, Y. Chu, J. Chen, J. Li, G. Ji, G. Niu, L. Gao, Z. Xiao, and J. Tang. Lead-free perovskite variant solid solutions $Cs_2Sn_{1-x}Te_xCl_6$: Bright luminescence and high anti-water stability. *Advanced Materials*, 32(32):2002443, 2020. doi: 10.1002/adma.202002443. URL https://onlinelibrary.wiley.com/doi/abs/10.1002/adma.202002443.

[40] Chun Lin Jia, Shao Bo Mi, Knut Urban, Ionela Vrejoiu, Marin Alexe, and Dietrich Hesse. Atomic-scale study of electric dipoles near charged and uncharged domain walls in ferroelectric films. *Nature Materials*, 7(1): 57–61, 2008. doi: 10.1038/nmat2080. URL http://doi.org/10.1038/nmat2080.

[41] J. Gonnissen, D. Batuk, G. F. Nataf, L. Jones, A. M. Abakumov, S. Van Aert, D. Schryvers, and Ekhard K. H. Salje. Direct observation of ferroelectric domain walls in $LiNbO_3$: Wall-meanders, kinks, and local electric charges. *Advanced Functional Materials*, 26(42):7599–7604, 2016. doi: 10.1002/adfm.201603489. URL https://onlinelibrary.wiley.com/doi/abs/10.1002/adfm.201603489.

[42] Y. C. Shu and K. Bhattacharya. Domain patterns and macroscopic behavior of ferroelectric materials. *Philosophical Magazine B*, 81:2021–2054, 2001. doi: 10.1080/13642810108208556. URL https://doi.org/10.1080/13642810108208556.

[43] J. R. Whyte and J. M. Gregg. A diode for ferroelectric domain-wall motion. *Nature Communications*, 6:1–5, 2015. doi: 10.1038/ncomms8361. URL http://doi.org/10.1038/ncomms8361.

[44] Y. Zuo, Y. A. Genenko, A. Klein, P. Stein, and B. Xu. Domain wall stability in ferroelectrics with space charges. *Journal of Applied Physics*, 115(8): 084110, 2014. doi: 10.1063/1.4866359. URL https://doi.org/10.1063/1.4866359.

[45] G. F. Nataf, M. Guennou, J. M. Gregg, D. Meier, J. Hlinka, E. K.H. Salje, and J. Kreisel. Domain-wall engineering and topological defects in ferroelectric

and ferroelastic materials. *Nature Reviews Physics*, 2(11):634–648, 2020. doi: 10.1038/s42254-020-0235-z. URL http://dx.doi.org/10.1038/s42254-020-0235-z.

[46] P. Sharma, P. Schoenherr, and J. Seidel. Functional ferroic domain walls for nanoelectronics. *Materials*, 12(18), 2019. doi: 10.3390/ma12182927. URL https://www.mdpi.com/1996-1944/12/18/2927.

[47] B. G. Streetman and S. Banerjee. *Solid State Electronic Devices*. Prentice Hall series in solid state physical electronics. Prentice Hall, 2000. ISBN 9780130261014. URL https://books.google.com/books?id=TymhQgAACAAJ.

[48] T. Kanai, S. Ohkoshi, and K. Hashimoto. Magnetic, electric, and optical functionalities of $(PLZT)_x(BiFeO3)_{1-x}$ ferroelectric-ferromagnetic thin films. *Journal of Physics and Chemistry of Solids*, 64(3):391–397, 2003. doi: 10.1016/S0022-3697(02)00284-6. URL https://www.sciencedirect.com/science/article/pii/S0022369702002846.

[49] S. J. Clark and J. Robertson. Band gap and Schottky barrier heights of multiferroic $BiFeO_3$. *Applied Physics Letters*, 90(13):132903, March 2007. doi: 10.1063/1.2716868. URL https://doi.org/10.1063/1.2716868.

[50] Y. Watanabe. Theoretical stability of the polarization in a thin semiconducting ferroelectric. *Physical Review B*, 57:789–804, Jan 1998. doi: 10.1103/PhysRevB.57.789. URL https://link.aps.org/doi/10.1103/PhysRevB.57.789.

[51] Y. Xiao, V. B. Shenoy, and K. Bhattacharya. Depletion layers and domain walls in semiconducting ferroelectric thin films. *Physical Review Letters*, 95 (24), 2005. doi: 10.1103/PhysRevLett.95.247603. URL https://link.aps.org/doi/10.1103/PhysRevLett.95.247603.

[52] Marin Alexe and Dietrich Hesse. Tip-enhanced photovoltaic effects in bismuth ferrite. *Nature Communications*, 2(1):255–256, 2011. doi: 10.1038/ncomms1261. URL http://dx.doi.org/10.1038/ncomms1261.

[53] Marin Alexe. Local mapping of generation and recombination lifetime in $BiFeO_3$ single crystals by scanning probe photoinduced transient spectroscopy. *Nano Letters*, 12(5):2193–2198, 2012. doi: 10.1021/nl300618e. URL http://doi.org/10.1021/nl300618e.

[54] A. Bhatnagar, A. R. Chaudhuri, Y. H. Kim, D. Hesse, and M. Alexe. Role of domain walls in the abnormal photovoltaic effect in BiFeO3. *Nature Communications*, 4:1–8, 2013. doi: 10.1038/ncomms3835. URL http://dx.doi.org/10.1038/ncomms3835.

[55] M. M. Yang, A. Bhatnagar, Z. D. Luo, and M. Alexe. Enhancement of Local Photovoltaic Current at Ferroelectric Domain Walls in BiFeO 3. *Scientific Reports*, 7(February):1–8, 2017. doi: 10.1038/srep43070. URL http://dx.doi.org/10.1038/srep43070.

[56] R. Inoue, S. Ishikawa, R. Imura, Y. Kitanaka, T. Oguchi, Y. Noguchi, and M. Miyayama. Giant photovoltaic effect of ferroelectric domain walls in perovskite single crystals. *Scientific Reports*, 5:14741, 2015. doi: 10.1038/srep14741. URL http://www.nature.com/articles/srep14741.

[57] H. Matsuo, Y. Kitanaka, R. Inoue, Y. Noguchi, M. Miyayama, T. Kiguchi, and T. J. Konno. Bulk and domain-wall effects in ferroelectric photovoltaics. *Physical Review B*, 94(21), 2016. doi: 10.1103/PhysRevB.94.214111. URL https://journals.aps.org/prb/pdf/10.1103/PhysRevB.94.214111.

[58] B. Meyer and D. Vanderbilt. Ab initio study of ferroelectric domain walls in $PbTiO_3$. *Physical Review B*, 65(10):104111, 2002. doi: 10.1103/PhysRevB.65.104111. URL https://link.aps.org/doi/10.1103/PhysRevB.65.104111.

[59] A. Lubk, S. Gemming, and N. A. Spaldin. First-principles study of ferroelectric domain walls in multiferroic bismuth ferrite. *Physical Review B*, 80(10):1–8, 2009. doi: 10.1103/PhysRevB.80.104110. URL https://link.aps.org/doi/10.1103/PhysRevB.80.104110.

[60] O. Diéguez, P. Aguado-Puente, J. Junquera, and J. Íñiguez. Domain walls in a perovskite oxide with two primary structural order parameters: First-principles study of $BiFeO_3$. *Physical Review B*, 87(2):024102, 2013. doi: 10.1103/PhysRevB.87.024102. URL https://journals.aps.org/prb/pdf/10.1103/PhysRevB.87.024102https://link.aps.org/doi/10.1103/PhysRevB.87.024102.

[61] J. Seidel, D. Fu, S.-Y. Yang, E. Alarcón-Lladó, J. Wu, R. Ramesh, and J. W. Ager. Efficient photovoltaic current generation at ferroelectric domain walls. *Physical Review Letters*, 107(12), 2011. doi: 10.1103/PhysRevLett.107.126805. URL https://journals.aps.org/prl/pdf/10.1103/PhysRevLett.107.126805.

[62] F. Xue, Y. Gu, L. Liang, Y. Wang, and L. Q. Chen. Orientations of low-energy domain walls in perovskites with oxygen octahedral tilts. *Physical Review B - Condensed Matter and Materials Physics*, 90(22), 2014. doi: 10.1103/PhysRevB.90.220101. URL https://journals.aps.org/prb/pdf/10.1103/PhysRevB.90.220101.

[63] G. Cao, Y. Cao, H. Huang, L. Q. Chen, and X. Ma. Analysis of multi-domain ferroelectric switching in $BiFeO_3$ thin film using phase-field method. *Computational Materials Science*, 115:208–213, 2016. doi: 10.1016/j.

commatsci.2015.11.021. URL https://docuserve.library.caltech.edu/illiad/illiad.dll?Action=10{&}Form=75{&}Value=470292.

[64] P. Suryanarayana and K. Bhattacharya. Evolution of polarization and space charges in semiconducting ferroelectrics. *Journal of Applied Physics*, 111 (3):0–11, 2012. doi: 10.1063/1.3678598.

[65] Jenny Nelson. *The Physics of Solar Cells*. Imperial College Press, London, 2003.

[66] S. M. Sze. *Physics of Semiconductor Devices*. Wiley, 1969.

[67] J. M. Foster, H. J. Snaith, T. Leijtens, and G. Richardson. A Model for the Operation of Perovskite Based Hybrid Solar Cells: Formulation, Analysis, and Comparison to Experiment. *SIAM Journal on Applied Mathematics*, 74(6):1935–1966, 2014. doi: 10.1137/130934258. URL http://epubs.siam.org/doi/pdf/10.1137/130934258http://epubs.siam.org/doi/abs/10.1137/130934258.

[68] O. Diéguez, O. E. González-Vázquez, J. C. Wojdeł, and J. Íñiguez. First-principles predictions of low-energy phases of multiferroic $BiFeO_3$. *Physical Review B*, 83:094105, 2011. doi: 10.1103/PhysRevB.83.094105. URL https://link.aps.org/doi/10.1103/PhysRevB.83.094105.

[69] S. Kamba, D. Nuzhnyy, M. Savinov, J. Šebek, J. Petzelt, J. Prokleška, R. Haumont, and J. Kreisel. Infrared and terahertz studies of polar phonons and magnetodielectric effect in multiferroic $BiFeO_3$ ceramics. *Physical Review B*, 75:024403, 2007. doi: 10.1103/PhysRevB.75.024403. URL https://link.aps.org/doi/10.1103/PhysRevB.75.024403.

[70] J. F. Scott. Applications of modern ferroelectrics. *Science*, 315(5814): 954–959, 2007. doi: 10.1126/science.1129564. URL http://science.sciencemag.org/content/315/5814/954.

[4] E. Cross. Lead-free at last. *Nature*, 432:24–25, 2004. doi: 10.1038/nature03142. URL https://www.nature.com/articles/nature03142.

[71] D. Damjanovic. Contributions to the piezoelectric effect in ferroelectric single crystals and ceramics. *Journal of the American Ceramic Society*, 88: 2663–2676, 2005. doi: 10.1111/j.1551-2916.2005.00671.x. URL https://doi.org/10.1111/j.1551-2916.2005.00671.x.

[72] J. Y. Li, R. C. Rogan, E. Üstündag, and K. Bhattacharya. Domain switching in polycrystalline ferroelectric ceramics. *Nature Materials*, 4:776–781, 2005. doi: 10.1038/nmat1485. URL https://doi.org/10.1038/nmat1485.

[73] J. Wu. Perovskite lead-free piezoelectric ceramics. *Journal of Applied Physics*, 127:190901, 2020. doi: 10.1063/5.0006261. URL https://doi.org/10.1063/5.0006261.

[74] H. Fu and R. E. Cohen. Polarization rotation mechanism for ultrahigh electromechanical response in single-crystal piezoelectrics. *Nature*, 403: 281, 2000. doi: 10.1038/35002022. URL https://doi.org/10.1038/35002022.

[75] D. Cao, I.-K. Jeong, R. H. Heffner, T. Darling, J.-K. Lee, F. Bridges, J.-S. Park, and K.-S. Hong. Local structure study of the off-center displacement of Ti and Zr across the morphotropic phase boundary of $PbZr_{1-x}Ti_xO_3$ ($x = 0.40, 0.47, 0.49, 0.55$). *Physical Review B*, 70:224102, 2004. doi: 10.1103/PhysRevB.70.224102. URL https://link.aps.org/doi/10.1103/PhysRevB.70.224102.

[76] J. Noheda and D. E. Cox. Bridging phases at the morphotropic boundaries of lead oxide solid solutions. *Phase Transitions*, 79:5–20, 2005. doi: 10.1080/01411590500467262. URL https://doi.org/10.1080/01411590500467262.

[77] I. Grinberg, V. R. Cooper, and A. M. Rappe. Relationship between local structure and phase transitions of a disordered solid solution. *Nature*, 419: 909, 2002. doi: 10.1038/nature01115. URL https://doi.org/10.1038/nature01115.

[78] I. Grinberg, V. R. Cooper, and A. M. Rappe. Oxide chemistry and local structure of $PbZr_xTi_{1-x}O_3$ studied by density-functional theory supercell calculations. *Physical Review B*, 69:144118, 2004. doi: 10.1103/PhysRevB.69.144118. URL https://link.aps.org/doi/10.1103/PhysRevB.69.144118.

[79] R. Theissmann, L. A. Schmitt, J. Kling, R. Schierholz, K. A. Schönau, H. Fuess, M. Knapp, H. Kungl, and M. J. Hoffmann. Nanodomains in morphotropic lead zirconate titanate ceramics: On the origin of the strong piezoelectric effect. *Journal of Applied Physics*, 102(2):024111, 2007. doi: 10.1063/1.2753569. URL https://doi.org/10.1063/1.2753569.

[80] L. Bellaiche, A. García, and D. Vanderbilt. Finite-temperature properties of $Pb(Zr_{1-x}Ti_x)O_3$ alloys from first principles. *Physical Review Letters*, 84: 5427–5430, 2000.

[81] S. F. Edwards and P. W. Anderson. Theory of spin glasses. *Journal of Physics F: Metal Physics*, 5(5):965–974, 1975. doi: 10.1088/0305-4608/5/5/017. URL https://doi.org/10.1088/0305-4608/5/5/017.

[82] D. Sherrington and S. Kirkpatrick. Solvable model of a spin-glass. *Physical Review Letters*, 35:1792–1796, 1975. doi: 10.1103/PhysRevLett.35.1792. URL https://link.aps.org/doi/10.1103/PhysRevLett.35.1792.

[83] S. Kartha, T. Castán, J. A. Krumhansl, and J. P. Sethna. Spin-glass nature of tweed precursors in martensitic transformations. *Physical Review Letters*,

67:3630–3633, 1991. doi: 10.1103/PhysRevLett.67.3630. URL https://link.aps.org/doi/10.1103/PhysRevLett.67.3630.

[84] D.C. Mattis. Solvable spin systems with random interactions. *Physics Letters A*, 56(5):421–422, 1976. ISSN 0375-9601. doi: https://doi.org/10.1016/0375-9601(76)90396-0. URL https://www.sciencedirect.com/science/article/pii/0375960176903960.

[85] S. D. Baranovskii, A. L. Efros, B. L. Gelmont, and B. I. Shklovskii. Coulomb gap in disordered systems: computer simulation. *Journal of Physics C: Solid State Physics*, 12(6):1023–1034, 1979. doi: 10.1088/0022-3719/12/6/015. URL https://doi.org/10.1088/0022-3719/12/6/015.

[86] J. H. Davies, P. A. Lee, and T. M. Rice. Electron glass. *Physical Review Letters*, 49:758–761, Sep 1982. doi: 10.1103/PhysRevLett.49.758. URL https://link.aps.org/doi/10.1103/PhysRevLett.49.758.

[87] E. R. Grannan and C. C. Yu. Critical behavior of the coulomb glass. *Physical Review Letters*, 71:3335–3338, 1993. doi: 10.1103/PhysRevLett.71.3335. URL https://link.aps.org/doi/10.1103/PhysRevLett.71.3335.

[88] Y. Wang, X. Liu, J. D. Burton, S. S. Jaswal, and E. Y. Tsymbal. Ferroelectric instability under screened coulomb interactions. *Physical Review Letters*, 109, 2012. doi: 10.1103/PhysRevLett.109.247601. URL https://link.aps.org/doi/10.1103/PhysRevLett.109.247601.

[89] P. P. Ewald. Die Berechnung optischer und elektrostatischer Gitterpotentiale. *Annalen der Physik*, 369(3):253–287, 1921. doi: 10.1002/andp.19213690304. URL https://doi.org/10.1002/andp.19213690304.

[90] J. J. Cerdà, V. Ballenegger, O. Lenz, and C. Holm. P3M algorithm for dipolar interactions. *The Journal of Chemical Physics*, 129(23):234104, 2008. doi: 10.1063/1.3000389. URL https://doi.org/10.1063/1.3000389.

[91] D. Wang, J. Liu, J. Zhang, S. Raza, X. Chen, and C.-L. Jia. Ewald summation for ferroelectric perovksites with charges and dipoles. *Computational Materials Science*, 162:314–321, 2019. doi: 10.1016/j.commatsci.2019.03.006. URL https://www.sciencedirect.com/science/article/pii/S0927025619301302.

[92] D. Mondal and D. B. Percival. Wavelet variance analysis for random fields on a regular lattice. *IEEE Trans Image Process*, 21(2):537–549, 2012. doi: 10.1109/TIP.2011.2164412. URL http://doi.org/10.1109/TIP.2011.2164412.

[93] Y. Imry and S. Ma. Random-field instability of the ordered state of continuous symmetry. *Physical Review Letters*, 35:1399–1401, 1975. doi: 10.1103/PhysRevLett.35.1399. URL https://link.aps.org/doi/10.1103/PhysRevLett.35.1399.

[94] M. Aizenman and J. Wehr. Rounding of first-order phase transitions in systems with quenched disorder. *Physical Review Letters*, 62:2503–2506, 1989. doi: 10.1103/PhysRevLett.62.2503. URL https://link.aps.org/doi/10.1103/PhysRevLett.62.2503.

[95] T. Nattermann. Theory of the random field ising model. In A. P. Young, editor, *Spin glasses and random fields*, pages 277–298. World Scientific, 1997.

[96] L. C. Sampaio, M. P. De Albuquerque, and F. S. de Menezes. Magnetic relaxation and formation of magnetic domains in ultrathin films with perpendicular anisotropy. *Physical Review B*, 9:6465–6472, 1996. doi: 10.1103/PhysRevB.54.6465. URL https://link.aps.org/doi/10.1103/PhysRevB.54.6465.

[97] V. Kovacova, N. Vaxelaire, G. Le Rhun, P. Gergaud, T. Schmitz-Kempen, and E. Defay. Correlation between electric-field-induced phase transition and piezoelectricity in lead zirconate titanate films. *Physical Review B*, 90: 140101, 2014. doi: 10.1103/PhysRevB.90.140101. URL https://link.aps.org/doi/10.1103/PhysRevB.90.140101.

[98] A. K. Kundu. *Magnetic Perovskites*. Springer, 2016.

[99] N. A. Hill. Why are there so few magnetic ferroelectrics? *The Journal of Physical Chemistry B*, 104:6694–6709, 2000. doi: 10.1021/jp000114x. URL https://doi.org/10.1021/jp000114x.

[100] R. Bai, Y. S. Teh, and K. Bhattacharya. Collective behavior in the kinetics and equilibrium of solid-state photoreaction. *Extreme Mechanics Letters*, 43:101160, 2021. doi: 10.1016/j.eml.2020.101160. URL https://www.sciencedirect.com/science/article/pii/S2352431620303102.

[101] J. Zhuang, L.-W. Su, H. Wu, A. A. Bokov, M. Liu, W. Ren, and Z.-G. Ye. Coexisting ferroelectric and magnetic morphotropic phase boundaries in Dy-modified $BiFeO_3$-$PbTiO_3$ multiferroics. *Applied Physics Letters*, 107 (18):182906, 2015. doi: 10.1063/1.4935097. URL https://doi.org/10.1063/1.4935097.

[102] J. Zhuang, J. Lu, N. Zhang, J. Zhang, A. A. Bokov, S. Yang, W. Ren, and Z.-G. Ye. Chemically engineered multiferroic morphotropic phase boundary in $BiFeO_3$-based single phase multiferroics. *Journal of Applied Physics*, 125 (4):044102, 2019. doi: 10.1063/1.5054674. URL https://doi.org/10.1063/1.5054674.

[103] Y. N. Zhou, T. T. Gao, J. Chen, X. Q. Liu, and X. M. Chen. Morphotropic phase boundary (MPB) and enhanced multiferroic characteristics of $Bi_{1-x}(Ba_{0.75}Ca_{0.25})_xFe_{1-x}Ti_xO_3$ ceramics ($0.25 leq x leq 0.35$). *Journal of Alloys and Compounds*, 819:153031, 2020. doi: 10.1016/j.jallcom.2019.153031. URL https://www.sciencedirect.com/science/article/pii/S092583881934277X.

[104] D. G. Schlom, L.-Q. Chen, C.-B. Eom, K. M. Rabe, S. K. Streiffer, and J.-M. Triscone. Strain tuning of ferroelectric thin films. *Annual Review of Materials Research*, 37(1):589–626, 2007. doi: 10.1146/annurev.matsci.37.061206.113016. URL https://doi.org/10.1146/annurev.matsci.37.061206.113016.

[105] G. Tsutsui, S. Mochizuki, N. Loubet, S. W. Bedell, and D. K. Sadana. Strain engineering in functional materials. *AIP Advances*, 9(3):030701, 2019. doi: 10.1063/1.5075637. URL https://doi.org/10.1063/1.5075637.

[106] J. W. Christian and S. Mahajan. Deformation twinning. *Progress in Materials Science*, 39(1):1–157, 1995. doi: https://doi.org/10.1016/0079-6425(94)00007-7. URL https://www.sciencedirect.com/science/article/pii/0079642594000077.

[107] Z. K. Lu and G. J. Weng. Martensitic transformation and stress-strain relations of shape-memory alloys. *Journal of the Mechanics and Physics of Solids*, 45(11):1905–1928, 1997. doi: https://doi.org/10.1016/S0022-5096(97)00022-7. URL https://www.sciencedirect.com/science/article/pii/S0022509697000227.

[108] T. Iwamoto, T. Tsuta, and Y. Tomita. Investigation on deformation mode dependence of strain-induced martensitic transformation in trip steels and modelling of transformation kinetics. *International Journal of Mechanical Sciences*, 40(2):173–182, 1998. doi: https://doi.org/10.1016/S0020-7403(97)00047-7. URL https://www.sciencedirect.com/science/article/pii/S0020740397000477.

[109] Z. Qin and Y. Xia. Role of strain-induced martensitic phase transformation in mechanical response of 304l steel at different strain-rates and temperatures. *Journal of Materials Processing Technology*, 280:116613, 2020. doi: https://doi.org/10.1016/j.jmatprotec.2020.116613. URL https://www.sciencedirect.com/science/article/pii/S0924013620300261.

[110] Z. Dai, L. Liu, and Z. Zhang. Strain engineering of 2D materials: Issues and opportunities at the interface. *Advanced Materials*, 31(45): 1805417, 2019. doi: https://doi.org/10.1002/adma.201805417. URL https://onlinelibrary.wiley.com/doi/abs/10.1002/adma.201805417.

[111] W. Kohn and L. J. Sham. Self-consistent equations including exchange and correlation effects. *Physical Review Journals Archive*, 140:A1133–A1138, 1965. doi: 10.1103/PhysRev.140.A1133. URL https://link.aps.org/doi/10.1103/PhysRev.140.A1133.

[112] A. Jain, Y. Shin, and K. A. Persson. Computational predictions of energy materials using density functional theory. *Nature Reviews Materials*, 1(1): 1–13, 2016. doi: 10.1038/natrevmats.2015.4. URL https://doi.org/10.1038/natrevmats.2015.4.

[113] T. H. Kim, D. Puggioni, Y. Yuan, L. Xie, H. Zhou, N. Campbell, P. J. Ryan, Y. Choi, J. W. Kim, J. R. Patzner, S. Ryu, J. P. Podkaminer, J. Irwin, Y. Ma, C. J. Fennie, M. S. Rzchowski, X. Q. Pan, V. Gopalan, J. M. Rondinelli, and C. B. Eom. Polar metals by geometric design. *Nature*, 533(7601):68–72, 2016. doi: 10.1038/nature17628. URL https://doi.org/10.1038/nature17628.

[114] R. Armiento, B. Kozinsky, M. Fornari, and G. Ceder. Screening for high-performance piezoelectrics using high-throughput density functional theory. *Physical Review B*, 84:014103, 2011. doi: 10.1103/PhysRevB.84.014103. URL https://link.aps.org/doi/10.1103/PhysRevB.84.014103.

[115] Y. LeCun and Y. Bengio. *Convolutional networks for images, speech, and time series*. MIT Press, 1995.

[116] K. He, X. Zhang, S. Ren, and J. Sun. Deep residual learning for image recognition. In *Proceedings of the IEEE conference on computer vision and pattern recognition*, pages 770–778, 2016.

[117] Y. Goldberg. Neural network methods for natural language processing. *Synthesis lectures on human language technologies*, 10:1–309, 2017. doi: 10.2200/S00762ED1V01Y201703HLT037. URL https://doi.org/10.2200/S00762ED1V01Y201703HLT037.

[118] R. Collobert and J. Weston. A unified architecture for natural language processing: Deep neural networks with multitask learning. In *Proceedings of the 25th international conference on Machine learning*, pages 160–167, New York, NY, USA, 2008. Association for Computing Machinery. doi: 10.1145/1390156.1390177. URL https://doi.org/10.1145/1390156.1390177.

[119] S. R. Kalidindi and M. De Graef. Materials data science: current status and future outlook. *Annual Review of Materials Research*, 45:171–193, 2015. doi: 10.1146/annurev-matsci-070214-020844. URL https://doi.org/10.1146/annurev-matsci-070214-020844.

[120] S. Ogata, E. Lidorikis, F. Shimojo, A. Nakano, P. Vashishta, and R. K. Kalia. Hybrid finite-element/molecular-dynamics/electronic-density-functional approach to materials simulations on parallel computers. *Computer Physics Communications*, 138(2):143–154, 2001. doi: https://doi.org/10.1016/S0010-4655(01)00203-X. URL https://www.sciencedirect.com/science/article/pii/S001046550100203X.

[121] G. Csányi, T. Albaret, M. C. Payne, and A. De Vita. "learn on the fly": A hybrid classical and quantum-mechanical molecular dynamics simulation. *Physical Review Letters*, 93:175503, 2004. doi: 10.1103/PhysRevLett.93.175503. URL https://link.aps.org/doi/10.1103/PhysRevLett.93.175503.

[122] R. Khare, S. L. Mielke, J. T. Paci, S. Zhang, R. Ballarini, G. C. Schatz, and T. Belytschko. Coupled quantum mechanical/molecular mechanical modeling of the fracture of defective carbon nanotubes and graphene sheets. *Physical Review B*, 75:075412, 2007. doi: 10.1103/PhysRevB.75.075412. URL https://link.aps.org/doi/10.1103/PhysRevB.75.075412.

[123] J. R. Kermode, T. Albaret, D. Sherman, N. Bernstein, P. Gumbsch, M. C. Payne, G. Csányi, and A. De Vita. Low-speed fracture instabilities in a brittle crystal. *Nature*, 455(7217):1224–1227, 2008. doi: 10.1038/nature07297. URL https://doi.org/10.1038/nature07297.

[124] N. Bernstein, J. R. Kermode, and G. Csányi. Hybrid atomistic simulation methods for materials systems. *Reports on Progress in Physics*, 72(2):026501, 2009. doi: 10.1088/0034-4885/72/2/026501. URL https://doi.org/10.1088/0034-4885/72/2/026501.

[125] C. Woodward, D. R. Trinkle, L. G. Hector, and D. L. Olmsted. Prediction of dislocation cores in aluminum from density functional theory. *Physical Review Letters*, 100, 2008. doi: 10.1103/PhysRevLett.100.045507. URL https://link.aps.org/doi/10.1103/PhysRevLett.100.045507.

[126] M. Ponga, K. Bhattacharya, and M. Ortiz. Large scale ab-initio simulations of dislocations. *Journal of Computational Physics*, 407:109249, 2020. doi: https://doi.org/10.1016/j.jcp.2020.109249. URL https://www.sciencedirect.com/science/article/pii/S0021999120300231.

[127] K. Bhattacharya, B. Hosseini, N. B. Kovachki, and A. M. Stuart. Model reduction and neural networks for parametric pdes. *arXiv preprint arXiv:2005.03180*, 2020.

[128] A. Chandrasekaran, D. Kamal, R. Batra, C. Kim, L. Chen, and R. Ramprasad. Solving the electronic structure problem with machine learning. *npj Computational Materials*, 5(1), 2019. doi: 10.1038/s41524-019-0162-7. URL http://dx.doi.org/10.1038/s41524-019-0162-7.

[129] A. Grisafi, A. Fabrizio, B. Meyer, D. M. Wilkins, C. Corminboeuf, and M. Ceriotti. Transferable machine-learning model of the electron density. *ACS Central Science*, 5(1):57–64, 2019. doi: 10.1021/acscentsci.8b00551. URL https://doi.org/10.1021/acscentsci.8b00551.

[130] F. Brockherde, L. Vogt, L. Li, M. E. Tuckerman, K. Burke, and K. R. Müller. Bypassing the Kohn-Sham equations with machine learning. *Nature Communications*, 8(1), 2017. doi: 10.1038/s41467-017-00839-3. URL http://doi.org/10.1038/s41467-017-00839-3.

[131] N. Marzari. Ab-initio Molecular Dynamics for Metallic Systems. *Thesis*, Ph.D.(April), 1996. URL http://quasiamore.mit.edu/phd/.

[132] X. Gonze, B. Amadon, G. Antonius, F. Arnardi, L. Baguet, J.-M. Beuken, J. Bieder, F. Bottin, J. Bouchet, E. Bousquet, N. Brouwer, F. Bruneval, G. Brunin, T. Cavignac, J.-B. Charraud, W. Chen, M. Côté, S. Cottenier, J. Denier, G. Geneste, P. Ghosez, M. Giantomassi, Y. Gillet, O. Gingras, D. R. Hamann, G. Hautier, X. He, N. Helbig, N. Holzwarth, Y. Jia, F. Jollet, W. Lafargue-Dit-Hauret, K. Lejaeghere, M. A. L. Marques, A. Martin, C. Martins, H. P. C. Miranda, F. Naccarato, K. Persson, G. Petretto, V. Planes, Y. Pouillon, S. Prokhorenko, F. Ricci, G.-M. Rignanese, A. H. Romero, M. M. Schmitt, M. Torrent, M. J. van Setten, B. V. Troeye, M. J. Verstraete, G. Zérah, and J. W. Zwanziger. The Abinit project: Impact, environment and recent developments. *Computer Physics Communications*, 248:107042, 2020. doi: 10.1016/j.cpc.2019.107042. URL https://www.sciencedirect.com/science/article/pii/S0010465519303741.

[133] W. J. Joost and P. E. Krajewski. Towards magnesium alloys for high-volume automotive applications. *Scripta Materialia*, 128:107–112, 2017. doi: https://doi.org/10.1016/j.scriptamat.2016.07.035. URL https://www.sciencedirect.com/science/article/pii/S1359646216303621.

[134] M. K. Kulekci. Magnesium and its alloys applications in automotive industry. *The International Journal of Advanced Manufacturing Technology*, 39(9-10): 851–865, 2008. doi: 10.1007/s00170-007-1279-2. URL https://doi.org/10.1007/s00170-007-1279-2.

[135] X. Chen, Y. Geng, and F. Pan. Research progress in magnesium alloys as functional materials. *Rare Metal Materials and Engineering*, 45 (9):2269–2274, 2016. doi: https://doi.org/10.1016/S1875-5372(17)30015-2. URL https://www.sciencedirect.com/science/article/pii/S1875537217300152.

[136] J. A. Pople. Nobel lecture: Quantum chemical models. *Reviews of Modern Physics*, 71:1267–1274, 1999. doi: 10.1103/RevModPhys.71.1267. URL https://link.aps.org/doi/10.1103/RevModPhys.71.1267.

[137] J. L. Ericksen. On the cauchy—born rule. *Mathematics and Mechanics of Solids*, 13(3-4):199–220, 2008. doi: 10.1177/1081286507086898. URL https://doi.org/10.1177/1081286507086898.

[138] O. H. Nielsen and Richard M. Martin. Quantum-mechanical theory of stress and force. *Physical Review B*, 32:3780–3791, 1985. doi: 10.1103/PhysRevB.32.3780. URL https://link.aps.org/doi/10.1103/PhysRevB.32.3780.

[139] N. V. Ilawe, J. A. Zimmerman, and B. M. Wong. Breaking badly: DFT-D2 gives sizeable errors for tensile strengths in palladium-hydride solids. *Journal of Chemical Theory and Computation*, 11(11):5426–5435, 2015. doi: 10.1021/acs.jctc.5b00653. URL https://doi.org/10.1021/acs.jctc.5b00653.

[140] J. Barzilai and J. M. Borwein. Two-Point Step Size Gradient Methods. *IMA Journal of Numerical Analysis*, 8(1):141–148, 1988. doi: 10.1093/imanum/8.1.141. URL https://doi.org/10.1093/imanum/8.1.141.

[141] Q. Liu, C. Fan, and R. Zhang. First-principles study of high-pressure structural phase transitions of magnesium. *Journal of Applied Physics*, 105:123505, 2009. doi: 10.1063/1.3151687. URL https://doi.org/10.1063/1.3151687.

[142] J. Seidel, P. Maksymovych, Y. Batra, A. Katan, S.-Y. Yang, Q. He, A. P. Baddorf, S. V. Kalinin, C.-H. Yang, J.-C. Yang, Y.-H. Chu, E. K. H. Salje, H. Wormeester, M. Salmeron, and R. Ramesh. Domain wall conductivity in la-doped bifeo$_3$. *Physical Review Letters*, 105:197603, 2010. doi: 10.1103/PhysRevLett.105.197603. URL https://link.aps.org/doi/10.1103/PhysRevLett.105.197603.

[143] S. M. Young, F. Zheng, and A. M. Rappe. First-principles calculation of the bulk photovoltaic effect in bismuth ferrite. *Physical Review Letters*, 109:236601, Dec 2012. doi: 10.1103/PhysRevLett.109.236601. URL https://link.aps.org/doi/10.1103/PhysRevLett.109.236601.

[144] Arti, S. Kumar, P. Kumar, R. Walia, and V. Verma. Improved ferroelectric, magnetic and photovoltaic properties of pr doped multiferroic bismuth ferrites for photovoltaic application. *Results in Physics*, 14:102403, 2019. doi: 10.1016/j.rinp.2019.102403. URL https://www.sciencedirect.com/science/article/pii/S2211379719315001.

[145] K. Binder and D. Heermann. *Monte Carlo Simulation in Statistical Physics : An Introduction*, volume 80. Springer, 01 2010. doi: 10.1007/978-3-642-03163-2.

[146] J. D. Jackson. *Classical electrodynamics*. Wiley, New York, 2 edition, 1975.

[147] H. Lee and W. Cai. Ewald summation for coulomb interactions in a periodic supercell, January 2009.

[148] D. Frenkel and B. Smit. *Understanding Molecular Simulation*. Academic Press, Inc., Orlando, FL, USA, 2nd edition, 2001. ISBN 0122673514.

[149] M. C. Payne, M. P. Teter, D. C. Allan, T. A. Arias, and J. D. Joannopoulos. Iterative minimization techniques for ab initio total-energy molecular dynamics and conjugate gradients calculations: molecular dynamics and conjugate gradients. *Reviews of Modern Physics*, 64(4):1045–1097, 1992. doi: 10.1103/RevModPhys.64.1045. URL https://link.aps.org/doi/10.1103/RevModPhys.64.1045.

Appendix A

DERIVATION OF DEVICE MODEL FOR INVESTIGATING PHOTOVOLTAIC EFFECT

We show some details regarding the derivation and implementation of the device model proposed in Chapter 3.

A.1 Derivation involved in the thermodynamically consistent theory

We prove equation (3.43) in Chapter 3.4 below.

Consider the right hand side of (3.43)

$$\begin{aligned}
\frac{d}{dt}\left(\frac{\varepsilon_0}{2}\int_{\mathbb{R}_3}|\nabla\phi|^2 dV\right) &= \varepsilon_0\int_{\mathbb{R}_3}\nabla\phi\cdot\nabla\dot{\phi}\,dV \\
&= \varepsilon_0\int_{\mathbb{R}_3}\nabla\cdot\left(\phi\nabla\dot{\phi}\right)dV - \varepsilon_0\int_{\mathbb{R}_3}\phi\left(\nabla\cdot\nabla\dot{\phi}\right)dV \\
&= \varepsilon_0\int_{\mathbb{R}_3\backslash\Omega}\nabla\cdot\left(\phi\nabla\dot{\phi}\right)dV + \varepsilon_0\int_{\Omega}\nabla\cdot\left(\phi\nabla\dot{\phi}\right)dV \\
&\quad - \varepsilon_0\int_{\mathbb{R}_3}\phi\left(\nabla\cdot\nabla\dot{\phi}\right)dV \\
&= \varepsilon_0\int_{\partial\mathbb{R}_3}\left(\phi\nabla\dot{\phi}\right)\cdot\hat{\mathbf{n}}\,dS + \varepsilon_0\int_{\partial\Omega^+}\left(\phi\nabla\dot{\phi}\right)\cdot(-\hat{\mathbf{n}})\,dS \\
&\quad + \varepsilon_0\int_{\partial\Omega^-}\left(\phi\nabla\dot{\phi}\right)\cdot\hat{\mathbf{n}}\,dS - \varepsilon_0\int_{\mathbb{R}_3}\phi\left(\nabla\cdot\nabla\dot{\phi}\right)dV \\
&= -\varepsilon_0\int_{\partial\Omega}\phi[\![\nabla\dot{\phi}]\!]\cdot\hat{\mathbf{n}}\,dS - \varepsilon_0\int_{\mathbb{R}_3}\phi\left(\nabla\cdot\nabla\dot{\phi}\right)dV. \qquad \text{(A.1)}
\end{aligned}$$

Due to the discontinuity of the quantity $\nabla\dot{\phi}$ at the boundary $\partial\Omega$, we have to separate the regions $\mathbb{R}^3\backslash\Omega$ and Ω before applying the divergence theorem. From the boundary condition $\phi \to 0$ as $|\mathbf{x}| \to \infty$, the first term in the fourth line of the above equation is zero. It is noteworthy that material deformation is not considered in the above formulation, which allows us to easily switch the sequence of time derivative and spatial derivative, therefore simplifying the derivations.

Using the time derivative forms of Gauss's equation and surface charge density

$$\nabla\cdot(-\varepsilon_0\nabla\dot{\phi} + \dot{\mathbf{p}}) = \chi q(z_d\dot{N}_d^+ - z_a\dot{N}_a^- - \dot{n}_c + \dot{p}_v), \qquad \text{(A.2)}$$

$$\dot{\sigma} = [\![-\varepsilon_0 \nabla \dot{\phi} + \chi \dot{\mathbf{p}}]\!] \cdot \hat{\mathbf{n}}, \tag{A.3}$$

we have

$$\begin{aligned}
\frac{d}{dt}\left(\frac{\varepsilon_0}{2}\int_{\mathbb{R}_3} |\nabla\phi|^2 dV\right) &= -\varepsilon_0 \int_{\partial\Omega} \phi [\![\nabla\dot{\phi}]\!] \cdot \hat{\mathbf{n}}\, dS - \int_{\Omega} \phi\, \nabla \cdot \dot{\mathbf{p}}\, dV \\
&\quad + \int_{\Omega} \phi\, q\, (z_d \dot{N}_d^+ - z_a \dot{N}_a^- - \dot{n}_c + \dot{p}_v) dV \\
&= \int_{\partial\Omega} \phi [\![-\varepsilon_0 \nabla\dot{\phi} + \chi\dot{\mathbf{p}}]\!] \cdot \hat{\mathbf{n}}\, dS + \int_{\Omega} \nabla\phi \cdot \dot{\mathbf{p}}\, dV \\
&\quad + \int_{\Omega} \phi\, q\, (z_d \dot{N}_d^+ - z_a \dot{N}_a^- - \dot{n}_c + \dot{p}_v) dV \\
&= \int_{\partial\Omega_1 \cup \partial\Omega_2} \phi\, \dot{\sigma}\, dS + \int_{\Omega} \nabla\phi \cdot \dot{\mathbf{p}}\, dV \\
&\quad + \int_{\Omega} \phi\, q\, (z_d \dot{N}_d^+ - z_a \dot{N}_a^- - \dot{n}_c + \dot{p}_v) dV,
\end{aligned} \tag{A.4}$$

recovering (3.43). The last equality is attained by using the fact that $\sigma = 0$ on $\partial\Omega \backslash (\partial\Omega_1 \cup \partial\Omega_2)$.

A.2 Non-dimensionalization and scaling

As mentioned in Chapter 3.5, before solving for the device model numerically, we introduce dimensionless variables through appropriate scalings as follows:

$$
\begin{aligned}
p_r &= p_0 \overline{p}_r \\
p_s &= p_0 \overline{p}_s \\
\theta_r &= \theta_0 \overline{\theta}_r \\
\theta_s &= \theta_0 \overline{\theta}_s \\
r &= L_0 \overline{r} \\
W_{DL} &= W_0 \overline{W}_{DL} \\
\phi &= \phi_0 \overline{\phi} \\
n_c &= N_0 \overline{n}_c \\
p_v &= N_0 \overline{p}_v \\
N_d^+ &= N_0 \overline{N}_d^+ \\
N_a^- &= N_0 \overline{N}_a^- \\
N_i &= N_0 \overline{N}_i \\
J_n &= J_0 \overline{J}_n \\
J_p &= J_0 \overline{J}_p \\
J_{total} &= q J_0 \overline{J}_{total} \\
G &= G_0 \overline{G},
\end{aligned}
$$

where

$$
\begin{aligned}
\{p_0, \theta_0\} &= \arg\min_{p,\theta} (W_{DL}|_{|p_1|=|p_2|=|p_3|=p, |\theta_1|=|\theta_2|=|\theta_3|=\theta}) \\
N_0 &= 1 \times 10^{21}\ \mathrm{m}^{-3} \\
L_0 &= p_0 \sqrt{\frac{a_0}{W_0}} = 3.9609 \times 10^{-8}\ \mathrm{m} \\
J_0 &= G_0 L_0 \\
\phi_0 &= \frac{a_0 p_0}{L_0},
\end{aligned}
$$

and W_0 is taken to be the energy barrier across the corresponding type of domain wall. The steady-state non-dimensionalized equations are

$$
\frac{d^2 \overline{p}_r}{d\overline{r}^2} - \frac{\partial \overline{W}_{DL}}{\partial \overline{p}_r} - \frac{d\overline{\phi}}{d\overline{r}} = 0 \tag{A.5}
$$

$$\frac{d^2\overline{p}_s}{d\overline{r}^2} - \frac{\partial \overline{W}_{DL}}{\partial \overline{p}_s} = 0 \tag{A.6}$$

$$\overline{b}_0 \frac{d^2\overline{\theta}_r}{d\overline{r}^2} - \frac{\partial \overline{W}_{DL}}{\partial \overline{\theta}_r} = 0 \tag{A.7}$$

$$\overline{b}_0 \frac{d^2\overline{\theta}_s}{d\overline{r}^2} - \frac{\partial \overline{W}_{DL}}{\partial \overline{\theta}_s} = 0 \tag{A.8}$$

$$\overline{\epsilon}_0 \frac{d^2\overline{\phi}}{d\overline{r}^2} - \frac{d\overline{p}_r}{d\overline{r}} + \delta(-\overline{n}_c + \overline{p}_v + \overline{N}_d^+ - \overline{N}_a^-) = 0 \tag{A.9}$$

$$\overline{J}_n = -K_n(\frac{d\overline{n}_c}{d\overline{r}} - \overline{\beta}\phi_0\overline{n}_c\frac{d\overline{\phi}}{d\overline{r}}) \tag{A.10}$$

$$\overline{J}_p = -K_p(\frac{d\overline{p}_v}{d\overline{r}} + \overline{\beta}\phi_0\overline{p}_v\frac{d\overline{\phi}}{d\overline{r}}) \tag{A.11}$$

$$-\frac{d}{d\overline{r}}\overline{J}_n + \overline{G} - \overline{B}(\overline{n}_c\overline{p}_v - \overline{N}_i^2) = 0 \tag{A.12}$$

$$-\frac{d}{d\overline{r}}\overline{J}_p + \overline{G} - \overline{B}(\overline{n}_c\overline{p}_v - \overline{N}_i^2) = 0, \tag{A.13}$$

where

$$\overline{b}_0 = \frac{b_0\theta_0^2}{W_0L_0^2}$$
$$\overline{\epsilon}_0 = \frac{\epsilon_0\phi_0}{L_0p_0}$$
$$\delta = \frac{qN_0L_0}{p_0}$$
$$K_n = \frac{\nu_nN_0}{q\beta L_0J_0}$$
$$K_p = \frac{\nu_pN_0}{q\beta L_0J_0}$$
$$\overline{B} = \frac{BN_0^2}{G_0}.$$

Appendix B

TRANSITION PROBABILITY IN MARKOV CHAIN MONTE CARLO METHOD

Following [145], a Markov chain of configurations can be obtained by constructing a random walk through the configurational space using fictitious kinetics in terms of Monte Carlo (MC) time. Let $P(X_t = r)$ be the probability of being in configuration r at MC time t, and $P(X_{t+1} = s \mid X_t = r)$ be the probability of transiting from state r to state s per unit time. It follows that

$$P(X_{t+1} = r) = P(X_t = r) + \sum_s \Big[P(X_{t+1} = r \mid X_t = s)P(X_t = s) - P(X_{t+1} = s \mid X_t = r)P(X_t = r)\Big]. \tag{B.1}$$

At large t, equilibrium is reached and we have $P(X_{t+1} = r) = P(X_t = r)$. A sufficient condition for attaining an equilibrium probability distribution is the detailed balance condition, given by

$$P(X_{t+1} = r \mid X_t = s)P(X_t = s) = P(X_{t+1} = s \mid X_t = r)P(X_t = r). \tag{B.2}$$

With the Boltzmann distribution being the probability distribution, the detailed balance condition becomes

$$\frac{P(X_{t+1} = s \mid X_t = r)}{P(X_{t+1} = r \mid X_t = s)} = \frac{P(X_t = s)}{P(X_t = r)} = \exp\left[-\beta(W^{(s)} - W^{(r)})\right]. \tag{B.3}$$

In the context of our multi-state Ising model, we may interprete state r or s above as one possible distribution of all dipole states on a periodic lattice. Since there are N number of lattice sites and N_{states} states at each lattice point, we have a total of $(N_{states})^N$ possible distributions (i.e. $(N_{states})^N$ possible r or s states). However at each MC step, we only attempt to update the dipole state at one randomly chosen site i. Therefore the current state r differs from the next state s only by the dipole state at site i while the dipole states at other sites remain the same. To satisfy the above condition (B.3), we choose to update the dipole state at each lattice site i to one of the N_{states} possible dipole states according to the following transition probability

$$P(X_{t+1} = s \mid X_t = r) = \frac{\exp\left(-\beta W^{(s)}\right)}{\sum_{r=1}^{N_{states}} \exp\left(-\beta W^{(r)}\right)}. \tag{B.4}$$

Appendix C

DERIVATION OF DIPOLE-DIPOLE ENERGY

We derive the electrostatic energy due to dipole-dipole interaction that is applicable to both two- and three-dimensional cases. In the first part (Appendix C.1), we present the derivation that leads to equation (4.4) in Section 4.2. In the second part (Appendix C.2), we decompose this term following the Ewald summation to obtain equation (4.6) in Section 4.3.

C.1 Derivation of dipole-dipole interaction energy in direct summation form

Consider an infinite field of polarization, $\mathbf{p}(\mathbf{x})$, in the d-dimensional space with a periodicity of $V \in \mathbb{R}^d$. Mathematically, $\mathbf{p}(\mathbf{x}+\mathbf{R}) = \mathbf{p}(\mathbf{x})$ for any translation vector $\mathbf{R}$. The polarization field, also known as the density of dipole moment, generates an electrostatic potential $\phi(\mathbf{x})$ following Gauss' law

$$\nabla^2\phi(\mathbf{x}) = \frac{1}{\epsilon_0}\nabla\cdot\mathbf{p}. \tag{C.1}$$

The electrostatic energy stored in the periodic supercell V is given by

$$\begin{aligned} W_{dip} &= -\frac{1}{2}\epsilon_0\int_V \phi\,\nabla^2\phi\,d\mathbf{x} \\ &= -\frac{1}{2}\int_V \phi\,\nabla\cdot\mathbf{p}\,d\mathbf{x}, \end{aligned}$$

where Gauss' equation is used in the last line. The electrostatic energy can be interpreted as the energy induced by a distributed charge with density $-\nabla\cdot\mathbf{p}$, or the dipole-dipole Coulombic interaction energy.

The electrostatic potential $\phi(\mathbf{x})$ in equation (C.1) can be solved using the Green's function as

$$\phi(\mathbf{x}) = \int_{\mathbb{R}^d} G(\mathbf{x},\mathbf{x}')\frac{1}{\epsilon_0}\nabla_{\mathbf{x}'}\cdot\mathbf{p}(\mathbf{x}')\,d\mathbf{x}' \tag{C.2}$$

where the Green's function $G(\mathbf{x},\mathbf{x}')$ satisfies

$$\nabla^2 G(\mathbf{x},\mathbf{x}') = \delta(\mathbf{x}-\mathbf{x}') \tag{C.3}$$

and has the solutions of

$$G(\mathbf{x},\mathbf{x}') = \begin{cases} \dfrac{1}{2\pi}\ln|\mathbf{x}-\mathbf{x}'|, & d=2 \\ -\dfrac{1}{4\pi}\dfrac{1}{|\mathbf{x}-\mathbf{x}'|}, & d=3 \end{cases} \tag{C.4}$$

when solved in polar coordinates and spherical cases for the 2D and 3D cases, respectively.

Writing equation (C.2) in terms of the periodic volume V and applying the divergence theorem give

$$\begin{aligned}\phi(\mathbf{x}) &= \frac{1}{\epsilon_0}\sum_{\mathbf{R}}\int_V G(\mathbf{x},\mathbf{x}'+\mathbf{R})\nabla_{\mathbf{x}'}\cdot\mathbf{p}(\mathbf{x}')\,d\mathbf{x}' \\ &= \frac{1}{\epsilon_0}\sum_{\mathbf{R}}\left[\int_{\partial V} G(\mathbf{x}-\mathbf{R},\mathbf{x}')\mathbf{p}(\mathbf{x}')\cdot\mathbf{n}\,dS - \int_V (\mathbf{p}(\mathbf{x}')\cdot\nabla_{\mathbf{x}'})\,G(\mathbf{x}-\mathbf{R},\mathbf{x}')\,d\mathbf{x}'\right] \\ &= -\frac{1}{\epsilon_0}\int_V (\mathbf{p}(\mathbf{x}')\cdot\nabla_{\mathbf{x}'})\sum_{\mathbf{R}} G(\mathbf{x}-\mathbf{R},\mathbf{x}')\,d\mathbf{x}'. \qquad \text{(C.5)}\end{aligned}$$

The first term in the second line vanishes due to the summation over the surface of the periodic volume. Similarly, applying the divergence theorem to the energy gives

$$W_{dip} = \frac{1}{2}\int_V \mathbf{p}(\mathbf{x})\cdot\nabla\phi(\mathbf{x})\,d\mathbf{x}. \qquad \text{(C.6)}$$

Substituting equation (C.5) into equation (C.6) gives

$$W_{dip} = -\frac{1}{2\epsilon_0}\int_V (\mathbf{p}(\mathbf{x})\cdot\nabla_{\mathbf{x}})\int_V (\mathbf{p}(\mathbf{x}')\cdot\nabla_{\mathbf{x}'})\sum_{\mathbf{R}} G(\mathbf{x}-\mathbf{R},\mathbf{x}')\,d\mathbf{x}'\,d\mathbf{x}. \qquad \text{(C.7)}$$

For convenience later, we introduce the dipole density function $\boldsymbol{p}(\mathbf{r})$ such that it is equal to the periodic part of the polarization function. This function can be used to replace the function $\mathbf{p}(\mathbf{x})$ in the previous equation.

$$\boldsymbol{p}(\mathbf{x}) = \begin{cases}\mathbf{p}(\mathbf{x}), & \mathbf{x}\in V \\ 0, & \text{otherwise.}\end{cases} \qquad \text{(C.8)}$$

With N dipoles at discrete points $\mathbf{x}_i$ in the supercell, we have

$$\boldsymbol{p}(\mathbf{x}) = \sum_{i=1}^{N}\boldsymbol{p}_i\,\delta(\mathbf{x}-\mathbf{x}_i). \qquad \text{(C.9)}$$

Substituting equations (C.4) and (C.9), the electrostatic energy becomes

$$W_{dip} = \frac{1}{4\pi\epsilon_0}\sum_{i,j=1}^{N}{\sum_{\mathbf{R}}}'\frac{1}{x_{ij}^2}\left[\boldsymbol{p}_i\cdot\boldsymbol{p}_j - \frac{2(\boldsymbol{p}_i\cdot\mathbf{x}_{ij})(\boldsymbol{p}_j\cdot\mathbf{x}_{ij})}{x_{ij}^2}\right] + W_{dip}^{self} \qquad \text{(C.10)}$$

for the 2D case, and

$$W_{dip} = \frac{1}{8\pi\varepsilon_0}\sum_{i,j=1}^{N}{\sum_{\mathbf{R}}}'\frac{1}{x_{ij}^3}\left[\boldsymbol{p}_i\cdot\boldsymbol{p}_j - \frac{3(\boldsymbol{p}_i\cdot\mathbf{x}_{ij})(\boldsymbol{p}_j\cdot\mathbf{x}_{ij})}{x_{ij}^2}\right] + W_{dip}^{self} \qquad \text{(C.11)}$$

for the 3D case, where $\mathbf{x}_{ij} = \mathbf{x}_i - \mathbf{x}_j - \mathbf{R}$. Following [90], the symbol (,) above the summation sign denotes the omission of the term $\mathbf{R} = \mathbf{0}$ during summation when $i = j$ to prevent the inclusion of the self-interaction term. Otherwise, this first term would not be finite. This term is also equal to the total interaction energy between any two idealized point dipoles. However, in actual, an electric dipole corresponds a localized distribution of charges, and it takes energy to assemble a dipole from infinitesimal parts. We call this the corrected self-energy which has an expression as in equation (C.12). This self-energy term is needed to ensure that the electric field is curl-free everywhere and can be derived in a similar manner as [146]. In the continuum formulation that we begin with, there is no need for such consideration since a continuous distribution of electric dipoles is used, and hence the energy of interaction of each infinitesimal dipole with all other infinitesimal dipoles is included. Note that this self-energy term can be omitted when all the electric dipoles considered have the same magnitudes, so the change in energy due to the change in dipole states in each Monte Carlo step would not be affected by that term.

$$W_{dip}^{self} = \frac{1}{2d\epsilon_0} \sum_{i=1}^{N} |\boldsymbol{p}_i|^2, \quad d = 2, 3. \tag{C.12}$$

In summary, we have

$$W_{dip} = \frac{1}{4\pi\epsilon_0(d-1)} \sum_{i,j=1}^{N} \dot{\sum_{\mathbf{R}}} \frac{1}{x_{ij}^2} \left[\boldsymbol{p}_i \cdot \boldsymbol{p}_j - \frac{d(\boldsymbol{p}_i \cdot \mathbf{x}_{ij})(\boldsymbol{p}_j \cdot \mathbf{x}_{ij})}{x_{ij}^2} \right] + \frac{1}{2d\epsilon_0} \sum_{i=1}^{N} |\boldsymbol{p}_i|^2, \tag{C.13}$$

which is the same as equation (4.4) with $D_e = \frac{1}{4\pi\epsilon_0}$.

C.2 Derivation of dipole-dipole interaction energy following Ewald summation

Since the summation in equation (C.10) for the dipole-dipole interaction energy is only conditionally convergent, we attempt to rewrite it using Ewald decomposition.

Reciprocal-space term (W_{dip}^k)

Using Parseval's theorem and the convolution theorem for Fourier series, as well as the fact that the Fourier series of the following periodic functions are related to the

Fourier transforms $\widetilde{\boldsymbol{p}}(\mathbf{k})$ and $\widetilde{G}(\mathbf{k})$,

$$\mathcal{FS}[\mathbf{p}(\mathbf{x})] = \frac{1}{V}\widetilde{\boldsymbol{p}}(\mathbf{k})$$

$$\begin{aligned}\mathcal{FS}[\sum_{\mathbf{R}} G(\mathbf{x}-\mathbf{R})] &= \int_V \sum_{\mathbf{R}} G(\mathbf{x}-\mathbf{R})\exp(-i\mathbf{k}\cdot\mathbf{x})\,d\mathbf{x} \\ &= \int_{\mathbb{R}^d} G(\mathbf{x})\exp(-i\mathbf{k}\cdot\mathbf{x})\,d\mathbf{x} \\ &= \widetilde{G}(\mathbf{k}),\end{aligned}$$

the dipole-dipole interaction energy can be expressed in the Fourier space as

$$W_{dip} - W_{dip}^{self} = -\frac{1}{2\epsilon_0}\frac{1}{V}\sum_{\mathbf{k}\in\mathbb{K}^d} |\widetilde{\boldsymbol{p}}(\mathbf{k})\cdot i\mathbf{k}|^2\widetilde{G}(\mathbf{k})$$

where $\widetilde{\boldsymbol{p}}(\mathbf{k}) = \sum_{i=1}^{N} \boldsymbol{p}_i \exp^{-i\mathbf{k}\cdot\mathbf{x}_i}$, $\widetilde{G}(\mathbf{k}) = -1/k^2$, and $\mathbb{K}^d$ is the reciprocal lattice. The series is again not convergent as it includes the fictitious self-interaction terms that contribute to the high frequency components. Following [147], this problem can be solved by regularizing the Dirac delta function in Eqn (C.3) with a Gaussian function $g_\sigma(x) = (2\pi\sigma^2)^{-d/2}\exp\left(-\frac{x^2}{2\sigma^2}\right)$ where $\lim_{\sigma\to 0} g_\sigma(x) = \delta(x)$. Then we introduce the decomposition

$$G(\mathbf{x},\mathbf{x}') = G_\sigma(\mathbf{x},\mathbf{x}') + G_r(\mathbf{x},\mathbf{x}')$$

with the modified Green's function $G_\sigma(\mathbf{x},\mathbf{x}')$ that satisfies

$$\nabla^2 G_\sigma(\mathbf{x},\mathbf{x}') = g_\sigma(|\mathbf{x}-\mathbf{x}'|). \tag{C.14}$$

Now, converting equation (C.14) to Fourier space gives

$$\begin{aligned}-k^2\widetilde{G}_\sigma(\mathbf{k}) &= \int_{\mathbb{R}^d} \frac{1}{(2\pi\sigma^2)^{d/2}}\exp\left(-\frac{x^2}{2\sigma^2}\right)\exp(-i\mathbf{k}\cdot\mathbf{x})d\mathbf{x} \\ &= \frac{1}{(2\pi\sigma^2)^{d/2}}\prod_{i=1}^{d}\left[\int_{-\infty}^{\infty}\exp\left(-\frac{x_i^2}{2\sigma^2}\right)\exp(-ik_i x_i)dr_i\right] \\ &= \exp(-k^2\sigma^2/2).\end{aligned}$$

The last line is obtained using the identity $\int_{-\infty}^{\infty}\exp(-bx^2)\exp(iax)dx = \sqrt{\frac{\pi}{b}}\exp\left(-\frac{a^2}{4b}\right)$. Finally,

$$\widetilde{G}_\sigma(\mathbf{k}) = -\frac{1}{k^2}\exp(-k^2\sigma^2/2). \tag{C.15}$$

The remaining term $G_r(\mathbf{x}, \mathbf{x}')$ will be determined later.

Now, we have

$$W_{dip} - W_{dip}^{self} = W_{dip}^{k} + W_{dip}^{r} - W_{dip}^{k\_self} + W_{dip}^{surf}$$

with

$$W_{dip}^{k} = -\frac{1}{2\epsilon_0}\frac{1}{V}\sum_{\substack{\mathbf{k}\neq\mathbf{0}\\ \mathbf{k}\in\mathbb{K}^d}} |\widetilde{\boldsymbol{p}}(\mathbf{k})\cdot i\mathbf{k}|^2 \widetilde{G}_\sigma(\mathbf{k}). \tag{C.16}$$

Real-space term (W_{dip}^r)
To find W_{dip}^r, we observe that

$$\begin{aligned}
-\widetilde{G}(\mathbf{k}) &= \frac{1}{k^2}\\
&= \int_0^\infty \exp(-k^2 t)dt\\
&= \int_0^\eta \exp(-k^2 t)dt + \int_\eta^\infty \exp(-k^2 t)dt\\
&= \int_0^\eta \exp(-k^2 t)dt + \frac{1}{k^2}\exp(-k^2\eta).
\end{aligned}$$

The last term is equal to $-\widetilde{G}_\sigma(\mathbf{k})$ if we set $\eta = \sigma^2/2$. It follows that

$$\widetilde{G}_r(\mathbf{k}) = -\int_0^{\sigma^2/2} \exp(-k^2 t)dt.$$

The expression of G_r can be obtained by taking the inverse Fourier transform. In the 2D case, we have

$$\begin{aligned}
G_r(\mathbf{x}) &= -\frac{1}{(2\pi)^2}\int_{\mathbb{R}^2} \widetilde{G}_r(\mathbf{k})\exp(i\mathbf{k}\cdot\mathbf{x})\,d\mathbf{k}\\
&= -\frac{1}{4\pi^2}\int_0^{\sigma^2/2}\int_{\mathbb{R}^2} \exp(-k^2 t)\exp(i\mathbf{k}\cdot\mathbf{x})\,d\mathbf{k}\,dt\\
&= -\frac{1}{4\pi^2}\int_0^{\sigma^2/2}\frac{\pi}{t}\exp\left(-\frac{x^2}{4t}\right)dt\\
&= \frac{1}{4\pi}\mathrm{Ei}\left(-\frac{x^2}{2\sigma^2}\right).
\end{aligned}$$

Notice that G_r rapidly decays as r^2 increases. Therefore,

$$W_{dip}^{r} = -\frac{1}{2\epsilon_0}\sum_{i,j=1}^{N}{\sum_{\mathbf{R}}}^{,}(\boldsymbol{p}_i\cdot\nabla_{\mathbf{x}_i})(\boldsymbol{p}_j\cdot\nabla_{\mathbf{x}_j})G_r(|\mathbf{x}_i - \mathbf{x}_j - \mathbf{R}|) \tag{C.17}$$

represents the short-range interaction and can be computed in real space. Further the parameter σ can be selected to be suffciently small such that W^r_{dip} becomes negligible and yet the computation of W^k_{dip} is kept tractable. The same procedure can be applied to the 3D case to give $G_r(\mathbf{x}) = -\frac{1}{4\pi x}\left[\text{erfc}(\frac{x}{\sqrt{2}\sigma})\right]$. Alternatively, equation (C.14) can be directly solved using spherical coordinates to obtain the expression of $G_r(\mathbf{x})$ for the 3D case.

Reciprocal-space self-interaction term ($W^{k\_self}_{dip}$)

Next, we determine the self-interaction term $W^{k\_self}_{dip}$ which is a fictitious term that has been included in W^k_{dip}. In the 2D case,

$$\begin{aligned} G_\sigma(\mathbf{x},\mathbf{x}') &= G(\mathbf{x},\mathbf{x}') - G_r(\mathbf{x},\mathbf{x}') \\ &= \frac{1}{2\pi}\ln(|\mathbf{x}-\mathbf{x}'|) - \frac{1}{4\pi}\text{Ei}\left(-\frac{x^2}{2\sigma^2}\right). \end{aligned}$$

This expression is difficult to be differentiated. Instead, using series expansion about $t = -\frac{|\mathbf{x}-\mathbf{x}'|^2}{2\sigma^2} = 0$, i.e. $\text{Ei}(t) = \gamma + \ln|t| + t + \frac{t^2}{2\cdot 2!} + \frac{t^3}{3\cdot 3!} + \ldots$, we obtain

$$G_\sigma(\mathbf{x},\mathbf{x}') = -\frac{\gamma}{4\pi} + \frac{1}{4\pi}\ln(2\sigma^2) + \frac{1}{8\pi\sigma^2}|\mathbf{x}-\mathbf{x}'|^2 + O(|\mathbf{x}-\mathbf{x}'|^4)$$

Then,

$$\begin{aligned} W^{k\_self}_{dip} &= -\frac{1}{2\epsilon_0}\lim_{\mathbf{x}_i\to\mathbf{x}_j}\sum_{i=1}^{N}(\boldsymbol{p}_i\cdot\nabla_{\mathbf{x}_i})(\boldsymbol{p}_i\cdot\nabla_{\mathbf{x}_j})G_\sigma(\mathbf{x}_i,\mathbf{x}_j) \\ &= \frac{1}{8\pi\sigma^2\epsilon_0}\sum_{i=1}^{N}|\boldsymbol{p}_i|^2. \end{aligned} \tag{C.18}$$

In the 3D case,

$$W^{k\_self}_{dip} = \frac{1}{12\sqrt{2}\pi^{3/2}\sigma^3\epsilon_0}\sum_{i=1}^{N}|\boldsymbol{p}_i|^2. \tag{C.19}$$

Surface term (W^{surf}_{dip})

Finally, we derive the surface term W^{surf}_{dip} following [148]. Consider a system comprising of two concentric circular (spherical for 3D) dielectrics with dielectric constants ϵ and ϵ', and radii of a and b respectively with $a < b$. The entire system is placed in a vacuum in the 2D or 3D space with an electric field $\mathbf{E}$ applied. In the limit of $a \to \infty$, $b \to \infty$, and $a/b \to 0$, the electric field in region I (the inner

region) is given by

$$\mathbf{E}_I = \begin{cases} \dfrac{4\epsilon'}{(\epsilon'+1)(\epsilon'+\epsilon)}\mathbf{E}, & d=2 \\ \dfrac{9\epsilon'}{(\epsilon'+2)(2\epsilon'+\epsilon)}\mathbf{E}, & d=3 \end{cases} \tag{C.20}$$

and the polarization $\mathbf{p}$ is

$$\mathbf{p} = \epsilon_0(\epsilon - 1)\mathbf{E}_I.$$

The electrostatic field $\mathbf{E}'_I$ that would be present in region I if it were empty is obtained by setting $\epsilon = 1$ in equation (C.20,) and hence

$$\mathbf{E}'_I = \begin{cases} \dfrac{4\epsilon'}{(\epsilon'+1)^2}\mathbf{E}, & d=2 \\ \dfrac{9\epsilon'}{(\epsilon'+2)(2\epsilon'+1)}\mathbf{E}, & d=3. \end{cases}$$

The total dipole moment $\mathbf{M}$ of the unit cell of area V gives rise to a surface charge at the boundary of the circle (sphere for 3D), which generates a homogeneous depolarizing field

$$\mathbf{E}_{depolarizing} = \mathbf{E}_I - \mathbf{E}'_I = \begin{cases} -\dfrac{1}{\epsilon_0(\epsilon'+1)}\mathbf{p}, & d=2 \\ -\dfrac{1}{\epsilon_0(2\epsilon'+1)}\mathbf{p}, & d=3 \end{cases}$$

where $\mathbf{p} = \mathbf{M}/V$. The reversible work per unit volume needed to be done against the depolarizing field to create the net polarization $\mathbf{p}$ is $dw = -\mathbf{E}_{depolarizing}d\mathbf{p}$, and the total work needed to polarize the system is hence

$$W_{dip}^{surf} = \begin{cases} \dfrac{2}{\epsilon_0(\epsilon'+1)}|\mathbf{p}|^2 V = \dfrac{1}{2V}\dfrac{1}{\epsilon_0(\epsilon'+1)}\left|\sum_{i=1}^{N}\boldsymbol{p}_i\right|^2, & d=2 \\ \dfrac{2}{\epsilon_0(2\epsilon'+1)}|\mathbf{p}|^2 V = \dfrac{1}{2V}\dfrac{1}{\epsilon_0(2\epsilon'+1)}\left|\sum_{i=1}^{N}\boldsymbol{p}_i\right|^2, & d=3. \end{cases} \tag{C.21}$$

In the context of the periodic lattice, this term is dependent on the dielectric constant at the boundary at infinity ϵ' and is therefore called the surface term. This term can also be interpreted as the contribution from the $k = 0$ component that has been omitted in W_{dip}^{k}. ϵ' is set to 1 in all simulations to represent vacuum boundary conditions so that the formation of ferroelectric domains can be observed. Using this value of ϵ' gives the same value of W_{dip} as obtained by following a spherical order of summation in the direct sum calculation in equation (C.10). If ϵ' is infinity which corresponds to a metallic boundary condition, then the surface term vanishes.

Combining all terms

Combining the results (C.15,C.16,C.17,C.18,C.19,C.21) gives equation (4.6) in Section 4.3. In the 3D case, these energy expressions are also consistent with literature [90, 91].

Appendix D

ALTERNATIVE APPROACH TO ANALYZING DOMAIN SIZE USING HAAR WAVELET DECOMPOSITION

In Section 4.4, we present a simple way to evaluate the average domain size of a domain pattern using breadth first search. Here we show similar results using wavelet decomposition.

We perform a 2D Haar wavelet trasformation on a dipole pattern represented by matrix $\mathbf{X}$ the same way as in Section 4.4, except that now we do so not only at the finest level ($j = 1$), but also at every level j to obtain the corresponding horizontal ($\mathbf{H}_j$), vertical ($\mathbf{V}_j$), and diagonal ($\mathbf{D}_j$) detail coefficients, where $j = 1, 2, ..., J$, $J = \log_2 L$, and L is the linear size of the periodic lattice. Note that the filters of the Haar wavelets used are normalized in the same way as [92].

We can partition data variance by scale. Given

$$\mathrm{var}(\mathbf{X}) = \sum_{j=1}^{J} \left[\mathrm{var}(\mathbf{H}_j) + \mathrm{var}(\mathbf{V}_j) + \mathrm{var}(\mathbf{D}_j)\right], \tag{D.1}$$

we can examine the sum of the variances corresponding to horizontal, vertical, and diagonal detail coefficients of the simulated dipole states at each level j which is the quantity in the square brackets of the above equation. This provides information on the proportion in which the wavelet variance at the scale $\tau_j = 2^{j-1}$ accounts for the variability in the data. Disregarding the finest scale which captures details of the domain walls as well as abnormalities, we can compute the expectation of level $\langle j \rangle$, and hence estimate the average scale of domains as $\langle \tau_j \rangle = 2^{\langle j \rangle - 1}$ for each domain pattern. As seen in Figure D.1, the expected values for different realizations span across a range for each PZT composition. However, there is clearly a dip in the length scale of domain structure at the MPB. This is consistent with Figure 4.3(f) which computes the average domain size via breadth first search and shows a smaller average domain size there.

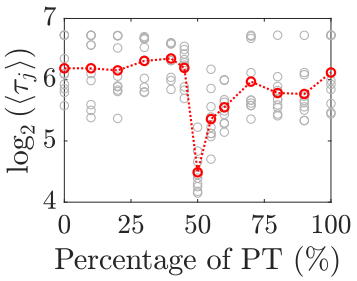

Figure D.1: Average scale of domains estimated using level-by-level variance decomposition. The grey circles show all ten realizations for each percentage of PT, while the red lines show the average values.

Appendix E

USEFUL EQUATIONS FOR MACHINE LEARNING MODELS

Here we provide more details regarding the machine learning models constructed in Chapter 5. Section E.1 presents the expressions of band structure energy density, volumetric entropy, and total free energy in a crystal that are used in data collection for both training and testing of the machine learning models. On the other hand, Section E.2 details the backpropagation method involving the neural networks for obtaining energy derivatives as needed in Chapter 5.4.

E.1 Band structure energy density, volumetric entropy, and total free energy in a crystal

In the context of a crystal that has electronic orbital $\psi_{i,\mathbf{k}}$ and energy state $E_{i,\mathbf{k}}$ associated with each $\mathbf{k}$ point in the Brillouin zone of the unit cell $\mathcal{U}$, the band structure energy density and volumetric generalized entropy are given by

$$u(\mathbf{x}) = \sum_{\mathbf{k}\in \mathrm{IBZ}} \sum_{i=1}^{N_{band}} w_{\mathbf{k}} E_{i,\mathbf{k}}\, f(E_{i,\mathbf{k}}) |\psi_{i,\mathbf{k}}(\mathbf{x})|^2, \tag{E.1}$$

$$s(\mathbf{x}) = -\frac{1}{\sqrt{\pi}} \sum_{\mathbf{k}\in \mathrm{IBZ}} \sum_{i=1}^{N_{band}} w_{\mathbf{k}} |\psi_{i,\mathbf{k}}(\mathbf{x})|^2 e^{-t^2} (\kappa t^3 + t^2 - \frac{1}{2}), \quad t = \beta(E_{i,\mathbf{k}} - E_f). \tag{E.2}$$

Here we restrict $\mathbf{k}$ to the irreducible Brillouin zone (IBZ) of $\mathcal{U}$ and add appropriate weights $w_{\mathbf{k}}$ satisfying $\sum_{\mathbf{k}\in \mathrm{IBZ}} w_{\mathbf{k}} = 1$. The energy eigenstates have also been normalized such that $\int |\psi_{i,\mathbf{k}}(\mathbf{x})|^2 d\mathbf{x} = 1$ for all $i, \mathbf{k}$.

Finally, we consider the total energy expression. The Kohn-Sham ground state energy is

$$\begin{aligned} E_{KS}[\{\psi_{i,\mathbf{k}}\}, \{R_I\}] = &\sum_{i=1}^{N_{band}} \sum_{\mathbf{k}\in \mathrm{IBZ}} -\frac{1}{2} w_{\mathbf{k}} f(E_{i,\mathbf{k}}) \int \psi^*_{i,\mathbf{k}}(\mathbf{x}) \nabla^2 \psi_{i,\mathbf{k}}(\mathbf{x}) d\mathbf{x} \\ &+ E_H[\rho(\mathbf{x})] + \int \rho(\mathbf{x}) V_{\mathrm{ext}}(\mathbf{x}) d\mathbf{x} + \int e_{xc}[\rho(\mathbf{x})] d\mathbf{x} \\ &+ E_{\mathrm{ion}}[\{R_I\}] + E_{core}, \end{aligned} \tag{E.3}$$

where the first term of the expression is the independent-particle kinetic energy, $\rho(\mathbf{x}) = \sum_{i=1}^{N_{band}} \sum_{\mathbf{k}\in \mathrm{IBZ}} w_{\mathbf{k}} f(E_{i,\mathbf{k}}) |\psi_{i,\mathbf{k}}|^2$ is the valence electronic density, E_{H} is the

Hartree energy (or in other words, the classical Coulomb interaction energy of the electron density interacting with itself), and E_{ion} is the Coulomb energy associated with interactions among the ions at positions $\{R_I\}$ which is computed using the Ewald summation method. There is also an additional energy contribution known as E_{core} arising from the fact that the ion is not a point charge. Its exact expression can be found in [149].

Using the Kohn-Sham equation $\mathcal{H}_{KS}\psi_{i,\mathbf{k}} = E_{i,\mathbf{k}}\psi_{i,\mathbf{k}}$ with $\mathcal{H}_{KS} = -\frac{1}{2}\nabla^2 + V_{\mathrm{H}} + V_{\mathrm{ext}} + V_{\mathrm{xc}}$ and orthonormality condition $\int \psi^*_{i,\mathbf{k}}(\mathbf{x})\psi_{i,\mathbf{k}}(\mathbf{x})d\mathbf{x} = \delta_{i,i'}\delta_{\mathbf{k},\mathbf{k}'}$, we may rewrite the ground state energy in terms of the band structure energy U analogous to equation (5.5) as follows:

$$E_{KS}[\{\psi_{i,\mathbf{k}}\},\{R_I\}] = \underbrace{\sum_{i=1}^{N_{band}} \sum_{\mathbf{k}\in \mathrm{IBZ}} w_{\mathbf{k}} f(E_{i,\mathbf{k}})E_{i,\mathbf{k}}}_{U} - E_H[\rho(\mathbf{x})] - \int V_{xc}[\rho(\mathbf{x})]\rho(\mathbf{x}) + \int e_{xc}[\rho(\mathbf{x})]d\mathbf{x} + E_{ion}[\{R_I\}] + E_{core}. \tag{E.4}$$

Then, the total Helmholtz free energy of the system is simply

$$\mathcal{F} = E_{KS} - S/\beta. \tag{E.5}$$

E.2 Backpropagation method in obtaining energy derivatives

The machine learning model that maps deformation $D = \{\lambda_a, \lambda_b, \lambda_c, \theta_a, \theta_b, \theta_c\}$ to the total free energy $\mathcal{F}$ has the following mathematical structure:

$$\mathbf{h}^{(0)} = \mathbf{W}^{(0)^{-1}}\left(\mathbf{h}^{(-1)} - \mathbf{b}^{(0)}\right), \quad \mathbf{h}^{(-1)} = [\lambda_a\ \lambda_b\ \lambda_c\ \theta_a\ \theta_b\ \theta_c]^T,\ W^{(0)}_{ij} = 0 \text{ if } i \neq j,$$

$$\mathbf{h}^{(k)} = g\left(\mathbf{W}^{(k)^T}\mathbf{h}^{k-1} + \mathbf{b}^{(k)}\right), \quad k = 1, 2, 3,$$

$$h^{(4)} = \mathbf{W}^{(4)^T}\mathbf{h}^{(3)} + b^{(4)},$$

$$\mathcal{F} = h^{(5)} = W^{(5)}h^{(4)} + b^{(5)}.$$

The first and the fourth lines represent the preprocessing steps that remove the mean and variance from the data, where $\mathbf{b}^{(0)}, \mathbf{W}^{(0)}, \mathbf{b}^{(5)}, \mathbf{W}^{(5)}$ are the mean and standard deviation of the input D and output $\mathcal{F}$ of the model. The second and third lines indicate the dense neural network with three hidden layers, hyperbolic tangent activation function $g(x) = \tanh(x)$, and fitted weights $\mathbf{b}^{(k)}, \mathbf{W}^{(k)}$ with $k = 1, 2, 3$.

The derivatives of $\mathcal{F}$ with respect to $\mathbf{h}^{(-1)}$ can be computed as follows:

$$\frac{\partial \mathcal{F}}{\partial h_i^{(3)}} = W^{(5)} W_{i1}^{(4)},$$

$$\frac{\partial \mathcal{F}}{\partial h_i^{(k-1)}} = \sum_j \frac{\partial \mathcal{F}}{\partial h_j^{(k)}} g'((\mathbf{W}^{(k)^T} \mathbf{h}^{(k-1)} + \mathbf{b}^{(k)})_j) W_{ij}^{(k)}, \quad k = 3, 2, 1,$$

$$\frac{\partial \mathcal{F}}{\partial h_i^{(-1)}} = \frac{\partial \mathcal{F}}{\partial h_i^{(0)}} \frac{1}{W_{ii}^{(0)}}.$$

Subsequently, applying the chain rule gives

$$\frac{\partial \mathcal{F}}{\partial \varepsilon_{kl}} = \sum_{i=1}^{6} \frac{\partial \mathcal{F}}{\partial h_i^{(-1)}} \frac{\partial h_i^{(-1)}}{\partial \varepsilon_{kl}}.$$

Appendix F

UNIAXIAL STRESS AND TRANVERSE STRAIN FROM DIFFERENT MACHINE LEARNING APPROACHES

Figure F.1 compares the ground truth uniaxial stress and transverse strain to those of the two ML approach, where the free energy is computed using the direct and sum approaches, respectively. In the case of the sum approach, there is not an analytical expression of $\frac{\partial \mathcal{F}}{\partial \varepsilon_{ij}}$, the derivative is therefore computed numerically. It is observed that the sum approach is able to better track the response of lattice instability under high compression in the x_2 direction, therefore demonstrating the robustness of computing the energy with the learned fields.

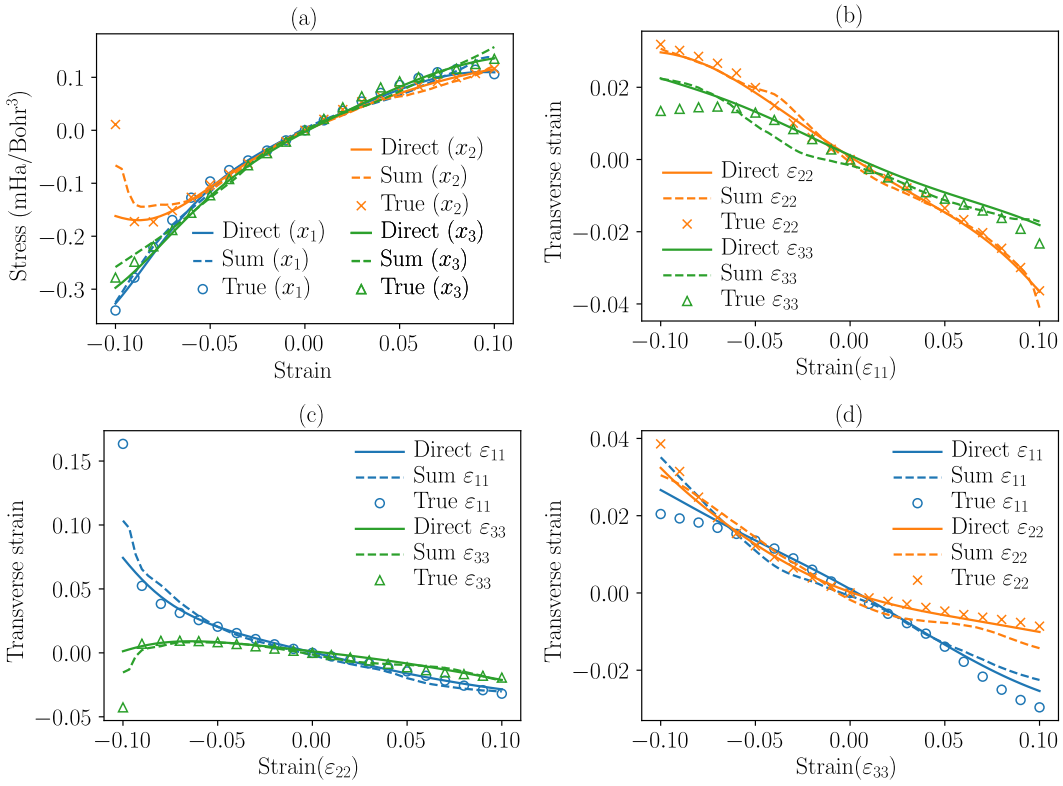

Figure F.1: Uniaxial test results. The results obtained from our machine learning models are marked as 'direct' and 'sum', while the results obtained directly from DFT calculations with stress relaxation are marked as 'true.' Note that the 'direct' and 'true' results are the 'ML' and 'true' results reproduced from Figure 5.9. (a) Stress-strain curves for uniaxial stress in the x_1, x_2, and x_3 directions. (b–d) Corresponding transverse strain.